Measurement of the Λ_b Polarization with pp Collisions at 7 TeV

Dissertation

zur

Erlangung der naturwissenschaftlichen Doktorwürde (Dr. sc. nat.)

vorgelegt der

Mathematisch-naturwissenschaftlichen Fakultät

der

Universität Zürich

von

Mirena Ivova Rikova

aus

Bulgarien

Promotionskomitee

Prof. Dr. C. Amsler (Vorsitz)
Prof. Dr. V. Chiochia

Zürich, 2013

To my family

Abstract

This thesis presents a measurement of the Λ_b baryon polarization with proton-proton collisions at a center-of-mass energy $\sqrt{s} = 7$ TeV. The analysis is performed with the CMS detector at the Large Hadron Collider at CERN. The results are based on data collected in 2011 corresponding to an integrated luminosity $\mathcal{L} = 5.1$ fb^{-1}.

Λ_b candidates are reconstructed in the decay mode $\Lambda_b \to J/\psi(\mu^+\mu^-)\Lambda(p\pi^-)$. The selected signal yield is 911 ± 38 and 845 ± 37 candidates for Λ_b and $\overline{\Lambda}_b$, respectively. The polarization is extracted through the angular correlations between the daughter particles in the decay by a multi-dimensional likelihood fit. A production polarization of

$$P^+ = 0.03 \pm 0.09 \text{ (stat.)} \pm 0.03 \text{ (syst.)} \quad \text{for } \Lambda_b$$

and

$$P^- = 0.02 \pm 0.08 \text{ (stat.)} \pm 0.05 \text{ (syst.)} \quad \text{for } \overline{\Lambda}_b$$

is measured. The parity violating asymmetry parameter characterizing the decay $\Lambda_b \to J/\psi\,\Lambda$ is measured to be 0.47 ± 0.24 (stat.) $\pm$ 0.17 (syst.).

A key detector system for the presented polarization analysis is the silicon pixel detector of CMS. It allows precise reconstruction of primary and displaced vertices as well as particle momentum measurements. Due to the presence of combined electric and magnetic fields, the charge carriers in the silicon pixel sensors experience the Lorentz force and their drift direction is deviated at the so-called *Lorentz angle*. This leads to a shift in the measured hit position which needs to be corrected for. Measurements of the Lorentz angle for the barrel pixel detector are presented, performed with cosmic ray data and collision data and utilizing two independent measurement techniques. For a nominal magnetic field of 3.8 T and a bias voltage of 150 V, the measured Lorentz angle is 21.7° with a systematic uncertainty of less than 5%.

Zusammenfassung

Diese Doktorarbeit berichtet über die Messung der Polarisation des Λ_b-Baryons in Proton-Proton-Kollisionen mit dem CMS-Detektor am Large Hadron Collider des CERN bei einer Schwerpunktsenergie von $\sqrt{s} = 7$ TeV. Es wurde der Datensatz aus dem Jahr 2011 benutzt, welcher einer integrierten Luminosität von $\mathcal{L} = 5.1\ \text{fb}^{-1}$ entspricht.

Λ_b-Kandidaten werden im Zerfallskanal $\Lambda_b \rightarrow J/\psi(\mu^+\mu^-)\Lambda(p\pi^-)$ rekonstruiert. Auf diese Weise konnten 911 ± 38 Λ_b und 845 ± 37 $\overline{\Lambda}_b$ gefunden werden. Die Polarisation wird mit Hilfe eines mehrdimensionalen Likelihood-Fits aus den Winkelverteilungen der Tochterteilchen bestimmt. Die Messung ergab eine Polarisation von

$$P^+ = 0.03 \pm 0.09\,(\text{stat.}) \pm 0.02\,(\text{syst.}) \text{ für } \Lambda_b$$

und

$$P^- = 0.02 \pm 0.08\,(\text{stat.}) \pm 0.06\,(\text{syst.}) \text{ für } \overline{\Lambda}_b.$$

Der Parameter der paritätsverletzenden Asymmetrie in diesem Zerfallskanal wurde zu $0.47 \pm 0.24\,(\text{stat.}) \pm 0.017\,(\text{syst.})$ gemessen.

Der Siliziumpixeldetektor im CMS-Detektor spielte eine entscheidende Rolle für diese Messung. Er ist in der Lage, den geometrischen Ort von Zerfallsvertices sowohl am Ursprung als auch versetzt davon zu messen und die Impulse der Spuren zu bestimmen. Das den Detektor umgebende Magnetfeld erzeugt auf die Ladungsträger im Silizium eine Lorentzkraft, welche zu einem durch den *Lorentzwinkel* beschriebenen Versatz in der Ortsmessung führt. Die Kenntnis dieses Winkels ist entscheidend um die Messung zu eichen. Für den zylindrischen Teil des Pixeldetektors wurde dieser Winkel mit Daten sowohl von Kollisionen als auch von kosmischen Müonen unter Zuhilfenahme zweier unterschiedlicher Verfahren bestimmt. Für ein nominelles Magnetfeld von 3.8 T und einer Sperrspannung von 150 V beträgt der Lorentzwinkel 21.7°, mit einer systematischen Unsicherheit von weniger als 5%.

Contents

Chapter 1

Theoretical introduction and motivation

1.1 A brief historical overview

1.1.1 Discovery of the b-quark

The existence of three generations of quarks was first postulated in 1973 by Makoto Kobayashi and Toshihide Maskawa as a part of their model to explain the recently observed CP violation in neutral kaon decays [1]. At that time not even the second quark family was fully confirmed and only three quarks were known – up (u), down (d) and strange (s). Kobayashi and Maskawa suggested in their work that a third generation of quarks allows for CP-violation effects to be introduced within the Standard Model. Their speculation on six quarks, however, did not gain popularity and their paper published in the Japanese journal *Progress on Theoretical Physics* remained rather unknown in Europe and in the U.S. The following year (1974) the unexpected discovery of the J/ψ meson, simultaneously by two competing experiments [2, 3], confirmed the existence of a fourth quark, namely the charm (c).

In 1977 the experiment E288 at Fermilab headed by Leon Lederman observed a resonance in the dimuon invariant mass spectrum at 9.5 GeV/c^2 (see Figure 1.1a) [4]. It was identified as a meson formed out of a new quark and its antiquark. The meson was named Υ and was the first observed particle with a constituent *beauty* (or also *bottom*) quark. With the discovery of the top (t) quark in 1995 by the experiments D0 and CDF [5, 6] the third quark family was complete. This won Kobayashi and Maskawa the Nobel Prize in Physics in 2008 *"for the discovery of the origin of the broken symmetry which predicts the existence of at least three families of quarks in nature"*.

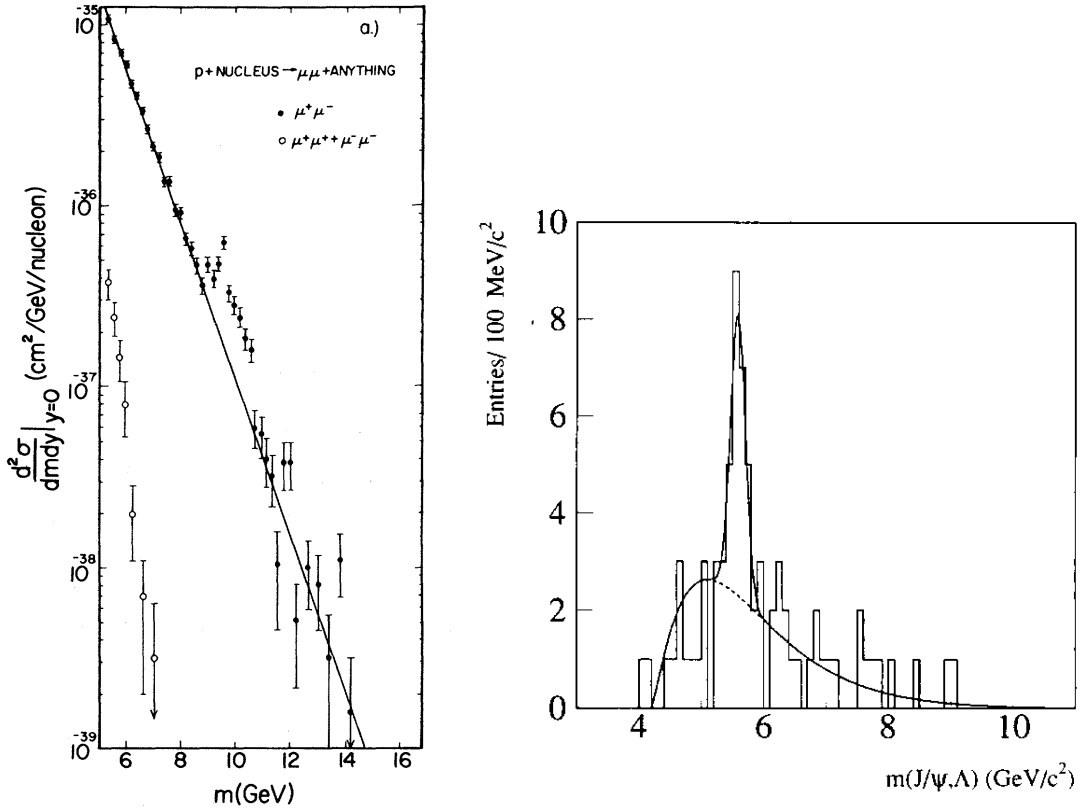

(a) **(b)**

Figure 1.1: (a) First evidence of a b-flavored meson, the Υ particle, by the E288 experiment at Fermilab in 1977 [4]. The decay channel is $\Upsilon \to \mu^+\mu^-$. (b) First observation of the Λ_b baryon in 1991 by the UA1 Collaboration at CERN [7]. The decay mode is $\Lambda_b \to J/\psi\,\Lambda$.

1.1.2 Discovery of the Λ_b baryon

In the following years, starting from 1981, inclusive decays of b-flavored hadrons were observed by the CLEO and CUSB detectors [8, 9, 10, 11, 12]. First observation of exclusive decay modes of b-flavored mesons was achieved by the CLEO detector in 1983 [13]. Naturally, the next goal was the observation of b-flavored baryons.

The lightest baryon with a constituent b-quark is the neutral Λ_b with quark composition (udb). Evidence of its first observation was reported in the channel $\Lambda_b \to p\pi^- D^0(\to K^-\pi^+)$ with six-standard-deviation significance in 1981 at the CERN ISR [14]. However, a second experiment performed few months later and using the same detector did not observe any signal [15]. The question about a conclusive observation of a b-flavored baryon remained open until 1991 when the UA1 experiment at the $p\bar{p}$ collider at CERN announced the discovery of Λ_b in the

decay channel $\Lambda_b \to J/\psi\,\Lambda$ [7]. Although a modest number, the reconstructed 16 ± 5 signal events above a background of 9 ± 1 events (see Figure 1.1b) were the first decisive observation of a beauty baryon in an exclusive decay channel.

Measurements of the Λ_b baryon mass result in a current world average value of 5619.4 ± 0.7 MeV/c^2 [16]. Significant attention has been drawn to Λ_b due to discrepancies between the theoretically predicted and the experimentally measured particle lifetime and mismatch between different experimental results [17]. However, the most recent and improved calculations and measurements show good agreement [18]. The world average measured Λ_b lifetime up to date is $\tau(\Lambda_b) = 1.425 \pm 0.032$ ps which is equivalent to a mean decay length of $c\tau(\Lambda_b) \approx 427$ μm.

1.2 Production and decays of b-hadrons at the LHC

1.2.1 Production of $b\bar{b}$ pairs

The leading-order (LO) mechanism in QCD for production of b-quarks in proton-proton collisions is pair creation. The process can be either light quark–antiquark annihilation $q\bar{q} \to b\bar{b}$ or gluon-gluon fusion $gg \to b\bar{b}$. As shown in Figure 1.2, at leading-order the only product of the process is the $b\bar{b}$ pair. The quarks are therefore produced with equal but opposite momenta, which results in two back-to-back jets in the detector.

In next-to-leading order (NLO) production mechanisms, there is one more quark-gluon or gluon-gluon vertex, as shown in Figure 1.3. One such process is the flavor excitation in which a parton from one beam particle scatters against a sea $b(\bar{b})$ quark from the other beam. Another NLO process is the gluon splitting, $g \to b\bar{b}$, in which the $b\bar{b}$ pair occurs from a virtual gluon. The quarks produced via NLO mechanisms are not necessarily back-to-back as the third final-state parton carries away a fraction of the total momentum.

The predicted contributions of the different production mechanisms and the total $b\bar{b}$ cross section in proton-proton collisions is shown in Figure 1.4 as a function of the center-of-mass energy [19]. At the LHC energy of 7 TeV, the dominant contribution comes from the next-to-leading order flavor excitation process.

1.2.2 Hadronization

Due to the color confinement, the quark (antiquark) from the produced $q\bar{q}$ pair can not exist individually as a single, colored-charged object. They both hadronize to

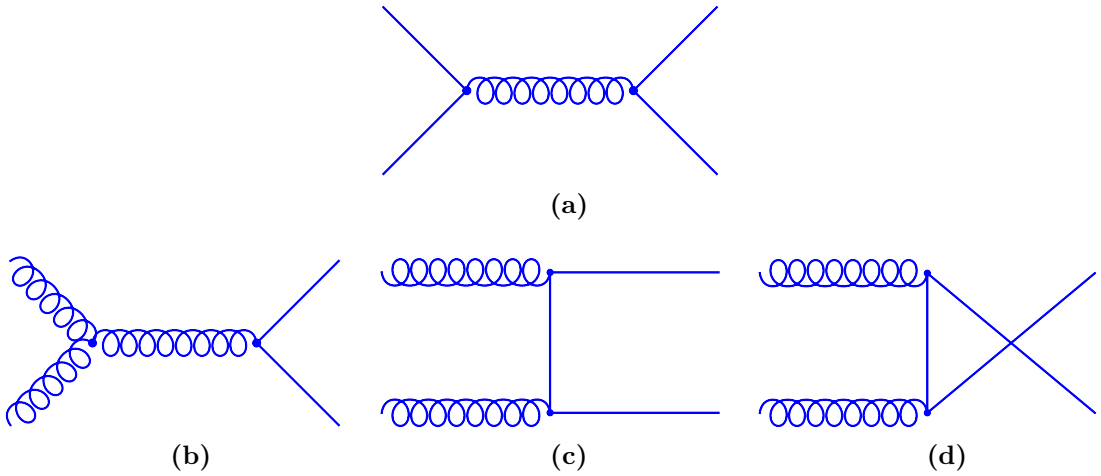

Figure 1.2: Leading order processes for $b\bar{b}$ pair production: (a) quark–antiquark annihilation $q\bar{q} \rightarrow b\bar{b}$, (b),(c),(d) gluon-gluon fusion $gg \rightarrow b\bar{b}$.

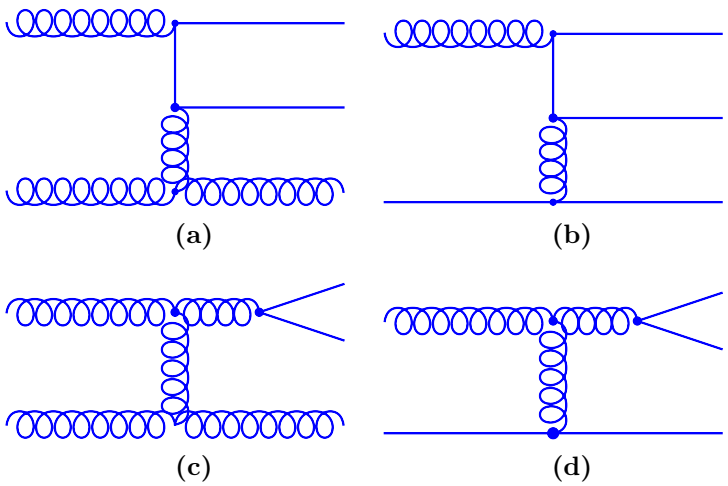

Figure 1.3: Next-to-leading order processes for $b\bar{b}$ pair production: (a),(b) flavor excitation, (c),(d) gluon splitting.

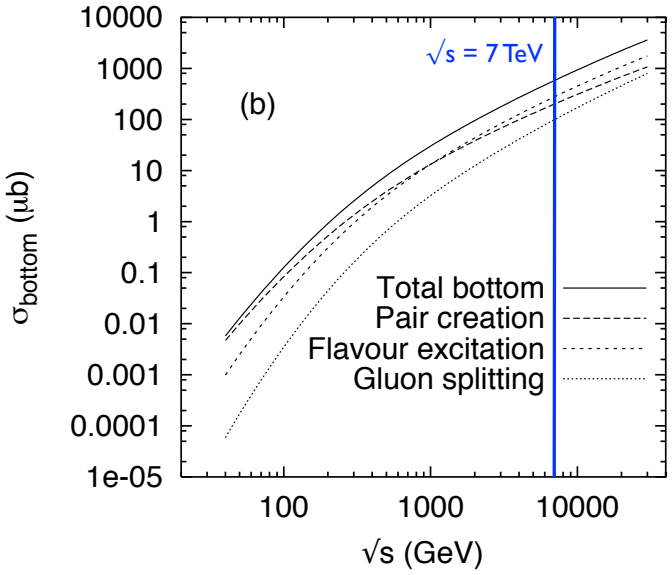

Figure 1.4: Total $b\bar{b}$ cross section in proton-proton collisions as a function of the center-of-mass energy $\sqrt{s}$. The contributions from pair creation, flavor excitation and gluon splitting are shown [19].

form colorless b-flavored hadrons. A summary of the existing hadronization models for the conversion of quarks and gluons into hadrons can be found in [20].

1.2.3 Decays of b-hadrons

With a mass of $m_b = 4.18 \pm 0.03$ GeV/c^2 [16], the b-quark is significantly heavier than the other quarks (u, d, s and even c) which can constitute a hadron and therefore the b-quark carries most of the hadron momentum. It is then fair to assume that in a first approximation the decay of the b-hadron is described by the b-quark decay and is independent of the light constituent quarks which act as spectators. This assumption is the basis of the so called *spectator model* and the Heavy Quark Effective Theory (HQET) [21, 22].

The b-quark can decay by the weak interaction to the lighter c- or u-quark through the emission of a W boson. The strengths of the transitions from one flavor to another through a charged W boson are contained in the Cabibbo-Kobayashi-Maskawa (CKM) quark-mixing matrix V_{CKM} [1]:

$$V_{CKM} = \begin{pmatrix} V_{ud} & V_{us} & V_{ub} \\ V_{cd} & V_{cs} & V_{cb} \\ V_{td} & V_{ts} & V_{tb} \end{pmatrix} \tag{1.1}$$

The matrix elements related to the b-quark decay are $|V_{cb}|$ and $|V_{ub}|$ involved in the processes $b \to cW^-$ and $b \to uW^-$, respectively. They have been measured to be $|V_{cb}| = 0.0409 \pm 0.0011$ and $|V_{ub}| = 0.00415 \pm 0.00049$, which is significantly smaller compared to other elements in the V_{CKM} matrix [16]. This indicates that the decay of the b-quark is highly suppressed compared to the decays of the other quarks and leads to a relatively large b-quark mean lifetime $\tau \sim 10^{-12}$ s. The matrix element $|V_{cb}|$ is a factor 10 larger than $|V_{ub}|$, from which it follows that the b-quark decays almost exclusively to a c- and not to a u-quark. The measured mean lifetime in the laboratory frame, τ_{lab}, is dilated by the Lorentz factor γ,

$$\tau_{lab} = \gamma\tau, \tag{1.2}$$

where

$$\gamma = \frac{1}{\sqrt{1-\beta^2}} \quad \text{and} \quad \beta = \frac{v}{c}, \tag{1.3}$$

with v being the velocity of the particle and c is the speed of light. Therefore, the observed mean decay length L_{lab} in the laboratory frame for a particle moving at a velocity v is

$$L_{lab} = \tau_{lab} v = \gamma\tau\beta c = \frac{p}{m} c\tau, \tag{1.4}$$

where p and m are the momentum and mass of the particle, respectively. For b-hadrons produced at the LHC, the flight distance is typically of the order of several millimeters and can be registered in the detector as a secondary vertex, displaced from the primary interaction point.

1.2.4 The decay $\Lambda_b \to J/\psi\,\Lambda$

The relatively long lifetime of the Λ_b baryon indicates that it decays by the weak interaction. The decay $\Lambda_b \to J/\psi\,\Lambda$ proceeds with the emission of a W^- boson, as illustrated in Figure 1.5. As can be seen from the diagram, this is a color-suppressed process because the quarks from the W^- decay are constrained to match the colors of the c-quark and the spectator diquark system in order to form the J/ψ and Λ hadrons, respectively. The integrated Λ_b cross section times branching fraction $\sigma(\Lambda_b) \times \mathcal{B}(\Lambda_b \to J/\psi\,\Lambda)$ has been reported in Ref. [23] for pp collisions at $\sqrt{s} = 7$ TeV and a transverse momentum of Λ_b greater than 10 GeV/c. The reported result is $1.16 \pm 0.06 \pm 0.12$ nb where the uncertainties are statistical and systematic, respectively.

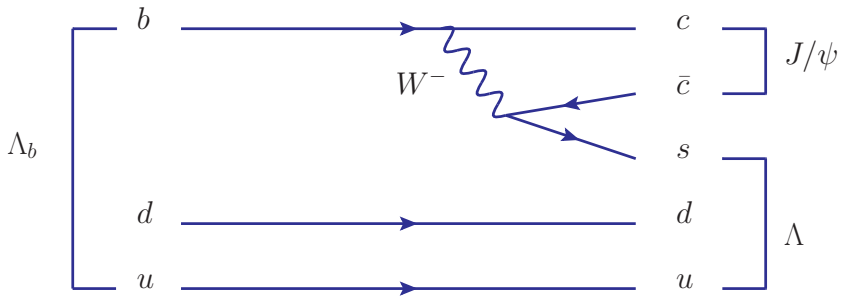

Figure 1.5: Feynman diagram for the decay $\Lambda_b \to J/\psi\,\Lambda$

1.3 Concept of polarization

1.3.1 Spin and helicity

The total angular momentum $\vec{J}$ combines the spin $\vec{S}$ and the orbital angular momentum $\vec{L}$,

$$\vec{J} = \vec{L} + \vec{S}. \tag{1.5}$$

From Noether's theorem [24], it follows that the total angular momentum of a system is a conserved quantity.

The helicity λ of a particle is defined as the projection of the total angular momentum $\vec{J}$ on the direction of the particle's momentum $\vec{p}/|\vec{p}|$:

$$\lambda = (\vec{L} + \vec{S}) \cdot \frac{\vec{p}}{|\vec{p}|} = \vec{L} \cdot \frac{\vec{p}}{|\vec{p}|} + \vec{S} \cdot \frac{\vec{p}}{|\vec{p}|} = \vec{S} \cdot \frac{\vec{p}}{|\vec{p}|} = m_s, \tag{1.6}$$

where it is taken into account that the orbital angular momentum $\vec{L}$ is perpendicular to the linear momentum $\vec{p}$. The discrete $2s+1$ eingenvalues of the helicity are $\{-s, -(s-1), ..., s-1, s\}$, where s is the spin quantum number.

1.3.2 Spin density matrix

Consider a particle (a quantum system) in its rest frame with spin J. It is represented by a mixture of quantum states $|\psi\rangle$, accounting for all possible projections M of the spin which take on values $M \in \{-J, -(J-1), ..., J-1, J\}$:

$$|\psi\rangle = \sum_{M=-J}^{+J} a_M |JM\rangle, \tag{1.7}$$

where a_M are complex coefficients. The spin density matrix ρ of the system is defined as

$$\rho = \rho_{MM'} = a_M a^*_{M'}. \tag{1.8}$$

It is of dimension $(2J+1) \times (2J+1)$ and has the following properties:

- ρ is Hermitian: $\rho^+ = \rho$ i.e. $\rho^*_{M'M} = \rho_{MM'}$
- $\mathrm{Tr}(\rho) = 1$

The expectation value for an arbitrary physical observable with a corresponding Hermitian operator A is given by

$$\langle A \rangle = \mathrm{Tr}(\rho A). \tag{1.9}$$

1.3.3 Polarization

The polarization characterizes the alignment of the particle spin with a given direction. Consider the set of matrices $\vec{S}$ representing the spin operator. By definition, the polarization vector is given by the expectation value of the spin matrices,

$$\vec{P} = \langle \vec{S} \rangle = \frac{\mathrm{Tr}(\rho \vec{S})}{\mathrm{Tr}(\rho)}, \tag{1.10}$$

where the denominator serves for normalization. The best known case is for particles with spin 1/2 where $\vec{S}$ corresponds to the Pauli matrices, $\vec{\sigma} = (\sigma_x, \sigma_y, \sigma_z)$. For the general case of an arbitrary spin s, the set of matrices $\vec{S}$ is represented by three $(2s+1)$-dimensional Hermitian matrices being the generalization of the Pauli matrices [25].

1.4 Expectations on the polarization and asymmetry parameter of Λ_b

1.4.1 Heavy quark polarization

In QCD with massless quarks the helicity is conserved and no single-quark polarization can occur. Once the mass parameter is nonzero, the helicity conservation can be violated allowing for helicity flip and thus single-quark polarization in scattering processes. Interference between non-flip and spin-flip helicity amplitudes requires imaginary parts of the amplitudes which are only generated in loop corrections. The polarization expected from the QCD processes $q + q' \to q + q'$, $q + g \to q + g$, $g + g \to q + \bar{q}$ and $q + \bar{q} \to q' + \bar{q}'$ is calculated and summarized in Ref. [26]. The largest contributions for the b-quark polarization come from quark annihilation (at most $\sim$10%) and gluon fusion ($\sim$5/%). From the calculations in Ref. [26] it also follows that the polarization should depend on the quark mass – at a given momentum the heaviest quark acquires the largest polarization. The maximum occurs at

$m_Q/p_Q \simeq 0.3$, where m_Q and p_Q are the quark mass and momentum, respectively, and the polarization of the b-quark is predicted to be an order of magnitude larger than the s-quark. It is not possible to directly observe the polarization of a quark, but it can be deduced from the polarization or the density matrix elements of the resultant hadrons. The polarization of the Λ_b baryon is inherited as a fraction of the b-quark polarization.

However, the polarization of the Λ hyperon resulting from the polarized s-quark has been experimentally observed to be an order of magnitude larger compared to the QCD expectation [27] and this result remains unexplained to date. It can be therefore expected that the polarization of Λ_b might as well significantly exceed the predictions of QCD. On the other hand, the polarization of Λ has been observed to depend strongly on the fraction of the beam energy carried by the hyperon [28, 29, 30], which is characterized by the Feynman variable $x_F = 2p_L/\sqrt{s}$ where p_L is the longitudinal momentum of Λ and $\sqrt{s}$ is the center-of-mass energy in the collision. The Λ polarization is observed to vanish at $x_F \approx 0$. Considering that for Λ_b produced at LHC with $\sqrt{s} = 7$ TeV the Feynman variable is $x_F \approx 0.01$, a Λ_b polarization close to zero can be expected.

Clearly, the expectations on the Λ_b polarization are very contradictory. An actual Λ_b polarization measurement is of great theoretical interest since it can throw light on the quark mass dependence of the spin effects and unravel the puzzle of the observed anomalously large hyperon polarization.

1.4.2 Previous Λ_b polarization measurements

Polarization measurements of Λ_b baryons produced in $e^+e^- \to Z^0 \to b\bar{b}$ events have been performed at LEP [31, 32, 33]. The Standard Model predicts that the b-quarks from the Z^0 boson decay have large longitudinal polarization which is expected to be retained by the resultant baryon [34, 35]. Sizable Λ_b polarization has been measured by three experiments, although with large uncertainties:

$$\begin{aligned} P &= -0.23^{+0.24}_{-0.20}\ (\text{stat.}) \pm 0.08\ (\text{syst.}) \quad (\text{ALEPH}) \\ P &= -0.56^{+0.20}_{-0.13}\ (\text{stat.}) \pm 0.09\ (\text{syst.}) \quad (\text{OPAL}) \\ P &= -0.49^{+0.32}_{-0.30}\ (\text{stat.}) \pm 0.17\ (\text{syst.}) \quad (\text{DELPHI}) \end{aligned} \tag{1.11}$$

The reported polarizations are measured from semileptonic Λ_b decays and spread in the range $(-0.79, +0.01)$. Note that these results can not serve as expectations for the polarization of Λ_b produced at hadron colliders due to the different production mechanisms.

1.4.3 Parity violating parameter

The parity violating asymmetry parameter for the decay $\Lambda_b \to J/\psi\,\Lambda$ is of particular interest since it can serve as a test for various quark models such as perturbative QCD and factorization models. Calculations of the asymmetry parameter are reported in numerous publications, e.g. Ref. [36, 37, 38][1]. The expectations vary within a wide range, generally between 0.14 and -0.78 while the full physical range is $[-1, +1]$. A measurement of this parameter is of high interest in order to point and tune the quark models with realistic predictions.

1.4.4 Dilution of the polarization

Λ_b baryons can also be produced as decay products of heavier states, e.g. in the strong decays $\Sigma_b^{(*)\pm} \to \Lambda_b \pi^\pm$. This causes the Λ_b polarization to be diluted to a certain degree. The polarization conveyed to Λ_b depends on the ratio Δ/Γ of the mass difference Δ between Σ_b and Σ_b^* and the decay rate Γ of $\Sigma_b^{(*)} \to \Lambda_b \pi$ [39]. Using the result of the CDF Collaboration on the mass difference [40],

$$\Delta \equiv m_{\Sigma_b^*} - m_{\Sigma_b} = 21.2 \pm 2.0 \text{ MeV}/c^2, \tag{1.12}$$

and employing assumptions on the decay rate as shown in Ref. [41], it has been calculated that up to 30% depolarization can be expected due to Λ_b baryons originating from $\Sigma_b^{(*)}$ states.

1.5 Helicity formalism

1.5.1 General approach

The *helicity formalism* provides a general method to obtain the angular distributions in a chain of decaying particles. It is described in detail in Ref. [42, 43], and examples of its application can be found in Ref. [44]. The method derives from conservation of the total angular momentum and $P(C)$-conservation in strong and electromagnetic decays. A short overview of the helicity formalism follows.

Let us consider the decay $A \to B + C$ in the rest frame of particle A with quantization axis z. The particles A, B, and C have well defined spins $\vec{J}$, $\vec{s}_1$ and $\vec{s}_2$, respectively, and λ_1 and λ_2 are the helicities of B and C, respectively. Consider that the flight direction of particle B in the rest frame of A is described by the spherical coordinates (θ, φ). The final state is then characterized by the direction of the decay axis given by (θ, φ) and by the helicity states of the decay products. The

[1] The convention used for the definition of the asymmetry parameter in the quoted references requires a sign flip in order to match the definition of the parameter used in this thesis.

angular distribution depends on the initial spin density matrix ρ_i of particle A and the helicity amplitudes $T_{\lambda_1\lambda_2}$ for the decay $A \to B + C$. The helicity states refer to a frame which is obtained from the initial coordinate system by a sequence of rotations. In spin space, the rotations are described through the Wigner $\mathcal{D}$-matrix with elements

$$\mathcal{D}^J_{MM'}(\theta,\varphi) = e^{iM'\varphi}\, d^J_{MM'}(\theta). \tag{1.13}$$

The dynamics of the decay process is contained in the helicity matrix T whose elements are the helicity amplitudes defined as

$$T_{\lambda_1\lambda_2} = \sum_{L,S} \alpha_{LS} \langle J\lambda | LS0\lambda\rangle \langle S\lambda | s_1 s_2 \lambda_1, -\lambda_2\rangle. \tag{1.14}$$

In the above expression, α_{LS} are unknown complex coefficients, $\lambda = \lambda_1 - \lambda_2$ and the brackets are Clebsch-Gordon coefficients which describe the couplings $\vec{J} = \vec{L} + \vec{S}$ and $\vec{S} = \vec{s}_1 + \vec{s}_2$. The sum over L and S is constrained by the value of J and $P(C)$-conservation, and takes on the values in the range $|L - S| \leq J \leq L + S$.

The transition amplitude f for the decay is a matrix of dimension $(2s_1+1)(2s_2+1) \times (2J+1)$ with elements given by

$$f_{\lambda_1\lambda_2;M}(\theta,\varphi) = \mathcal{D}^J_{\lambda M}(\theta,\varphi)\; T_{\lambda_1\lambda_2} \tag{1.15}$$

The angular distribution $w(\theta,\varphi)$ of particle B in the rest frame of A is then determined by the following relation

$$w(\theta,\varphi) = \mathrm{Tr}(\rho_f) = \mathrm{Tr}(f\rho_i f^+), \tag{1.16}$$

where ρ_f and ρ_i are the final and initial spin density matrices of dimensions $(2s_1 + 1)(2s_2 + 1) \times (2s_1 + 1)(2s_2 + 1)$ and $(2J + 1) \times (2J + 1)$, respectively, and f is the transition amplitude.

1.5.2 Cascade decay chain

Let us consider now that the decay $A \to B + C$ with transition amplitude $f(A)$ is followed by the subsequent decays $B \to b_1 + b_2$ and $C \to c_1 + c_2$, with corresponding transition amplitudes $f(B)$ and $f(C)$, respectively, calculated by analogy with Eq. 1.15. Note that the angles (θ,φ) for each transition amplitude are defined in the rest frame of the respective decay. The transition amplitude for the total process is given by

$$f_T = [f(B) \otimes f(C)]f(A) \tag{1.17}$$

where the symbol $\otimes$ refers to a Kronecker (tensor) product. For further subsequent decays, e.g. $c_1 \to d_1 + d_2$ etc., the total transition matrix is obtained analogously. The angular distribution of the final-state particles is determined from the trace of the final density matrix (see Eq. 1.16).

1.6 Angular distributions for the decay $\Lambda_b \to J/\psi(\mu^+\mu^-)\Lambda(p\pi^-)$

1.6.1 Angular distributions of the final state particles

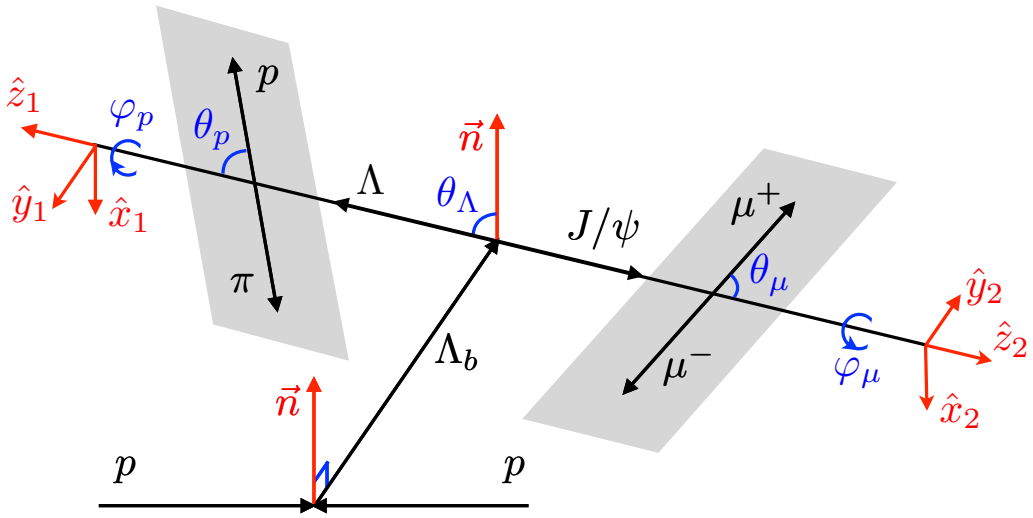

Figure 1.6: Definitions of the reference frames and angles used for the Λ_b polarization analysis in the decay $\Lambda_b \to J/\psi(\mu^+\mu^-)\Lambda(p\pi^-)$

Let us consider the inclusive production process $pp \to \Lambda_b + X$ with the consecutive decay $\Lambda_b \to J/\psi\,\Lambda$ in the rest frame of Λ_b, as is schematically illustrated in Figure 1.6. In proton-proton collisions, Λ_b is produced with a polarization vector perpendicular to the production plane due to parity conservation in the strong production mechanism. Let us define a vector $\vec{n}$ perpendicular to the production plane of Λ_b,

$$\vec{n} = \frac{\vec{p}_{beam} \times \vec{p}_{\Lambda_b}}{|\vec{p}_{beam} \times \vec{p}_{\Lambda_b}|}, \tag{1.18}$$

where $\vec{p}_{beam}$ and $\vec{p}_{\Lambda_b}$ are the vector-momenta of one incident proton beam and the Λ_b, respectively. The mean value of the Λ_b spin along $\vec{n}$ is the production polarization of Λ_b. Thus defined, it is by convention denoted as *transverse* polarization, to be distinguished from the *longitudinal* polarization, where the word is by tradition referred to the alignment of the field vector in photon polarization studies. Let us define the rest frame of the Λ_b particle $(\hat{x}, \hat{y}, \hat{z})$ in the following way:

$$\begin{aligned} \hat{z} &= \vec{n} \\ \hat{x} &= \vec{p}_{beam}/|\vec{p}_{beam}| \\ \hat{y} &= \hat{z} \times \hat{x} \end{aligned} \tag{1.19}$$

The quantization axis z is chosen parallel to $\vec{n}$. The choice of the orthogonal axes x and y is not important since parity conservation in the production process of Λ_b assures independence of the azimuthal angle. The angle θ is the polar angle of the Λ momentum in the rest frame of Λ_b with respect to the quantization axis $\hat{z} \equiv \vec{n}$. The particles participating in the decay have well defined spins of $J = 1/2$, $s_1 = 1/2$ and $s_2 = 1$ for Λ_b, Λ and J/ψ, respectively. $T_{\lambda_1\lambda_2}$ denotes the helicity amplitudes for the decay where $\lambda_1 = +, -$ and $\lambda_2 = +, 0, -$ indicate helicities of $\pm 1/2$ and $+1, 0, -1$ for Λ and J/ψ, respectively. The projection M of the Λ_b spin along the z-axis can be $\pm 1/2$, which constrains the values of λ_1 and λ_2 – among six combinations there are only four physically allowed helicity configurations. The decay is therefore described by four helicity amplitudes, T_{++}, T_{+0}, T_{-0} and T_{--}.

Let us further consider the decays of the intermediate resonances $\Lambda \to p\pi^-$ and $J/\psi \to \mu^+\mu^-$. The helicity frame $(\hat{x}_1, \hat{y}_1, \hat{z}_1)$ of the Λ particle is defined as follows:

$$\begin{aligned} \hat{z}_1 &= \vec{p}_\Lambda/|\vec{p}_\Lambda| \\ \hat{y}_1 &= (\vec{n} \times \vec{p}_\Lambda)/|\vec{n} \times \vec{p}_\Lambda| \\ \hat{x}_1 &= \hat{y}_1 \times \hat{z}_1 \end{aligned} \tag{1.20}$$

where $\vec{p}_\Lambda$ is the momentum of Λ in the rest frame of Λ_b. The angles θ_p and ϕ_p are the polar and the azimuthal angles, respectively, of the proton direction in the rest frame of Λ. Analogously, the helicity frame of the J/ψ particle $(\hat{x}_2, \hat{y}_2, \hat{z}_2)$ is defined as

$$\begin{aligned} \hat{z}_2 &= \vec{p}_{J/\psi}/|\vec{p}_{J/\psi}|, \\ \hat{y}_2 &= (\vec{n} \times \vec{p}_{J/\psi})/|\vec{n} \times \vec{p}_{J/\psi}|, \\ \hat{x}_2 &= \hat{y}_2 \times \hat{z}_2, \end{aligned} \tag{1.21}$$

where $\vec{p}_{J/\psi}$ is the momentum of J/ψ in the rest frame of Λ_b. The angles θ_μ and ϕ_μ are the polar and the azimuthal angles, respectively, of the positively-charged muon direction in the rest frame of J/ψ. From the general prescription of the helicity formalism described in Section 1.5, it follows that the final density matrix ρ_f for the decay $\Lambda_b \to J/\psi(\mu^+\mu^-)\Lambda(p\pi^-)$ is of dimension 8×8. The joint angular distribution of the final-state particles involves the five angles defined above and is given by (see Eq. 1.16)

$$\frac{\mathrm{d}^5\Gamma}{\mathrm{d}\Omega_5}(\theta_\Lambda, \theta_p, \theta_\mu, \varphi_p, \varphi_\mu) = w(\theta_\Lambda, \theta_p, \theta_\mu, \varphi_p, \varphi_\mu) = \mathrm{Tr}\rho_f. \tag{1.22}$$

The angular distribution in Eq. 1.22 depends on the four helicity amplitudes $T_{\lambda_1\lambda_2}$, on the transverse Λ_b polarization P and on the parity violation asymmetry parameter α_Λ for the decay $\Lambda \to p\pi^-$. The expression obtained from the trace of the final density matrix ρ_f is very complex and rather inconvenient to be directly employed in a physics analysis. With a proper parametrization, the angular distribution can be more conveniently presented in the form of a sum of 20 terms where each term

factorizes,

$$\frac{\mathrm{d}^5\Gamma}{\mathrm{d}\Omega_5}(\theta_\Lambda,\theta_p,\theta_\mu,\varphi_p,\varphi_\mu) \sim \sum_{i=1}^{20} \eta_i(T_{++},T_{+0},T_{-0},T_{--})\ c_i(P,\alpha_\Lambda)\ f_i(\theta_\Lambda,\theta_p,\theta_\mu,\varphi_p,\varphi_\mu) \tag{1.23}$$

The expressions for η_i, c_i and f_i are listed in Table 1.1. The coefficients c_i are either equal to 1 or to a combination of the Λ_b polarization P and the asymmetry parameter α_Λ of the Λ decay. The terms f_i are trigonometric functions of the 5 angles involved in the decay, and the coefficients c_i depend on the four helicity amplitudes. Using the normalization constraint valid for the helicity amplitudes,

$$|T_{++}|^2 + |T_{+0}|^2 + |T_{-0}|^2 + |T_{--}|^2 = 1, \tag{1.24}$$

the coefficients η_i can be written in terms of the following *decay parameters*:

$$\begin{aligned}
\alpha_1 &= |T_{++}|^2 - |T_{+0}|^2 + |T_{-0}|^2 - |T_{--}|^2,\\
\alpha_2 &= |T_{++}|^2 + |T_{+0}|^2 - |T_{-0}|^2 - |T_{--}|^2,\\
\alpha_3 &= 2Re(T_{++}T^*_{+0}) - 2Re(T_{--}T^*_{-0}),\\
\alpha_4 &= 2Re(T_{++}T^*_{-0}) - 2Re(T_{--}T^*_{+0}),\\
\beta_1 &= 2Im(T_{+0}T^*_{-0}),\\
\beta_2 &= 2Im(T_{++}T^*_{--}),\\
\beta_3 &= 2Im(T_{++}T^*_{+0}) - 2Im(T_{--}T^*_{-0}),\\
\beta_4 &= 2Im(T_{++}T^*_{-0}) - 2Im(T_{--}T^*_{+0}),\\
\gamma_0 &= |T_{++}|^2 - 2|T_{+0}|^2 - 2|T_{-0}|^2 + |T_{--}|^2,\\
\gamma_1 &= 2Re(T_{+0}T^*_{-0}),\\
\gamma_2 &= 2Re(T_{++}T^*_{--}),\\
\gamma_3 &= 2Re(T_{++}T^*_{+0}) - 2Re(T_{--}T^*_{-0}),\\
\gamma_4 &= 2Re(T_{++}T^*_{-0}) - 2Re(T_{--}T^*_{+0}),\\
\delta_1 &= 2Im(T_{++}T^*_{+0}) + 2Re(T_{--}T^*_{-0}),\\
\delta_2 &= 2Im(T_{++}T^*_{-0}) + 2Re(T_{--}T^*_{+0}).
\end{aligned} \tag{1.25}$$

Details on how the angular distribution is obtained in the form of Eq. 1.23 can be found in Ref. [46] and [45].

1.6.2 Treatment of particles and antiparticles

The angular distributions described by the terms in Table 1.1 are explicitly related to the decay $\Lambda_b \to J/\psi(\mu^+\mu^-)\Lambda(p\pi^-)$. Several considerations have to be taken into account for the case of the conjugated decay $\overline{\Lambda}_b \to J/\psi(\mu^+\mu^-)\overline{\Lambda}(\bar{p}\pi^+)$.

Polarization

The polarizations of Λ_b and $\overline{\Lambda}_b$ are not necessarily equal since their production mechanisms are not identical. This therefore requires particle and antiparticle decays to be treated separately.

i	η_i	c_i	f_i
1	1	1	1
2	α_2	α_Λ	$\cos\theta_p$
3	$-\alpha_1$	P	$\cos\theta_\Lambda$
4	$-(1+2\gamma_0)/3$	$\alpha_\Lambda P$	$\cos\theta_\Lambda\cos\theta_p$
5	$\gamma_0/2$	1	$(3\cos^2\theta_\mu - 1)/2$
6	$(3\alpha_1 - \alpha_2)/4$	α_Λ	$\cos\theta_p(3\cos^2\theta_\mu - 1)/2$
7	$(\alpha_1 - 3\alpha_2)/4$	P	$\cos\theta_\Lambda(3\cos^2\theta_\mu - 1)/2$
8	$(\gamma_0 - 4)/6$	$\alpha_\Lambda P$	$\cos\theta_\Lambda\cos\theta_p(3\cos^2\theta_\mu - 1)/2$
9	$-3\alpha_3/(2\sqrt{2})$	P	$\sin\theta_\Lambda\sin\theta_\mu\cos\theta_\mu\cos\varphi_\mu$
10	$3\delta_1/(2\sqrt{2})$	P	$\sin\theta_\Lambda\sin\theta_\mu\cos\theta_\mu\sin\varphi_\mu$
11	$3\alpha_4/(2\sqrt{2})$	α_Λ	$\sin\theta_p\sin\theta_\mu\cos\theta_\mu\cos(\varphi_\mu + \varphi_p)$
12	$-3\delta_2/(2\sqrt{2})$	α_Λ	$\sin\theta_p\sin\theta_\mu\cos\theta_\mu\sin(\varphi_\mu + \varphi_p)$
13	$-3\gamma_1/2$	$\alpha_\Lambda P$	$\sin\theta_\Lambda\sin\theta_p\sin^2\theta_\mu\cos\varphi_p$
14	$3\beta_1/2$	$\alpha_\Lambda P$	$\sin\theta_\Lambda\sin\theta_p\sin^2\theta_\mu\sin\varphi_p$
15	$-3\gamma_2/4$	$\alpha_\Lambda P$	$\sin\theta_\Lambda\sin\theta_p\sin^2\theta_\mu\cos(2\varphi_\mu + \varphi_p)$
16	$3\beta_2/4$	$\alpha_\Lambda P$	$\sin\theta_\Lambda\sin\theta_p\sin^2\theta_\mu\sin(2\varphi_\mu + \varphi_p)$
17	$-3\gamma_3/(2\sqrt{2})$	$\alpha_\Lambda P$	$\sin\theta_\Lambda\cos\theta_p\sin\theta_\mu\cos\theta_\mu\cos\varphi_\mu$
18	$3\beta_3/(2\sqrt{2})$	$\alpha_\Lambda P$	$\sin\theta_\Lambda\cos\theta_p\sin\theta_\mu\cos\theta_\mu\sin\varphi_\mu$
19	$-3\gamma_4/(2\sqrt{2})$	$\alpha_\Lambda P$	$\sin\theta_\Lambda\sin\theta_p\sin\theta_\mu\cos\theta_\mu\cos(\varphi_\mu + \varphi_p)$
20	$3\beta_4/(2\sqrt{2})$	$\alpha_\Lambda P$	$\sin\theta_\Lambda\sin\theta_p\sin\theta_\mu\cos\theta_\mu\sin(\varphi_\mu + \varphi_p)$

Table 1.1: Functions describing the full angular distribution of the decay $\Lambda_b \to J/\psi(\mu^+\mu^-)\Lambda(p\pi^-)$ in five dimensions $(\theta_\Lambda, \theta_p, \theta_\mu, \varphi_p, \varphi_\mu)$. Based on [45].

Decay parameters

To obtain the angular distribution for the case of $\overline{\Lambda}_b$ decay, it is necessary to understand the transformation of Eq. 1.23 under parity (P) and charge (C) conjugation. Let us define P-even and P-odd combinations of the helicity amplitudes:

$$T^{\pm}_{\lambda\lambda'} = T_{\lambda\lambda'} \pm T_{-\lambda-\lambda'}. \tag{1.26}$$

In case of no final state interactions, the helicity amplitudes for the antiparticles and particles are related as

$$\overline{T}^{\pm}_{\lambda\lambda'} = \pm\,(T^{\pm}_{-\lambda-\lambda'})^*. \tag{1.27}$$

This leads to the following relations between the decay parameters in $\overline{\Lambda}_b$ and Λ_b decays, respectively:

$$\boxed{\begin{aligned} \overline{\alpha}_i &= -\alpha_i \\ \overline{\beta}_i &= \beta_i \\ \overline{\gamma}_i &= \gamma_i \\ \overline{\delta}_i &= -\delta_i \end{aligned}} \tag{1.28}$$

If final state interactions are present, then the relation between the helicity amplitudes is the following:

$$\overline{T}^{\pm}_{\lambda\lambda'} = \pm\, T^{\pm}_{-\lambda-\lambda'}, \tag{1.29}$$

which brings in the following decay parameters:

$$\boxed{\begin{aligned} \overline{\alpha}_i &= -\alpha_i \\ \overline{\beta}_i &= -\beta_i \\ \overline{\gamma}_i &= \gamma_i \\ \overline{\delta}_i &= \delta_i \end{aligned}} \tag{1.30}$$

Details about the decay parameters in CP-conjugated states can be found in Ref. [45, 47].

1.7 Strategy for Λ_b polarization measurement

The full angular distribution in Eq. 1.23 contains nine unknown parameters – one is the polarization P of Λ_b, the other eight parameters describe the four complex helicity amplitudes $T_{\lambda_1\lambda_2}$ in the decay $\Lambda_b \to J/\psi\,\Lambda$. The normalization condition on the helicity amplitudes (Eq. 1.24) and the arbitrariness of the global phase reduce the number of independent unknown parameters to seven. They can be determined simultaneously by a 5-dimensional fit to the five angular distributions $(\theta_\Lambda, \theta_p, \theta_\mu, \varphi_p, \varphi_\mu)$ which fully characterize the decay $\Lambda_b \to J/\psi(\mu^+\mu^-)\Lambda(p\pi^-)$.

Under the assumption of a uniform detector acceptance over the azimuthal angles φ_p and φ_μ, the expression for the angular distribution can be significantly simplified by integrating over φ_p and φ_μ,

$$\begin{aligned}\frac{\mathrm{d}^3\Gamma}{\mathrm{d}\Omega_3}(\theta_\Lambda, \theta_p, \theta_\mu) &= \int_{-\pi}^{\pi}\int_{-\pi}^{\pi} \frac{\mathrm{d}^5\Gamma}{\mathrm{d}\Omega_5}(\theta_\Lambda, \theta_p, \theta_\mu, \varphi_p, \varphi_\mu)\ \mathrm{d}\varphi_p\ \mathrm{d}\varphi_\mu \\ &\sim \sum_{i=1}^{8} \eta_i(T_{++}, T_{+0}, T_{-0}, T_{--})\ c_i(P, \alpha_\Lambda)\ f_i(\theta_\Lambda, \theta_p, \theta_\mu)\end{aligned} \tag{1.31}$$

The resulting expression contains just the first 8 terms from the list in Table 1.1 and employs only three out of five angular distributions, namely $\cos\theta_\Lambda$, $\cos\theta_p$ and $\cos\theta_\mu$. The number of unknown parameters involved is reduced to four: the polarization P of Λ_b, and the decay parameters α_1, α_2 and γ_0 defined through the magnitudes of the helicity amplitudes in Eq. 1.25. Simulations of the three angular distributions as defined in Eq. 1.31 are shown in Figure 1.7 for different polarizations of Λ_b – fully polarized ($P = -1$ or $+1$) and unpolarized ($P = 0$). In the shown examples, the decay parameters are fixed to $\alpha_1 = -0.3$, $\alpha_2 = -0.8$ and $\gamma_0 = -0.6$, respectively. As can be clearly seen from the plots, the polarization of Λ_b manifests as a slope in the distributions of $\cos\theta_\Lambda$. The other two angular distributions, $\cos\theta_p$ and $\cos\theta_\mu$, are not influenced by the polarization but are modeled by the decay parameters.
If the expression in Eq. 1.31 is further integrated over θ_p and θ_μ, one obtains the following simple relation involving only the distribution of $\cos\theta_\Lambda$ which is explicitly sensitive to the polarization:

$$\frac{\mathrm{d}\Gamma}{\mathrm{d}\cos\theta_\Lambda} \sim 1 - \alpha_1 P \cos\theta_\Lambda \tag{1.32}$$

The slope of the distribution is determined by the factor $\alpha_1 P$ where α_1 is the parity violation asymmetry parameter of the Λ_b decay and P is the polarization of Λ_b. Since both parameters are not known, they can not be disentangled by employing only the distribution of $\cos\theta_\Lambda$. Therefore, the simultaneous observation of at least three angular distributions is required ($\cos\theta_\Lambda, \cos\theta_p, \cos\theta_\mu$) in order to measure the polarization P and the asymmetry parameter α_1 by employing Eq. 1.31. The angular distribution also involves the well-measured asymmetry parameter $\alpha_\Lambda = 0.641 \pm 0.013$ [16] for the decay $\Lambda \to p\pi^-$.

The charge conjugated decay $\overline{\Lambda}_b \to J/\psi(\mu^+\mu^-)\ \overline{\Lambda}(\overline{p}\pi^+)$ is characterized by the corresponding decay parameters as defined in Eq. 1.30. The asymmetry parameter $\alpha_{\overline{\Lambda}}$ for the decay $\overline{\Lambda} \to \overline{p}\pi^+$ is assumed to have the same magnitude as α_Λ, so that $\alpha_{\overline{\Lambda}} = -\alpha_\Lambda$. The assumption is based on expectations for negligible CP-violation effects in the Λ decays within the Standard Model [48] and the fact that the current measurement precision of the parameter α_Λ is significantly better than for $\alpha_{\overline{\Lambda}}$.

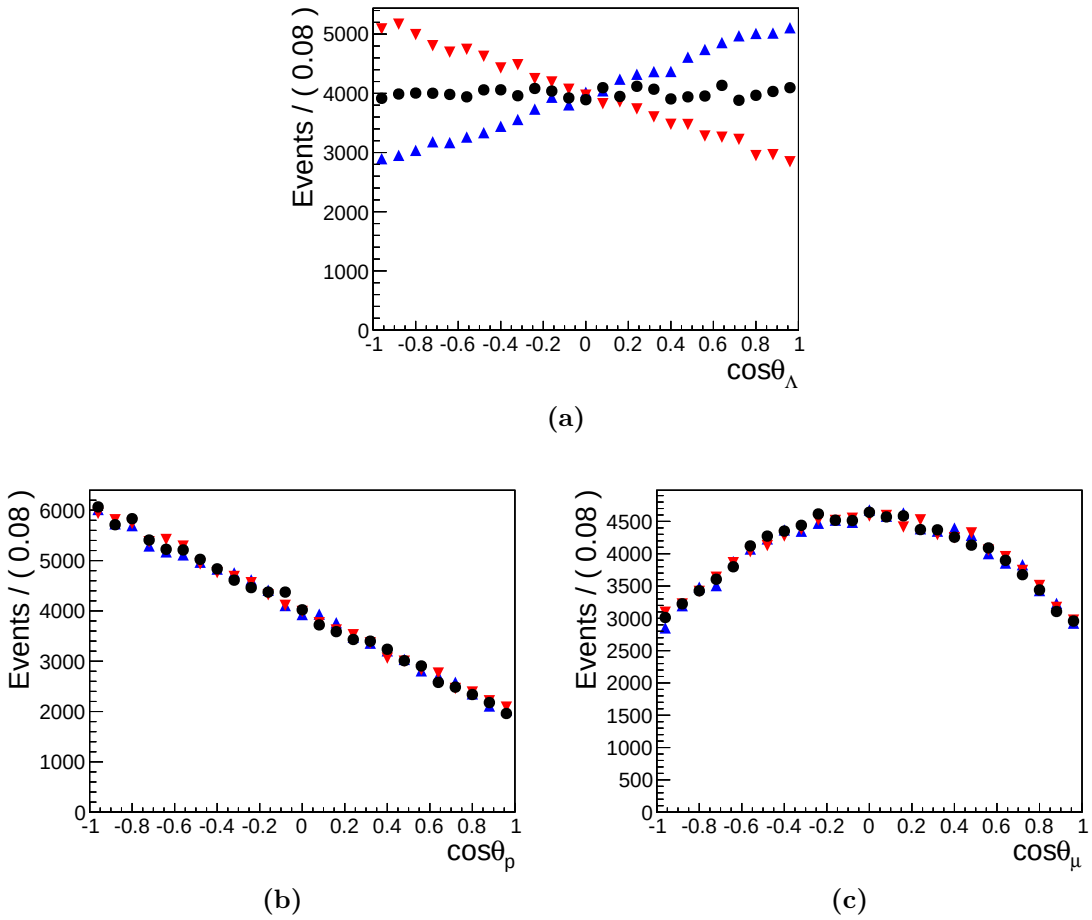

Figure 1.7: Simulations of the angular distributions in the Λ_b decay according to Eq. 1.31 for three different polarizations of Λ_b: $P = 0$ (black circles), $P = 1$ (blue triangles) and $P = -1$ (red triangles). The Λ_b polarization manifests itself in the slope of the distribution of $\cos\theta_\Lambda$ and does not influence the distributions of $\cos\theta_p$ and $\cos\theta_\mu$.

Chapter 2

LHC and the CMS experiment

2.1 The Large Hadron Collider

The Large Hadron Collider (LHC) is the flagship project of the European Organization for Nuclear Research (CERN). It is a circular particle accelerator and collider with a circumference of 27 km, located at the Swiss-French border in a tunnel at a depth ranging from 50 m to 175 m below the surface. The underground facility was initially constructed for the Large Electron-Positron collider (LEP) which was in operation from 1989 until 2000 [49]. LHC [50] is the most powerful collider to date, designed to provide proton-proton and heavy ions ($^{208}\mathrm{Pb}^{82+}$) collisions at the center-of-mass energies $\sqrt{s} = 14$ TeV and 1148 TeV respectively. Protons are first accelerated to the energy of 450 GeV by a complex of smaller accelerators – LINAC2, PSB, PS and SPS (Figure 2.1). They are then injected in the LHC in two particle beams, circulating in opposite direction in separate vacuum pipes, and are further accelerated by 400 MHz radio frequency systems. The beam particles are split in packets called bunches. The trajectories of the accelerated particles are bent by a strong magnetic field produced by superconducting dipole magnets operating at a temperature of 1.9 K. The nominal collision energy of $\sqrt{s} = 14$ TeV corresponds to a field of 8.3 T requiring a current of 12 kA in the dipole magnets.

The two oppositely circulating beams collide at four interaction points around the accelerator ring, where the four major experiments of LHC are located (Figure 2.1):

- **CMS** (**C**ompact **M**uon **S**olenoid) [51] and **ATLAS** (**A** **T**oroidal **L**HC **A**pparatu**S**) [52]: two general purpose experiments with different detector design and main focus on Higgs boson searches.

- **LHCb** (**L**arge **H**adron **C**ollider **b**eauty experiment) [53]: dedicated to precision measurements in b-quark physics, focused on CP violation studies and

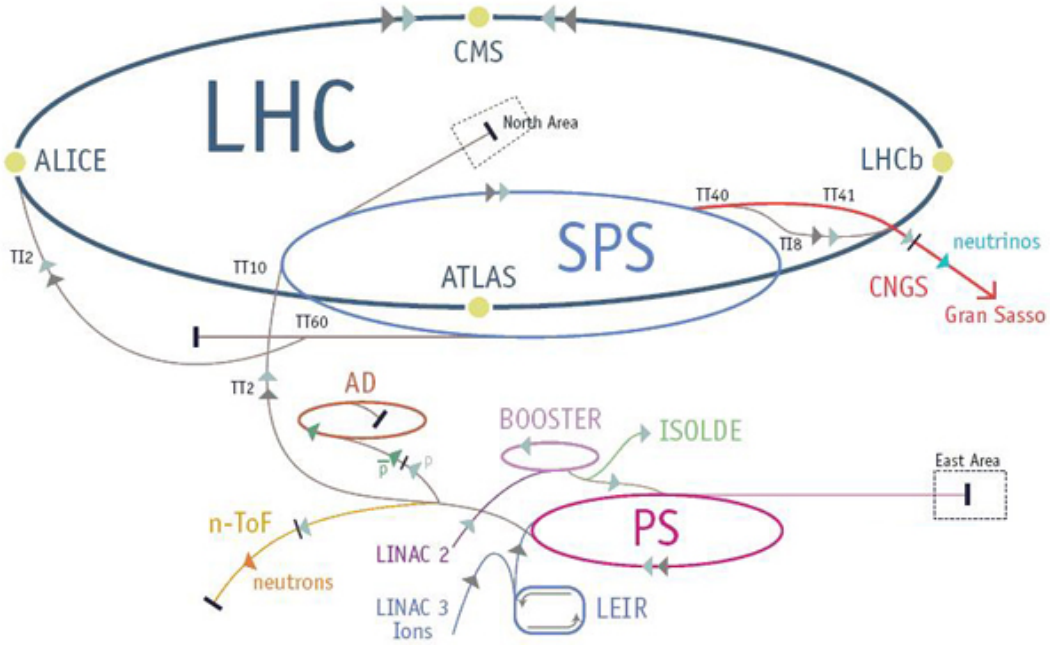

Figure 2.1: Schematic view of the LHC accelerator chain and its four major experiments: CMS, ATLAS, LHCb and ALICE. Sketch taken from the LHC website [55].

searches for *New Physics* in rare decays.

- **ALICE** (**A** **L**arge **I**on **C**ollider **E**xperiment) [54]: designed for quark-gluon plasma searches at extreme energy densities produced in heavy ion collisions (Pb, Au).

For a certain process, the number of events per second created in the collisions at LHC is given by the process cross section σ_{event} and is proportional to the machine instantaneous luminosity L:

$$N_{event} = L\ \sigma_{event} \tag{2.1}$$

The instantaneous luminosity L is entirely determined by the machine parameters:

$$L = \frac{n_b N_b^2 f}{\sigma_x \sigma_y} F, \tag{2.2}$$

where n_b is the number of bunches per beam, N_b is the number of particles per bunch, f is the bunch crossing frequency, $\sigma_{x,y}$ is the transverse beam size assuming

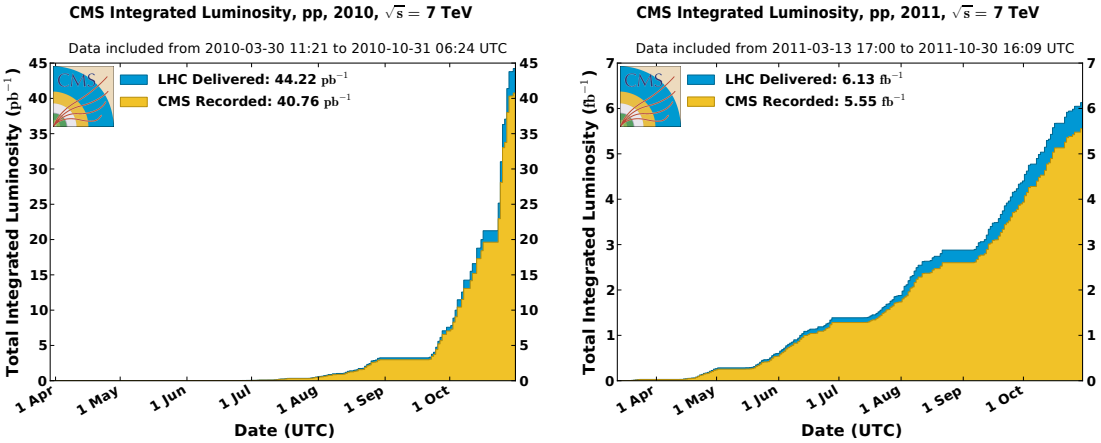

(a) Integrated luminosity in 2010 **(b)** Integrated luminosity in 2011

Figure 2.2: Total integrated luminosity delivered by LHC (blue) and recorded by CMS (yellow) in 2010 (left) and 2011 (right) [56]. The increase of delivered data in 2011 is more than a factor of 100 compared to 2010.

gaussian beam distribution, and F is a geometric luminosity reduction factor due to the crossing angle of the beams at the interaction point.

LHC produced its first proton-proton collisions in December 2009 at a center-of-mass energy $\sqrt{s} = 0.9$ TeV, serving as a storage ring for the protons injected at the SPS energy of 450 GeV. The energy was raised to $\sqrt{s} = 7$ TeV in 2010 and a total delivered luminosity of $\mathcal{L} \approx 50$ pb^{-1} was achieved. Throughout the data collection period in 2011 the collisions energy of LHC was maintained constant while improving the parameters of the beams in order to rise the instantaneous luminosity of the machine. As a result, the delivered integrated luminosity in 2011 increased impressively by a factor of 100, exceeding 5 fb^{-1}, as shown in Figure 2.2. Table 2.1 summarizes the main design operation parameters expected to be achieved within the next several years, and the peak values reached in 2011.

2.2 The CMS detector

2.2.1 Detector overview

The Compact Muon Solenoid (Figure 2.3) is a multi-purpose particle detector designed to cover a wide spectrum of physics analysis [58]. The name of the detector emphasizes on the main characteristics of its design – compact dimensions and highly efficient detection and measurement of muons facilitated by a solenoid magnet. The CMS detector is 15 m high and 22 m long, which makes it compact in comparison

Parameter	Design value	Peak value in 2011
Beam energy (TeV)	7	3.5
Number of bunches per beam, n_b	2802	1380
Number of protons per bunch, N_b	1.15×10^{11}	1.4×10^{11}
Bunch separation (ns)	25	50
Average number of collisions per bunch crossing	20	17
Peak luminosity ($\mathrm{cm^{-2}s^{-1}}$)	1×10^{34}	3.5×10^{33}

Table 2.1: Summary of the main LHC operation parameters: design values expected to be reached over the next few years [57] and peak values achieved during data collection in 2011.

with the other multi-purpose detector at LHC, ATLAS, which has a hight of 25 m and a length of 44 m. Despite its significantly smaller size, CMS has a weight of 12 500 tons which is almost twice the weight of ATLAS (7000 tons).

The CMS detector incorporates several subdetector layers. They are arranged in two sections – cylindrical *barrel* part along the beam direction, and *endcaps* orthogonal to the beam pipe. The closest to the beam subdetector system is the silicon pixel detector followed by the silicon tracker. Next is the calorimetry system comprising electromagnetic and hadron calorimeters. The outermost subdetector layer is the muon system. A schematic layout of CMS and its subdetectors is shown in Figure 2.3.

The utilized reference frame of the CMS detector is a cartesian right-handed coordinate system with the origin at the nominal collision point in the center of the detector. The x-axis points inward toward the center of the LHC ring, the y-axis points vertically upward to the surface, and the z-axis is along the beam. The azimuthal angle φ is measured from the x-axis in the x-y plane transverse to the beam and is defined as

$$\varphi = \arctan\left(\frac{y}{x}\right). \tag{2.3}$$

The radial coordinate in the x-y plane is denoted by r. The polar angle θ is measured from the z-axis and is defined as

$$\theta = \arccos\left(\frac{z}{\sqrt{x^2+y^2}}\right). \tag{2.4}$$

An often used quantity describing the direction of a particle with respect to the beam line is the pseudorapidity η defined as

$$\eta = -\ln\left[\tan\left(\frac{\theta}{2}\right)\right] \tag{2.5}$$

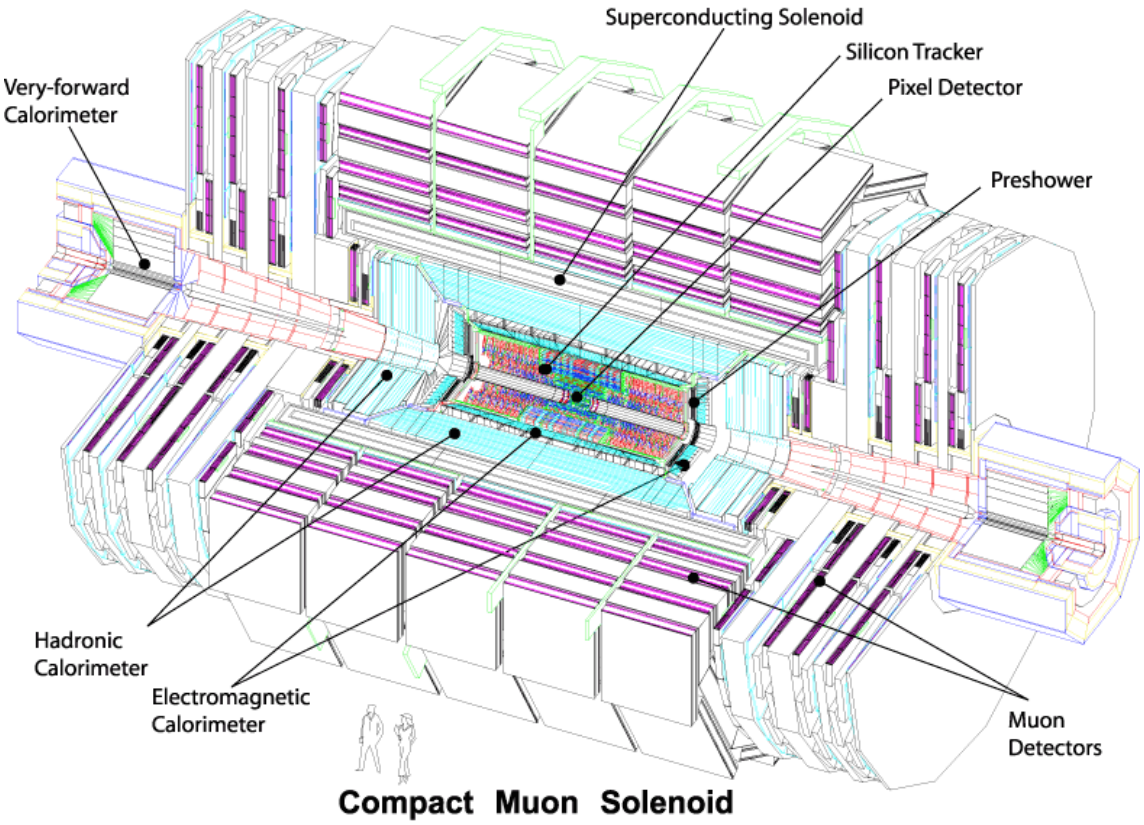

Figure 2.3: Layout of the CMS detector and its subdetector systems [51].

The following sections describe the main detector parts of CMS. An emphasis is put on the tracker and muon systems since the work presented in this thesis is based on information provided by these subdetectors.

2.2.2 Magnet

The first important decision on the CMS detector design was the choice of the magnet system [59]. The magnetic field bends the trajectories of the charged particles providing measurements of their charge and momenta and thus affects the precision of the particle mass measurements. Solenoidal field parallel to the beam was chosen for the following advantages:

- Particle tracks are bent in the transverse to the beam plane x-y. The vertex position in this plane is known with an accuracy allowing the use of triggers which are based on tracks pointing back to the vertex.

- Measurements of particle momenta start at $r = 0$.

The superconducting solenoid of the CMS experiment is the largest solenoid built to date, with a length of 13 m and an inner diameter of 6 m. It provides a homogeneous magnetic field of 3.8 T carrying a current of 20 kA at a temperature of 4.6 K.

2.2.3 Inner tracking system

The objective of the inner tracking system of CMS is to provide highly efficient and precise measurements of trajectories of charged particles in order to determine particle momenta and secondary vertices of long-lived particles, such as b-hadrons. At the design luminosity of $L = 10^{34}$ cm^{-2}s^{-1}, an average of 1000 particles will emerge at each LHC bunch crossing, i.e. every 25 ns, which requires high granularity and fast response of the detector. The tracker has to be radiation-resistant in order to sustain the hostile radiation environment near the proton beam. In addition, the amount of material needs to be minimized in order to reduce multiple scattering processes. To meet these requirements of the CMS experiment, silicon detector technology is used.

Considering the charged particle flux at different radii from the beam pipe, the inner tracking detector is divided into two parts:

- Silicon pixel detector, positioned closest to the interaction point (4 cm $< r <$ 11 cm) where a particle flux of $\sim 10^7$/s is expected at nominal luminosity of LHC.

- Silicon strip detector, located at $r > 20$ cm, where the particle flux is sufficiently low to allow the use of larger detector strips instead of pixels.

Details on the silicon detectors of CMS are given in the following sections.

Silicon pixel detector

The silicon pixel detector is the innermost and closest to the beam subdetector of CMS. It consists of a cylinder-shaped barrel section and forward (endcap) part at both sides (Figure 2.4a). The barrel [60] comprises three cylindrical layers with a length of 53.3 cm, positioned at radii $r = 4.4$ cm, 7.4 cm and 10.2 cm, respectively. Each of the three layers is made up of two half-cylinders (also called half-shells) for convenience of construction and mounting around the beam pipe. The layers comprise modular detector units (called modules) attached on carbon fiber support structures (called ladders). Each ladder supports 8 modules. Silicon sensors with a thickness of 285 μm are integrated in the modules and read out by indium bump-bonded readout chips (ROC), one module including 16 ROCs. At the edges of the half-cylinders, half-ladders are used to support eight half-modules with 8 ROCs each.

The pixel cells are designed with a rather *square* size of 100 × 150 μm^2 in order to achieve similar track resolution in r-ϕ and z directions and to allow a 3-dimensional vertex reconstruction. The total number of pixel sensors in the barrel section is 48 million.

The superconducting solenoid of CMS creates a homogeneous magnetic field in the barrel section of the pixel detector which is perpendicular to the drift direction of the created charge carriers in the sensor volume. The resulting Lorentz force leads to a side drift of the charges, spreading the collected signal charge over more than one neighboring pixels. The use of zero-suppressed readout scheme with analog pulse-height readout with charge interpolation allows a single-hit spatial resolution of ∼20 μm.

The pixel detector is completed by four endcap disks, two on each side of the barrel (Figure 2.4a). They are positioned at $z = \pm$ 35.5 cm and $z = \pm$ 48.5 cm, covering radii from 6 cm to 15 cm. The disks are split in two half-disks, each including 12 trapezoidal blades arranged in a turbine-like geometry to benefit from charge sharing due to the Lorentz drift. The silicon sensors have a rectangular shape of five sizes and a thickness of 270 μm, slightly thinner than the barrel cells. The sensors are bump-bonded to arrays of ROCs, forming the so-called plaquettes. The four endcap disks include a total of 18 million pixels.

The pixel detector provides three 3-dimensional tracking points in almost the full pseudorapidity range of -2.5 $< \eta <$ 2.5 (Figure 2.4b).

The University of Zurich has contributed to the design, construction, test and commissioning of the CMS barrel pixel detector. Measurements of the Lorentz angle in the barrel pixel sensors are presented in Chapter 3.

Silicon strip detector

The barrel section of the silicon strip tracker consists of Tracker Inner Barrel (TIB) and Tracker Outer Barrel (TOB). TIB comprises four concentric cylinders with radii from the beam axis of 22.5 cm, 33.9 cm, 41.85 cm and 49.8 cm, respectively, and covers the area from -70 cm to 70 cm in z along the beam. The silicon sensors have a thickness of 320 μm and a strip pitch varying from 80 μm to 120 μm, yielding a resolution in r-ϕ of 23-34 μm. The TOB provides 6 detection layers at radii 60.8 cm, 69.2 cm, 78.0 cm, 86.8 cm, 96.5 cm and 108.0 cm, extending from -110 cm to 110 cm in z. The silicon sensors in the outer barrel are thicker (500 μm) with a strip pitch from 120 μm to 180 μm in the different layers providing a resolution of 35-52 μm. The silicon strips alone provide measurements in r-ϕ coordinates. In order to provide measurements also in r-z, the first two layers of both TIB and TOB consist of "stereo" modules. They are equipped with a second micro-strip detector

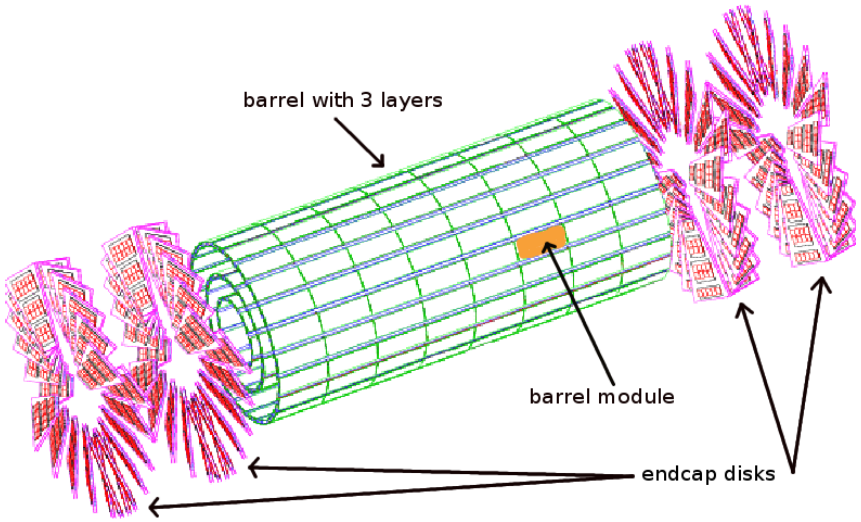

(a)

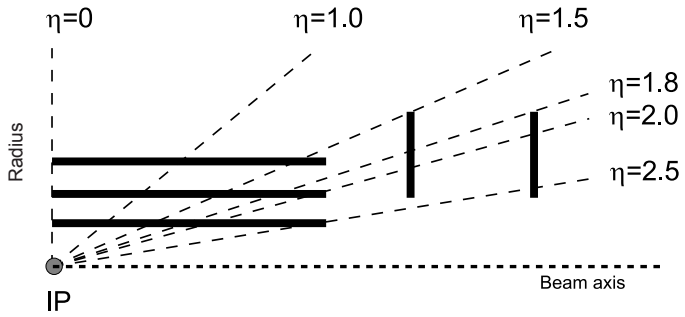

(b)

Figure 2.4: (a) Layout of the forward and barrel sections of the CMS pixel detector [61]. (b) Pseudorapidity coverage of the pixel detector [51].

module mounted back-to-back with a stereo angle of 100 mrad which provides the measurement of the second coordinate. The position resolution in z is 230 μm and 530 μm in TIB and TOB, respectively.

The forward tracker detectors are divided into Tracker End Cap (TEC) and Tracker Inner Disks (TID). The detector modules of both TEC and TID are arranged in rings with strips pointing towards the beam line, having therefore a variable strip pitch. TEC is made up of 9 disks (at each side) positioned at 120 cm $< |z| <$ 280 cm. Rings 1,2 and 5 of each TEC disk are equipped with "stereo" modules in order to provide measurements in both z and r. The sensor thickness is 320 μm for rings 1-3 and 500 μm for rings 4-9. The TID comprises 3 disks positioned in the space

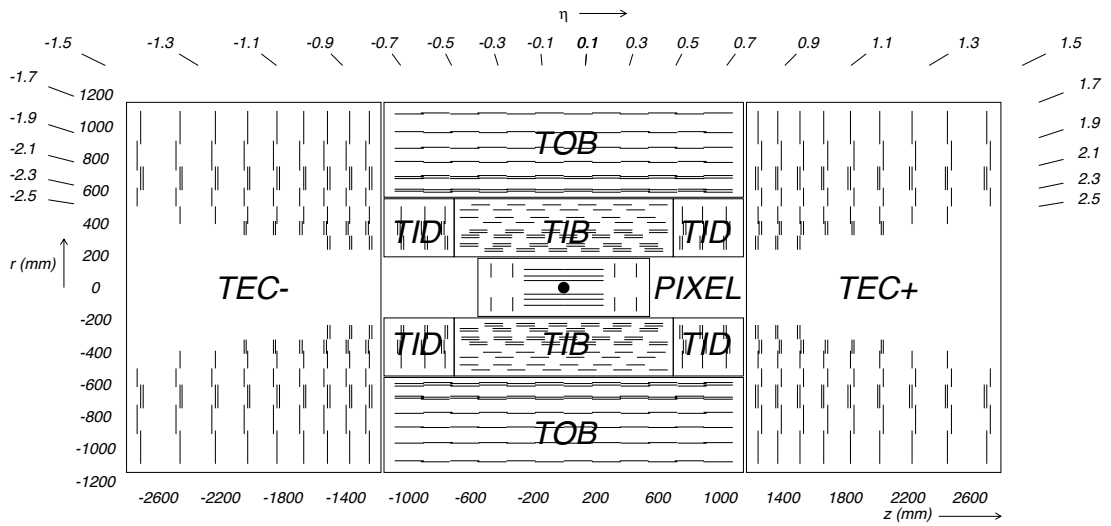

Figure 2.5: The CMS tracker: arrangement of the pixel and strip detectors and their pseudorapidity coverage [51].

between the TIB and the TEC. The sensors of the TID have a thickness of 320 μm and the two innermost rings provide "stereo" measurements. A drawing of the CMS tracker showing the arrangement of the pixel detector and all strip tracker sections is given in Figure 2.5.

2.2.4 Electromagnetic calorimeter

The electromagnetic calorimeter (ECAL) of CMS measures the energy deposit of electromagnetically interacting particles. The ECAL [62] is made of lead tungstate ($PbWO_4$) scintillating crystals. The choice of this material is based on its short radiation length ($X_0 = 0.89$ cm) and Moliere radius ($r = 2.2$ cm), quick response time (less than 25 ns) and radiation resistance. These advantages come at the price of relatively low light yield (30 photons per 1 MeV) and demand for the use of photodetectors with large intrinsic gain. The ECAL is divided into a barrel part positioned 1.3 m from the beam line, and endcaps located at $z = \pm 3.14$ m from the nominal interaction point, providing a total coverage in pseudorapidity up to $|\eta| < 3$. The size of the crystals is $22 \times 22 \times 230$ mm^3 in the barrel part, and $28.6 \times 28.6 \times 220$ mm^3 in the endcaps, equivalent to $25.8X_0$ and $24.7X_0$, respectively. The emitted scintillation light is detected by silicon avalanche photodiodes (APDs) in the barrel section and by vacuum phototriodes (VPTs) in the endcaps.

2.2.5 Hadron calorimeter

The last and outermost subdetector housed inside the inner coil of the solenoid of CMS is the hadron calorimeter (HCAL) [63]. Its main task is to measure the energy of hadrons produced in the *pp* collisions and to stop their further way through the detector. The HCAL of CMS is a sampling calorimeter with alternating layers of brass and plastic scintillator. The barrel and the two endcap sections cover a pseudorapidity range of $|\eta| < 3.0$. An outer barrel calorimeter, located outside the solenoid coil, samples the energy of late started hadron showers using the material of the solenoid as an additional absorber. Thus the total effective thickness of the hadron calorimetry is 10 interaction lengths. The scintillation light is read out by wavelength-shifting plastic fibers. The pseudorapidity coverage is further extended to $3 < |\eta| < 5$ by very forward Cherenkov-based calorimeters positioned 11.2 m from the nominal interaction point.

2.2.6 Muon system

As the name of the experiment indicates, the identification and momentum measurement of muons is a specially dedicated subject in the design and operation of CMS. Three types of gaseous detectors are used (shown in Figure 2.6) to fulfill the different requirements in the barrel and endcap environment.

The large area of the barrel is equipped with drift tube chambers (DTs) covering a pseudorapidity range $|\eta| < 1.2$. They are suitable for the low muon rate (less than 1 Hz/cm^2) and low residual magnetic field (less than 1 T) in this part of the detector. The chambers are arranged in four coaxial cylindrical layers (stations MB1 to MB4) located within the magnet return yoke at radii 4 m to 7 m from the beam line. The chambers in the first three layers (MB1 to MB3) comprise 12 planes of aluminum drift tubes in the following order: 4 measuring coordinates in the r-ϕ plane, 4 providing measurements in z and the last four again measuring in r-ϕ. Thus, each chamber provides 12 measurements per track resulting in a vector with a precision better than 100 μm in position and 1 mrad in direction. The fourth layer (station MB4) does not include any z-measuring planes. The total number of measured points for a single track crossing all layers is 44 (12 + 12 + 12 + 8) from which a muon track candidate is formed.

In the forward region, where the muon rate and the residual magnetic fields are significantly higher with respect to the barrel, cathode strip chambers (CSCs) are installed with a coverage in pseudorapidity of $0.9 < |\eta| < 2.4$. The CSCs are arranged in 4 disks (stations) in each endcap with cathode strips running radially outward to provide measurements in the r-ϕ plane. The anode wires, running approximately perpendicular to the strips, are read out to measure the pseudorapidity of the muon.

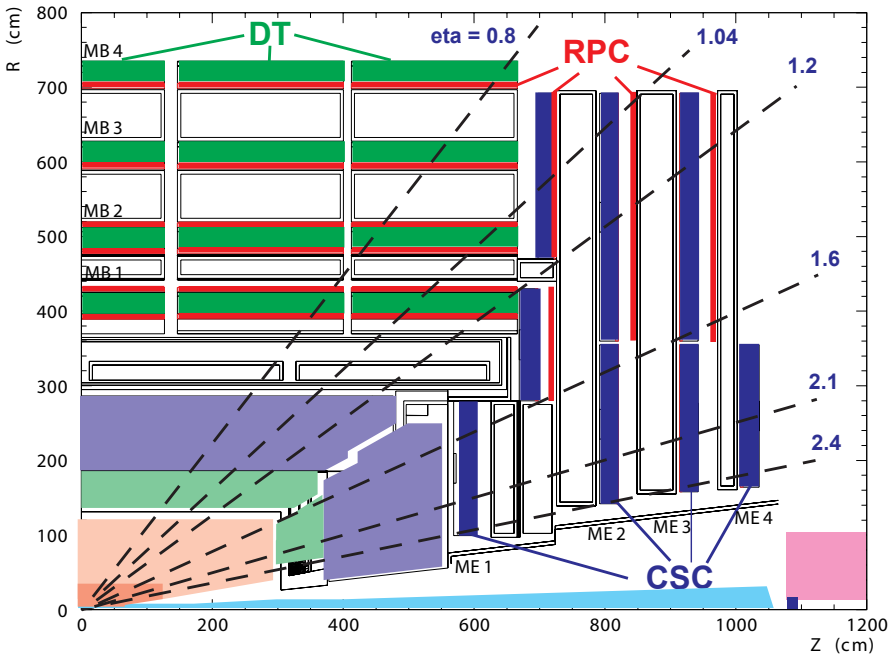

Figure 2.6: Schematic layout of the CMS muon system [61]. The three utilized types of gaseous detectors are shown (DTs, CSCs, RPCs). Dashed lines mark different pseudorapidities $|\eta|$.

The precision provided by each chamber is better than 200 μm for the position and of the order of 10 mrad for the φ angle.

The muon system is complemented by fast resistive plate chambers (RPCs), both in the barrel and in the endcaps. The RPCs have a good time resolution but poor position resolution with respect the DTs and CSCs. Their fast response is used for triggering on the muons and to determine the corresponding bunch crossing.

2.2.7 Trigger system and data acquisition

At nominal operation of LHC, bunch crossings will take place every 25 ns corresponding to a rate of 40 MHz. The size of one zero-suppressed event after digitization is ~1 MB, leading to a data production rate of ~40 TB/s. The present maximum achievable output rate is limited by the computing facilities available for prompt reconstruction and is ~300 Hz, i.e. ~300 bunch crossings/second. This is the bandwidth that has to be shared among all analysis from the rich physics program of CMS. Thus a rejection factor of $\sim 10^5$ has to be accomplished by the CMS trigger system.

The large event rate reduction is done in two steps, namely the Level-1 (L1) trigger and the High-Level trigger (HLT). Even though LHC has not reached its nominal operation parameters yet, the current bunch separation of 50 ns and instantaneous luminosity of 10^{33} $cm^{-2}s^{-1}$ have already made the operation of the trigger system extremely demanding.

Level-1 trigger

The Level-1 system [64] is a hardware trigger reducing the event rate from 40 MHz down to 100 kHz. The accept/reject decision is based on proto-objects of photons, electrons, muons and jets using coarse, low granularity information for the event from the calorimetry and muon systems and employs transverse momentum/energy thresholds. Signals from the inner tracker would require intricate and time-consuming processing and are thus not used at this stage. The L1 system must be able to issue a decision and to accept a next event every 25 ns. The decision-making time allocated for one bunch crossing is approximately 3.2 μs during which time the full high resolution event data is kept in pipelined memories in the front-end electronics. If an "accept" is issued, the full event information is sent for further processing by the High-Level trigger.

High-Level trigger

The High-Level trigger [65] has the task to further reduce the incoming from Level-1 trigger rate of 100 kHz down to ∼300 Hz. Given an "accept" decision from L1, the Data Acquisition system (DAQ) reads out and passes the full event data to be processed by the HLT. The High Level trigger system comprises fast software algorithms implemented in the CMS reconstruction software framework and executed on a custom computer farm. Physics objects (e.g. muons and jets) are reconstructed with more precision and details compared to Level-1. At this stage information from the inner tracking system is used for the first time in order to obtain better momentum resolution for charged particles. With the available reconstructed objects, the accept/reject decision of the High-Level trigger is based on a trigger table which contains a list of conditions on the reconstructed physics objects. Both the algorithms and the trigger table are flexible and configurable in order to meet different CMS analysis priorities and changing running conditions from LHC. At present, ∼300 trigger algorithms are implemented and each one takes on average 50 ms per event. Upon an "accept" decision from HLT, the DAQ system transfers the event data to the storage element for full offline reconstruction.

2.3 The analysis framework of CMS

2.3.1 CMS analysis software

The information from a single triggered bunch crossing is stored in an *event*. The complete chain of event reconstruction, from data acquisition to physics analysis, is implemented in one overall software framework referred to as CMSSW (CMS Software). CMSSW is used for selection and reconstruction of events at both online (High Level Trigger) and offline stage. Event information is stored in terms of objects in C++ in data files within the ROOT analysis framework [66]. Events are processed one by one by a sequence of software modules defined and/or configured by the user. Producer modules add data products in the event in the format of C++ classes. Filter modules analyze events and keep only those fulfilling certain criteria acting as "offline triggers". Filtering is very useful in reducing a large dataset in order to keep only events suitable for a particular user's analysis. Analysis modules allow development and application of sophisticated user-defined algorithms for a certain physics analysis of interest in order to obtain more detailed and complex information, for example invariant mass, lifetime and angular distributions for a given particle. The event content is configurable and may include observed and derived products from the triggered bunch crossing (such as raw detector output), reconstruction and/or simulation products and physics analysis objects.

2.3.2 Reconstruction of tracks of charged particles

The trajectory of a charged particle traveling through the magnetic field of the CMS detector follows a helix with an axis along the magnetic field. The trajectory is described by five parameters: the curvature (ρ), the azimuthal angle (φ) and the polar angle (θ) of the track, the distance of closest approach of the track to the beam spot (i.e. the region of the proton-proton collisions) in the transverse plane (d_0) and in the longitudinal direction (z_0).

The reconstruction of tracks of charged particles is realized in four steps in the CMS reconstruction software [67]:

1. **Track seeding:** The search of tracks starts with generating seeds, each seed comprising either three hits or two hits compatible with the beam spot. A seed determines the initial estimation of the trajectory parameters and their errors.

2. **Track finding:** This step is based on a combinatorial Kalman filter technique [68]. It is first determined which tracker layers are compatible with the initial trajectory provided by the seed. The trajectory is then extrapolated from the

seed to the proper layers according to the equations of motion of a charged particle in a magnetic field. Multiple scattering effects and energy loss in the material are taken into account. At each next tracker layer the algorithm searches a hit, compatible with the predicted trajectory. If several matches are found on a layer, a separate trajectory candidate for each of them is built and the multiple trajectory candidates are grown in parallel. An additional trajectory candidate is formed to account for detector inefficiencies in case the track did not leave any hit on the particular layer. The trajectory parameters are updated on each layer taking into account the new information from a compatible or missing hit. With this iterative procedure, the trajectory candidates are propagated until the last tracker layer is reached or a (configurable) "stop condition" is fulfilled (e.g. a certain large value for the χ^2 of the trajectory or a given maximum number of detector layers with no compatible hit found). If the total number of hits associated with a track is above a (configurable) minimum value, an inward search for hits is started, excluding the hits belonging to the seed. The aim of the inward filter propagation is to search for additional compatible hits at the seeding detector layers and at the layers closer to the beam line than the seeding layers.

3. **Track cleaning:** Due to the combinatorial approach to trajectory finding, multiple trajectory candidates can be found starting from the same seed and sharing a number of same hits. At the trajectory cleaning step, the fraction of shared hits between two track candidates is calculated. If this fraction is larger than a (configurable) set value, the track with the fewer number of hits is discarded; if the two tracks have the same number of hits, the ambiguity is resolved in favor of the candidate with a lower χ^2 value.

4. **Track fitting and smoothing:** The trajectory building stage results in a collection of hits for each trajectory. The full information is only available at the last hit and might be biased by constraints applied at the seeding stage. To avoid such biases, the trajectories are re-fitted with a combination of two fits. A Kalman filter is started at the innermost hit location proceeding outward, using the trajectory estimate obtained at the seeding step. A second fit ("smoother") is initialized at the last hit location, using the full information and proceeding inwards toward the beam line. The track parameters at a given detector surface associated with a hit can then be computed from the average of the track parameters obtained from the two filters at the same detector surface.

For each event, the track reconstruction sequence described above is run multiple times in a process called *iterative tracking* [69]. After each iteration of the sequence,

the hits associated with tracks are removed thus reducing the combinatorial complexity for the next iteration. The principal concept of the iterative tracking is that the early iterations are targeted at tracks that are easiest to find (e.g. tracks with relatively large transverse momentum), while the later iterations search for tracks which are harder to reconstruct (e.g. tracks with low transverse momentum or originating relatively away from the primary interaction point).

2.3.3 Muon reconstruction

At proton-proton collisions at CMS, tracks are first reconstructed using only the inner tracker (*tracker tracks*) and employing only the muon system (*standalone-muon tracks*). Based on these two independent classes of objects, muon reconstruction is performed in two manners:

- **Global muons:** Reconstruction proceeds outside-in matching each standalone-muon track to a tracker track. Hits from the two segments are combined and fit with the Kalman filter method to form a global-muon track. Typically segments in at least two muon stations are required. Because of the small trajectory curvature for muons with large transverse momentum ($p_T \gtrsim 200$ GeV), a global fit improves the momentum resolution with respect to a tracker-only fit.

- **Tracker muons:** Tracker tracks are extrapolated to the muon system in a search for at least one matching muon segment (hits from a drift tube or a cathode strip chamber). Magnetic field, energy loss and multiple scattering are taken into account. Tracker muon reconstruction is more efficient at low momenta ($p \lesssim 5$ GeV) compared to the global reconstruction due to its looser requirements regarding matched muon segments.

About 99% of the produced in the collisions muons that fall within the geometrical acceptance of the detector and have a momentum $p \gtrsim 3$ GeV are successfully reconstructed as Global muons, Tracker muons or both. A further muon selection provides a balance between reconstruction efficiency and rate of mis-identified muons that is to be decided depending on the specifics of the particular physics analysis. However, there is a common selection adopted in b-physics analyses at CMS which are typically using low momenta muons (*soft muons*) [70] with respect to e.g. Z, W and Higgs analysis. The efficiency to reconstruct and identify a soft muon with a transverse momentum larger than a few GeV/c is above 95% over the entire pseudorapidity range $|\eta| < 2.4$ of CMS (Figure 2.7). The relative transverse momentum resolution for muons with a transverse momentum up to 100 GeV/c is in the range from 1% to 6% depending on pseudorapidity.

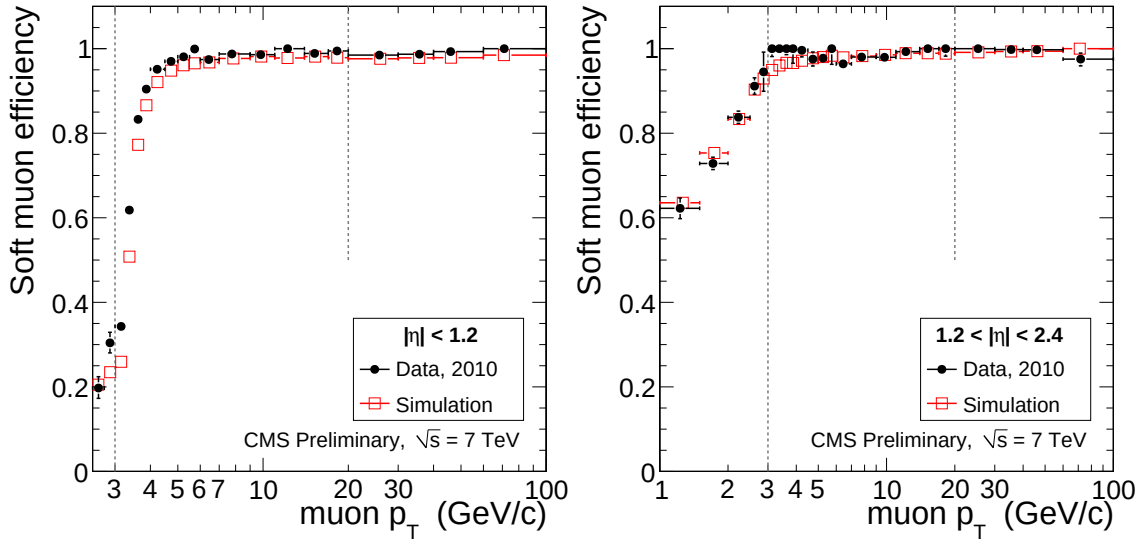

(a) **(b)**

Figure 2.7: Reconstruction and identification efficiency for muons in data and simulation in the barrel (left) and endcaps (right) of the detector. The applied selection of the muons (*soft muons*) is optimized for b-physics analysis at CMS [70].

2.3.4 Primary vertex reconstruction

The primary vertex reconstruction has to provide a precise determination of the proton-proton interaction point. Except for the early data collected in 2010, multiple proton-proton collisions in the same bunch crossing take place, called pile-up events. Therefore, for each bunch crossing multiple collision points have to be determined and tracks assigned to each of them. The primary vertex reconstruction at CMS is realized in three separate steps described below.

1. **Selection of tracks**
   At this first step, tracks originating from the primary interaction region are selected. Requirements are imposed on the significance of the transverse impact parameter of the tracks with respect to the beam spot, where the significance is defined as the ratio of a given parameter value and its error. In addition, to assure the use of well reconstructed tracks, requirements on the normalized χ^2 of the tracks and the number of hits in the pixel and strip detector are applied.

2. **Primary vertex finding**
   The default primary vertex finding algorithm used at CMS during the data taking period in 2011 is the deterministic annealing (DA) clustering [71, 72]. The

algorithm groups tracks along the beam (z) axis based on their z-coordinates at the point of closest approach to the beam line. The method is analogous to thermodynamic annealing. The *temperature* parameter is equivalent to a scale factor of the track errors. The algorithm starts at high *temperature* at which all tracks have an equal weight, i.e. no underlying structure (vertex) is yet visible. Clustering proceeds with a gradual decrease of the *temperature*, assigning each track a different weight between 0 and 1 at each iteration. When a critical *temperature* value is reached, the group of tracks is split in two. The algorithm proceeds further down to a configurable minimal value of the *temperature* parameter. Schematic representation of the deterministic annealing clustering is shown in Figure 2.8. The clustering step results in a collection of vertex candidates with tracks assigned to each of them.

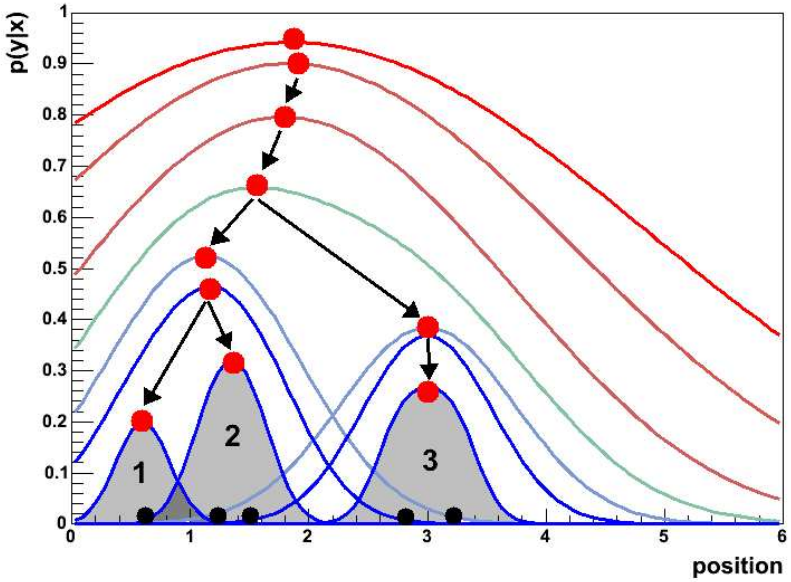

Figure 2.8: Schematic representation of the deterministic annealing clustering used for primary vertex finding: by lowering the *temperature* parameter, the maximum shifts from a symmetric one and the curve is split into two; the process continues until a certain minimal *temperature* is reached. The plot is borrowed from [73].

3. **Primary vertex fitting**
   The track list associated with each vertex candidate is further used for a 3-dimensional vertex fit. The default primary vertex fitting algorithm in CMS is the Adaptive Vertex Fitter (AVF) [74, 75]. It is an iterative re-weighted least-squares fit. The algorithm down-weights tracks according to their standardized (χ^2) distance to the vertex which makes it robust against outlying

tracks coming from other vertices. The assigned weights are fractional (so-called soft assignment) and vary at each next iteration until the fit converges. The fit produces two collections of reconstructed primary vertices created with and without a beam spot constraint.

2.3.5 Vertex reconstruction in particle decays

Reconstruction of vertices originating from particle decays in some aspects differs from the reconstruction of primary vertices. Contrary to the primary vertex case, the number of tracks to be fit is exactly known and it is in general a small number (most often two to five tracks). The step of vertex finding is therefore not realized through a track clustering algorithm but the tracks to be fit are directly fed to a vertex fitting algorithm. The Adaptive Vertex Fitter described in Section 2.3.4 is optimized for down-weighting outliers and is thus particularly well suited for fitting vertices with a large number of tracks, such as primary vertices. For the presented in this thesis analysis, two vertex fitting algorithms are utilized for the reconstruction of exclusive particle decays – Kalman vertex fit and kinematic vertex fit.

Kalman vertex fit

The Kalman vertex fitter (KVF) uses the Kalman filter algorithm [76, 68]. KVF is a linear (least-squares) fit in which all tracks enter with an equal (unit) weight and is mathematically equivalent to a global least-squares minimization. It is the optimal algorithm for linear models with Gaussian distributed errors. The fit can also provide an improved measurement of the track parameters constrained by the vertex and the covariance matrices of the tracks [77].

Kinematic vertex fit

The kinematic vertex fit [78] is a least-squares minimization algorithm with constraints derived from physics laws (e.g. conservation of mass, energy and momentum). The constraints are mathematically included in the minimization by Lagrange multipliers [79]. The purpose of the kinematic fit is to improve the resolution (i.e. the precision) of the measured parameters by involving physics laws into the minimization problem.

Chapter 3

Measurements of the Lorentz angle in the CMS silicon pixel sensors

3.1 Introduction

Charged particles traversing the volume of a silicon detector produce electron-hole pairs by ionization. The applied bias voltage causes the charges to drift towards the surface of the sensors where they are read out. The silicon pixel detector of CMS operates in an environment with a magnetic field of 3.8 T. For the barrel section, the uniform magnetic field is perpendicular to the electric field applied in the pixel sensors. The produced charge carriers therefore experience the Lorentz force. As shown schematically in Figure 3.1, instead of moving towards the surface of the sensor along the direction of the electric field, the charges are deviated by the Lorentz force at an angle θ_L called Lorentz angle. As a consequence, the charge deposit is spread and collected by several neighboring pixels. Due to the analog charge readout, the spatial resolution of the pixel detector can benefit from charge sharing by estimating the hit position from the center of gravity of the collected charge. The reconstructed hit position, however, has to be corrected for the shift caused by the Lorentz drift of the charge carriers.

It has been shown [81] that the Lorentz angle is significantly influenced by the operating conditions of the pixel detector, such as bias voltage and temperature. Studies with test beams have shown that at a magnetic field of 4 T the Lorentz angle is around 26° at a bias voltage of 100 V and decreases to 8° at a bias voltage of 600 V, as can be seen in Figure 3.2. Furthermore, a decrease of the temperature leads to an increase of the Lorentz angle. Throughout the operation of LHC, the accumulated radiation will affect the silicon pixel detector by increasing the number

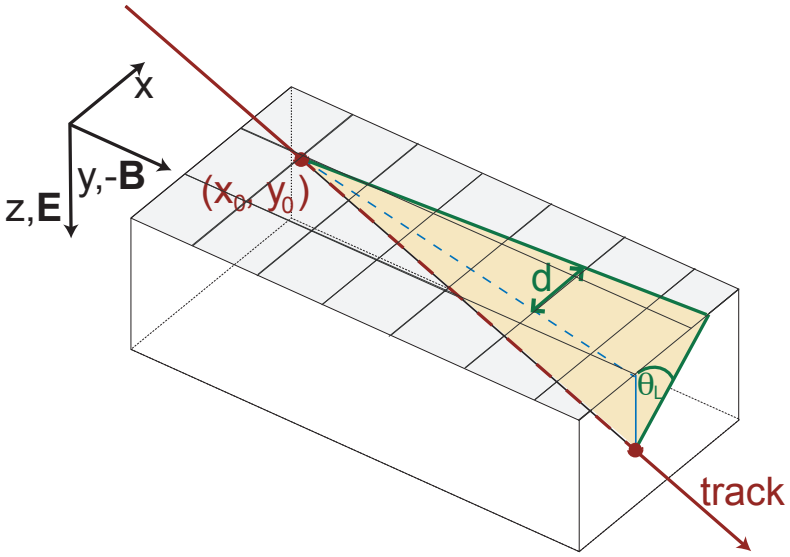

Figure 3.1: Schematic illustration of a particle track traversing the barrel pixel sensors of CMS [80]. The local coordinates (x, y, z) utilized for the pixel detector are shown. The Lorentz angle and the Lorentz drift are labeled as θ_L and d, respectively.

of defects in the silicon crystals. Trapping of charge carriers during the charge drift deteriorates the detector performance due to a decrease of the collected charge at the sensor contact surface. In order to recover the amount of collected charge, the electric field applied to the sensors has to be increased and the reconstructed hit position has to be corrected accordingly. Therefore, one of the factors which influence the position resolution of the pixel detector is the understanding of the Lorentz angle.

Under the influence of electric and magnetic fields, the transport of electrons within the silicon crystals of the detector is described by the classical equation of motion including a drag force proportional to the velocity of the electrons [82],

$$m \cdot \frac{\mathrm{d}^2\vec{r}}{\mathrm{d}t^2} = -q \cdot \frac{\mu_H}{\mu} \cdot \frac{\mathrm{d}\vec{r}}{\mathrm{d}t} \times \vec{B} - q \cdot \vec{E} - \frac{q}{\mu} \cdot \frac{\mathrm{d}\vec{r}}{\mathrm{d}t}, \tag{3.1}$$

where m is the effective electron mass, $\vec{r}$ is the location vector of the electron, q is the magnitude of the electron charge ($q = |-e|$), μ and μ_H are the drift and Hall mobilities of the electron, $\vec{B}$ and $\vec{E}$ are the magnetic and electric fields, respectively. The general solution for the electron velocity, employing the vector components in

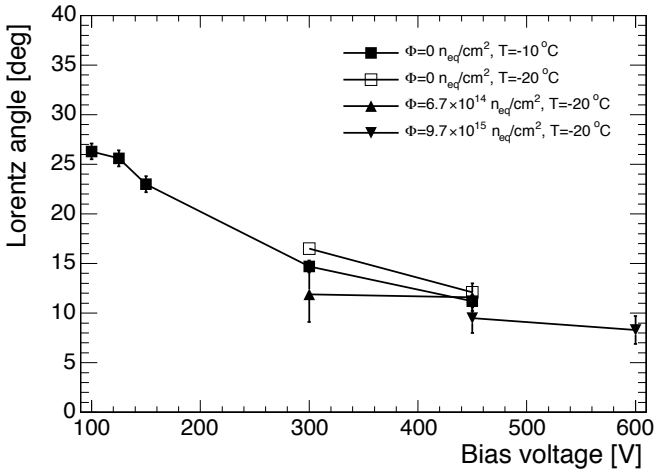

Figure 3.2: Lorentz angle as a function of bias voltage at a magnetic field of 4 T [81].

the x, y and z directions, is

$$\begin{aligned}\begin{pmatrix} v_x \\ v_y \\ v_z \end{pmatrix} = &- \frac{\mu}{1+\mu_H^2 B^2} \\ &\times \begin{pmatrix} 1+\mu_H^2 B_x^2 & \mu_H^2 B_x B_y - \mu_H B_z & \mu_H^2 B_x B_z + \mu_H B_y \\ \mu_H^2 B_x B_y + \mu_H B_z & 1+\mu_H^2 B_y^2 & \mu_H^2 B_z B_y - \mu_H B_x \\ \mu_H^2 B_x B_z - \mu_H B_y & \mu_H^2 B_z B_y + \mu_H B_x & 1+\mu_H^2 B_z^2 \end{pmatrix} \\ &\times \begin{pmatrix} E_x \\ E_y \\ E_z \end{pmatrix}\end{aligned} \tag{3.2}$$

From the sketch in Figure 3.1, it follows that the Lorentz angle in the barrel pixel detector of CMS is obtained from the relation

$$\tan\theta_L = \frac{v_x}{v_z}. \tag{3.3}$$

Accounting for the fact that in the barrel pixel detector the electric field is parallel to the local z direction and the magnetic field is antiparallel to the local y direction, the Lorentz angle is then given by the simple relation

$$\tan\theta_L = -\mu_H B = -r_H \mu B. \tag{3.4}$$

The Hall factor $r_H = \mu_H/\mu$ accounts for the effect of the magnetic field on the scattering relaxation time. The value of r_H is of the order of unity and has an uncertainty $\sim$10%. The electron mobility μ has a complex dependence on the electric

field, temperature and irradiation, which is to date not well understood [83]. As a consequence, at present calculations of the Lorentz effect are not reliable. It is therefore required to measure the Lorentz angle in situ.

This Chapter presents measurements of the Lorentz angle in the barrel pixel detector of CMS with cosmic ray muons (Section 3.2) and collision data (Section 3.3), followed by a discussion of the systematic uncertainties in Section 3.4.

3.2 Measurements of the Lorentz angle with cosmic ray data

Before the start of the LHC proton-proton program in the end of 2009, the CMS experiment collected cosmic ray data for tests and commissioning of the detector systems. Cosmic data was as well used to determine the Lorentz angle in the pixel barrel detector. The technique used to extract the Lorentz angle from cosmic ray data is the so called ***minimal cluster size method*** [84]. The method is derived from geometrical considerations and can be explained with the help of Figure 3.3. The ionization charges created by a charged particle move towards the detector surface. In the absence of a magnetic field, they would drift along the electric field which coincides with the local z-axis orientation. In the presence of orthogonal electric and magnetic fields, the charge carriers direction is deviated at an angle θ_L w.r.t. the electric field. Due to the Lorentz drift, which is along the x direction only, part of the charges can be read out by a neighboring pixel, thus extending the cluster size along the x direction. The cluster width along the y-axis is not affected by the Lorentz force. The cluster size in the x direction depends on the incident track angle α and is minimal when the track points along the drift direction of the charge carriers, i.e. $\alpha = \pi/2 + \theta_L$. This leads to the following relation:

$$\cot \alpha_{min} = -\tan \theta_L \tag{3.5}$$

where α_{min} is the incident track angle α at which the cluster width along the x-axis is minimal. The angle α is determined from the momentum components p_x and p_z of the track in the local coordinate system of the pixel detector,

$$\alpha = \arctan(p_z/p_x), \tag{3.6}$$

and is defined in the range $0 \leq \alpha \leq \pi$. The Lorentz angle can be extracted by finding the minimum in the distribution of the mean cluster size in the x direction as a function of the impact track angle α.

Tracks from cosmic muons are reconstructed with a dedicated cosmic track finding algorithm [85]. The steps are similar to the standard track reconstruction in

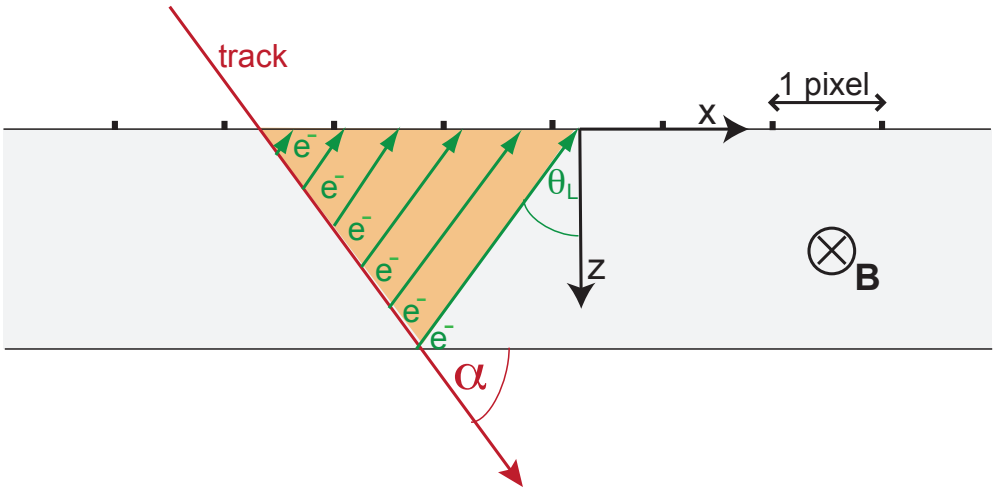

Figure 3.3: Illustration of the charge carriers drift in the silicon sensors of the barrel pixel detector. Due to the Lorentz force, the charges are deflected at an angle θ_L along the x direction, thus extending the cluster size in this line. The cluster size in the x direction depends on the incident track angle α and is minimal when the track points along the drift direction of the charge carriers. Sketch taken from [84].

collision data but are modified to match the specifics of cosmic muons. The seeding step is performed with hits from the TIB and TOB sections of the tracker. The pattern recognition proceeds inwards toward the beam line, followed by a final fitting step performed with the Kalman filter.

The information necessary to measure the Lorentz angle with the cluster size method includes the impact angles of the tracks and the properties of the hits which they create in the barrel pixel detector. A number of requirements are imposed, as described below.

- In order to select reconstructed tracks with well-determined parameters, it is required that their reduced χ^2 per degree of freedom is $\chi^2/\text{ndof} < 2$ (see Figure 3.4).

- It has been observed [86] that in cosmic ray events the hit detection efficiency for single-pixel hits is lower w.r.t. larger clusters. In order to select well-defined clusters, single-pixel hits are excluded. However, a requirement on the total number of pixels forming the cluster would introduce a bias in the measured cluster width in the x direction, which must be avoided. Therefore, the requirement is applied only along the y direction, imposing a cluster size in y of at least 2 pixels.

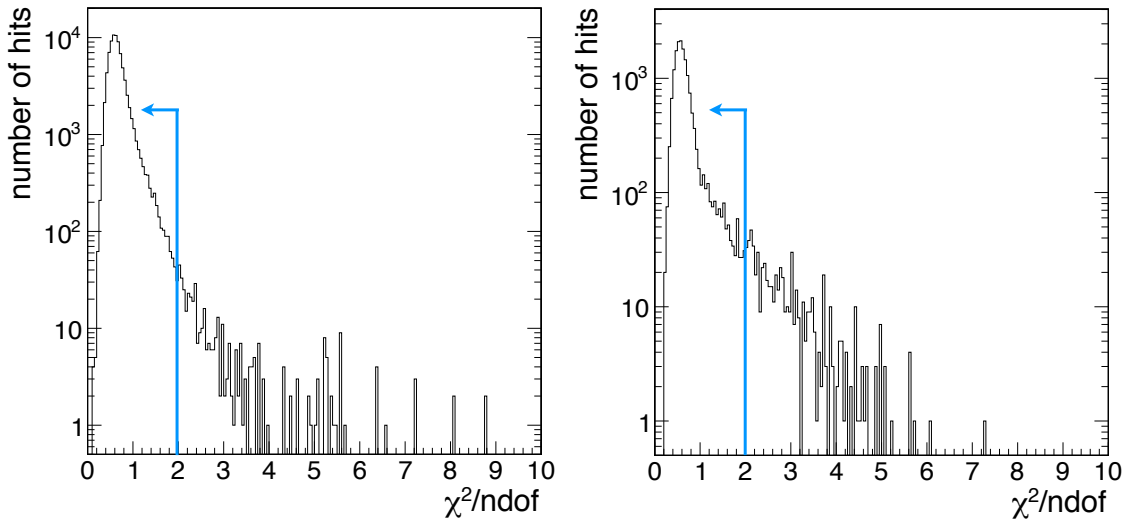

(a) **(b)**

Figure 3.4: Reduced χ^2 per degree of freedom for cosmic muon tracks. Only tracks with $\chi^2/\text{ndof} < 2$ are used for the Lorentz angle measurement. (a) Data collected at nominal magnetic field of 3.8 T. (b) Data collected without magnetic field.

- The boundaries of the readout chips are equipped with pixels having twice the normal size in order to avoid dead regions between the ROCs. Hits containing such edge pixels are not used for the Lorentz angle measurement.

The selection results in approximately 80 thousand hits collected at the nominal magnetic field of 3.8 T, and 16 thousand hits collected at 0 T. For the case of nominal magnetic field, the distribution of the cluster size in the x direction as a function of $\cot\alpha$ of the incident tracks is shown in Figure 3.5a. The color scheme corresponds to the number of clusters in a certain bin. The cluster size of just one pixel along x corresponds to tracks traversing (anti)parallel to the drift direction of the charge carriers. The averaged cluster size in each bin of $\cot\alpha$ is shown in Figure 3.5b for data collected at a nominal magnetic field and without a magnetic field. The minimum of the distribution is obtained from a χ^2 fit of the function

$$f(\cot\alpha) = \begin{cases} A + \sqrt{B^2 + C^2 \cdot (\cot\alpha - \cot\alpha_{min})^2} & \text{for } \cot\alpha < \cot\alpha_{min} \\ A + \sqrt{B^2 + D^2 \cdot (\cot\alpha - \cot\alpha_{min})^2} & \text{for } \cot\alpha \geq \cot\alpha_{min} \end{cases} \tag{3.7}$$

with the following free parameters:

– A is the minimum of the cluster size in the x direction (in terms of pixels),

– B accounts for the smearing of the minimum due to detector resolution,

– C and D represent the slopes on the left and right side of the minimum, respectively,

– $\cot\alpha_{\min}$ is the value of $\cot\alpha$ corresponding to the minimum in the mean cluster size distribution.

The results of the measurements are summarized in Table 3.1. The obtained value for $\cot\alpha_{\min}$ for the case of a nominal magnetic field of 3.8 T is -0.405 ± 0.003 corresponding to a Lorentz angle $\theta_L = 22.05° \pm 0.15°$. The result from data collected in the absence of a magnetic field is compatible with a Lorentz angle of 0°, as should be expected since the Lorentz force is not present in this case. The quoted errors are statistical only. The reason for the different slopes on the left and right side of the distribution minimum when a magnetic field is present is discussed in Ref. [84]. Due to the charge readout threshold (given in number of electrons), pixels at the boundary of a cluster might be discarded if they are below the threshold. Since the Lorentz force deflects the charges in a certain direction, this effect is not symmetric and is not present in the absence of a magnetic field.

Parameter	3.8 T	0 T
$\cot\alpha_{\min}$	-0.405 ± 0.003	0.008 ± 0.007
A	1.068 ± 0.015	0.989 ± 0.036
B	0.160 ± 0.023	0.235 ± 0.050
C	2.254 ± 0.023	2.186 ± 0.052
D	2.008 ± 0.023	2.212 ± 0.053
χ^2/ndof	34.47/35	39.74/35

Table 3.1: Results for the Lorentz angle in the barrel pixel detector measured with cosmic ray data: summary of the fit parameters obtained from data taken with and without a magnetic field. The uncertainties are statistical only.

The results in Table 3.1 are obtained at the assumption of idealized pixel sensors with linearly drifting charges. A crosscheck is done with a detailed simulation of the pixel sensors with the PIXELAV software [87, 88] which takes into account effects such as realistic electric field map, charge mobility and Hall effect. The bias voltage and sensor temperature in the simulation are set to $V_{bias} = 150$ V and $T = 10$ °C corresponding to the operating conditions in the barrel pixel detector. The Lorentz angle is extracted by applying the same cluster size method on the simulated with

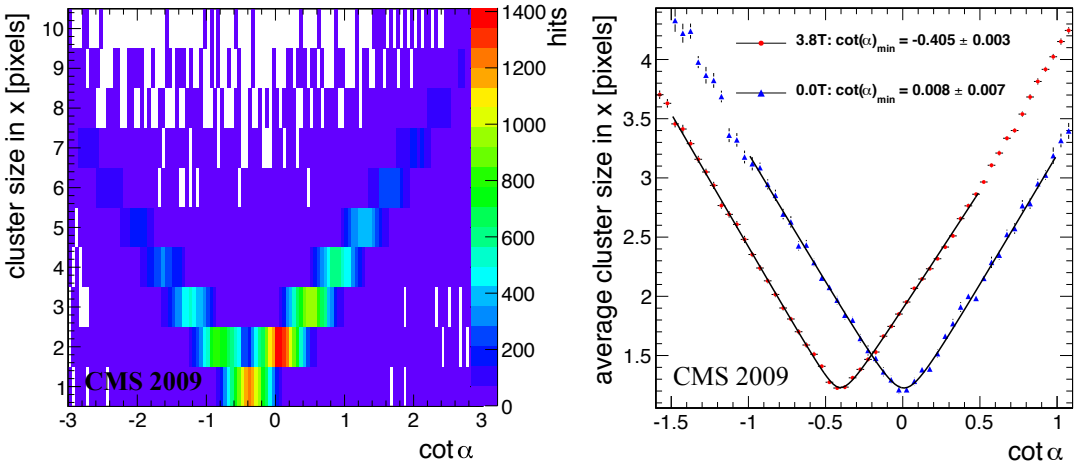

(a) **(b)**

Figure 3.5: (a) Distribution of the cluster size in the x-direction as a function of $\cot\alpha$ of the traversing tracks at a magnetic field of 3.8 T. The color scheme corresponds to the number of clusters in a histogram bin. (b) Average cluster size in the x-direction as a function of $\cot\alpha$ of the traversing tracks at a magnetic field of 3.8 T (red circles) and 0 T (blue triangles). Solid lines denote the fit (Eq. 3.7) applied to the data points.

PIXELAV sample. The results from data and simulation, summarized in Table 3.2, are in a very good agreement. However, the PIXELAV simulation is known to introduce a systematic error of up to 10% in the result due to an uncertainty on the Hall factor.

The results are compared with earlier measurements [86, 84] performed with cosmic data taken at different operation conditions of the pixel detector (see Table 3.2). An increase of the bias voltage from 100 V to 150 V combined with a decrease of the sensor temperature from 20 °C to 10 °C leads to an overall reduction of $\tan\theta_L$ from 0.462 to 0.405. This is equivalent to a decrease of the Lorentz angle θ_L from $\sim$24.80° to $\sim$22.04°. The effect is mainly due to the change of the bias voltage because, as can be seen from Figure 3.2, the temperature change has a less pronounced influence on the Lorentz angle.

It has been shown [84] that the measurement of the Lorentz angle with the minimal cluster size method has a bias and results in up to 10% larger angle than the true value. The bias is due to the assumption for linear drift of the charge carriers in the bulk of the silicon sensors. In reality, the lines of the electric field at

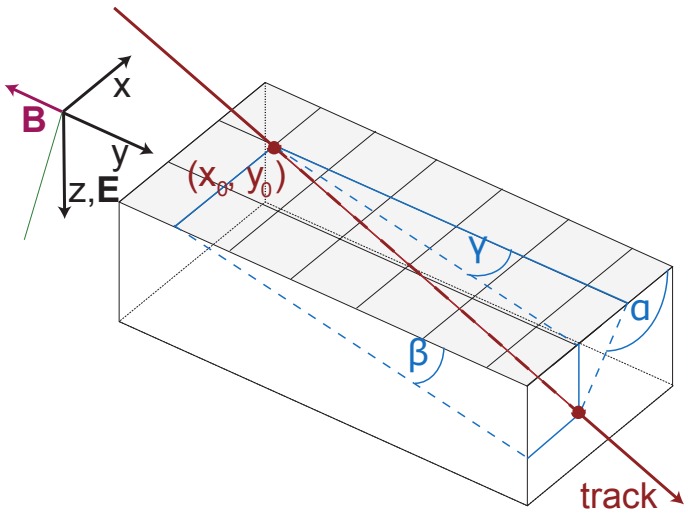

Figure 3.6: Schematic illustration of the three impact angles (α, β, γ) of an incident track traversing the barrel pixel sensors. The local coordinate system utilized for the pixel sensors is shown. Sketch borrowed from [84].

the readout contacts are distorted and the charges are focused towards the central area of the pixel cell.

			$\tan\theta_L$ at $B = 3.8$ T		$\tan\theta_L$ at $B = 0.0$ T	
year	V_{bias}	T	data	PIXELAV	data	PIXELAV
2009	150 V	10 °C	0.405 ± 0.003	0.397 ± 0.003	-0.008 ± 0.007	-0.012 ± 0.006
2008	100 V	20 °C	0.462 ± 0.003	0.452 ± 0.002	-0.003 ± 0.009	0.008 ± 0.005

Table 3.2: Summary of results for the Lorentz angle obtained from cosmic data and simulation with the minimal cluster size method. The results are compared with earlier measurements (2008) [86, 84] performed at different operation conditions of the detector. A decrease of almost 3° degrees is observed due to the increase of the bias voltage. The uncertainties are statistical only.

3.3 Measurements of the Lorentz angle with collision data

The *minimal cluster size method* discussed in the previous section requires a broad spectrum for the track impact angle α in order to provide a sufficient fit range to extract the Lorentz angle. This technique is in general not suitable for the case

of proton-proton collision data, where the impact angle α of tracks coming from the nominal collision point is in a rather narrow range around $\alpha \approx 90°$. For this reason, a dedicated technique is used to measure the Lorentz angle from collision data, known as the ***grazing angle method*** [89]. The method is based on purely geometrical considerations. It can be explained with the help of Figure 3.1 and Figure 3.6, where the three impact angles (α, β, γ) defining a track passing through the pixel detector are shown. Charged particles produce ionization charges which are read out by a series of pixels. Each pixel in the group collects charge from a certain part of the traversing particle's path and thus from a certain depth in the bulk of the detector. In the absence of a magnetic field, the charges move along the electric field direction and are read out by the pixels under which they are produced. When a magnetic field is present, due to the Lorentz force the charges reach the surface with a displacement which is proportional to their drift length. The displacement of the charge carriers is a function of the depth at which they are produced. The production depth of the charges (along the z-axis) and their displacement (along the x-axis) are calculated from the parameters of the traversing track. In order to attain multiple measurement points for the production depth, the clusters have to be long along the y-axis leading to shallow ("grazing") β impact angles of the tracks (see Figure 3.6). The tangent of the Lorentz angle is obtained from the slope of the average shift as a function of the production depth of the charge carriers.

The notations as in Ref. [80] are used. The impact point (x_0, y_0) of the track on the surface of the pixel detector is estimated by extrapolating the trajectory to each detector layer. The charge collected by each pixel from the cluster is measured as a function of the distance between the given pixel and the impact point of the track. The following quantities are defined:

$$\begin{aligned} \Delta x &= x - x_0, \\ \Delta y &= y - y_0, \end{aligned} \tag{3.8}$$

where (x, y) is the center of the pixel for which the charge is measured. The impact angles of the track are obtained from the following relations:

$$\tan\alpha = \frac{p_z}{p_x}, \tag{3.9}$$

$$\tan\beta = \frac{p_z}{p_y}, \tag{3.10}$$

$$\tan\gamma = \frac{p_x}{p_y}, \tag{3.11}$$

where p_x, p_y, p_z are the track momentum components in the local coordinate system of the pixel detector. The displacement d of the ionization charges and their

production depth z are then calculated as follows:

$$\begin{aligned} d &= \Delta x - \Delta y \cdot \tan\gamma, \\ z &= \Delta y \cdot \tan\beta. \end{aligned} \tag{3.12}$$

Finally, the Lorentz angle is given by the ratio of the charges displacement and their production depth:

$$\tan\theta_L = \frac{d}{z}. \tag{3.13}$$

The Lorentz angle in the barrel pixel detector was measured for the first time with proton-proton collision events with the very first data delivered by LHC in December 2009. During the commissioning of LHC and the CMS detector, data was collected in sets of increasingly higher center-of-mass energies and several values for the magnetic field in CMS. This allowed measurements of the Lorentz angle to be performed with collisions at a center-of-mass energy of 0.9 TeV, 2.36 TeV and 7 TeV, and a magnetic field of 2 T and 3.8 T. In theory, the Lorentz effect does not depend on the beam energy, while a linear dependance is expected on the strength of the magnetic field. Measurements performed at different beam energies and magnetic fields are of particular interest in order to verify the expected behavior of the Lorentz angle and thus to test the stability of the measurement method. The measurements serve as well as an indirect test of the tracking performance of CMS in a period when the tracking algorithms are applied for the first time on real collision data.

The following selection criteria are applied to tracks and clusters used for the measurements of the Lorentz angle with the grazing angle method:

- Tracks from any kind of charged particles can be used for the measurement. In order to avoid the lowest momentum tracks which curl up in the pixel detector volume, tracks with a transverse momentum p_T larger than 0.1 GeV/c are selected from the data samples collected at $\sqrt{s} = 0.9$ TeV and 2.36 TeV (see Figure 3.7a). A tighter requirement on the track momentum significantly reduces the dataset size. For the large data sample collected at $\sqrt{s} = 7$ TeV, a tight criterion of $p_T > 3$ GeV/c is applied to select tracks with well measured parameters. This is the only difference in the selection of tracks from the different data samples.

- To assure several measurement points in production depth, the cluster size in the y direction is required to be at least four pixels.

- Secondary electrons can lead to double clusters positioned very close to each other or even merged. In order to reject such hits, the total charge collected in a cluster is required to be less than 120 000 electrons (see Figure 3.7b).

- Clusters covering double-sized pixels from the edges of the ROCs are excluded.
- In order to select good quality tracks with well measured parameters, the reduced χ^2 per degree of freedom from the track fit is required to be $\chi^2/\text{ndof} < 2$ (see Figure 3.7c).
- The difference between the extrapolated track position on the pixel detector surface and the actual position of the hit is required to be less than 50 μm (see Figure 3.7d).

For the case of data collected at a center-of-mass energy of 900 GeV and a magnetic field of 3.8 T, the distributions of the variables used for the selection, before imposing any requirements, are given in Figure 3.7. The distribution of the production depth of the charges as a function of their displacement along the x direction is shown in Figure 3.8a. The averaged displacement in each production depth bin is shown in Figure 3.8b. The tangent of the Lorentz angle $\tan\theta_L$ is given by the slope of the average displacement distribution and is obtained by a linear fit to the data. The range of the fit is over the thickness of the pixel sensor, omitting the first and the last 50 μm in order to avoid nonlinear charge drift at the edges of the sensor.

A summary of the measurements performed with the grazing angle method is given in Table 3.3. The results from different data samples collected at center-of-mass energies of 0.9 TeV, 2.36 TeV and 7 TeV and at the nominal magnetic field of 3.8 T, are in perfect agreement – no sign of dependence on the beam energy is observed. The averaged result is $\tan\theta_L = 0.3984$ corresponding to a Lorentz angle $\theta_L = 21.7°$. The measurements performed with the same method but using data collected at a magnetic field of 2 T clearly show the dependence of the Lorentz effect on the magnetic field, resulting in $\sim$50% decrease of the Lorentz angle. The grazing angle method is as well used to extract the Lorentz angle from simulated samples provided by PIXELAV. Good agreement is observed between the results from data and from simulation.

The minimal cluster size technique described in Section 3.2 is not optimal for the measurement of the Lorentz angle with collision data. The reason is the rather limited range of values for the track impact angle α for tracks coming from the nominal interaction point. However, the large population of low transverse momentum tracks in minimum bias events, recorded during the initial period of LHC beam commissioning, provides highly curved tracks with a large acceptance in $\cot\alpha$. This allows the application of the minimal cluster size method on collision data as a complementary test utilizing a second measurement technique on the same sample of events. The same selection criteria are applied as for cosmic ray data (see Section 3.2). An additional requirement for a track $p_T > 0.1$ GeV/c is imposed to reject

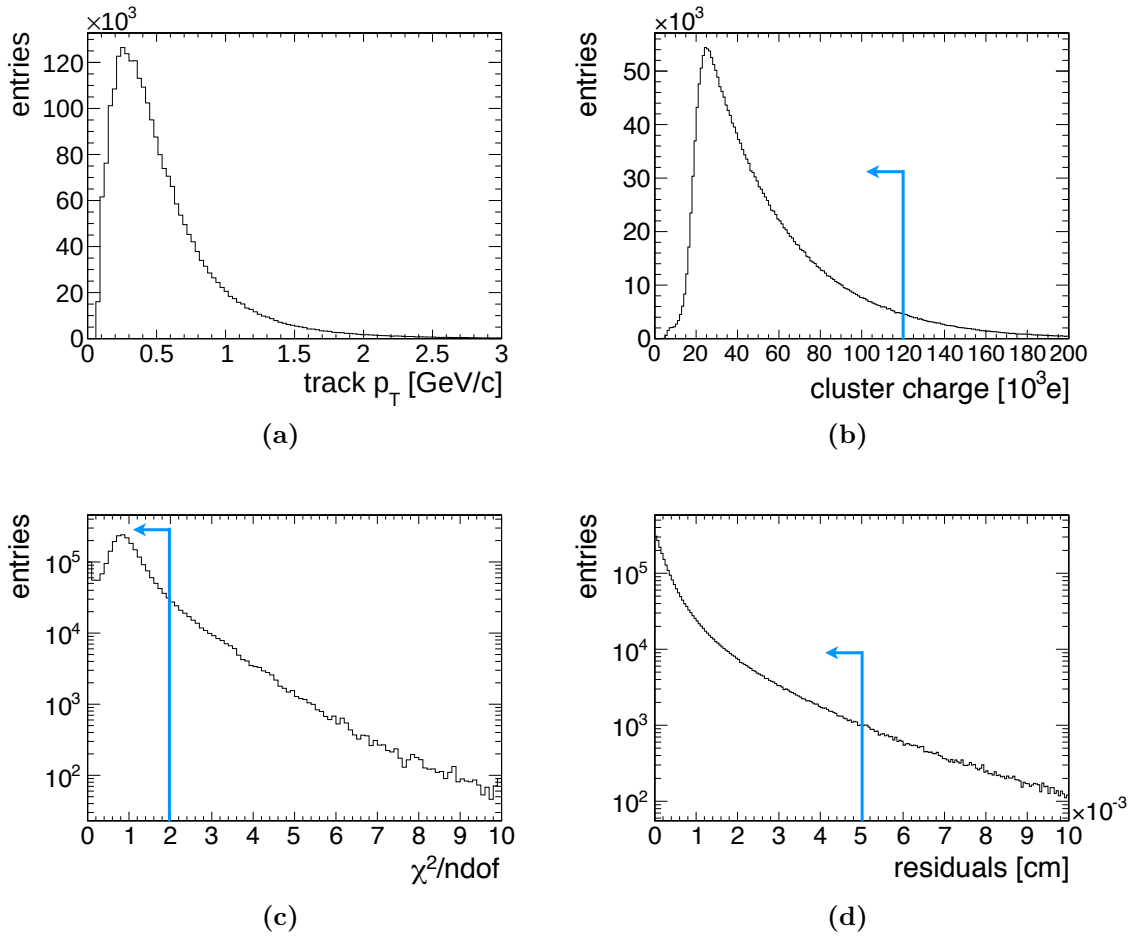

Figure 3.7: Distributions of the quantities serving for selection of tracks and clusters to be used with the grazing angle method. The distributions are obtained from minimum bias events in collision data collected at $\sqrt{s} = 0.9$ TeV and $B = 3.8$ T. (a) Transverse momentum of tracks. A minimum of 0.1 GeV/c is required. (b) Deposited electric charge in clusters. A maximum charge of 120 ke is required. (c) χ^2 per degree of freedom for fitted tracks. Tracks with χ^2/ndof<2 are selected. (d) Hit residuals defined as the difference between the extrapolated and the reconstructed hit position. Hits with residuals of maximum of 50 μm are selected.

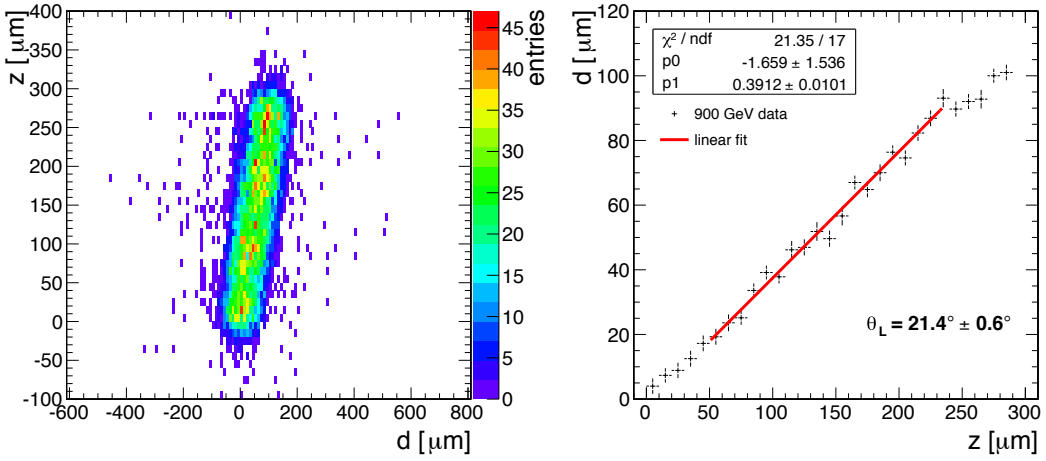

(a) **(b)**

Figure 3.8: The grazing angle method applied to selected collision data at $\sqrt{s} = 0.9$ TeV and $B = 3.8$ T. (a) Production depth z for the electrons in the silicon sensor bulk vs. their displacement d. (b) Average displacement of the electrons vs. their production depth. The tangent of the Lorentz angle $\tan\theta_L$ is given by the slope of the distribution. Solid line shows the fit applied to the data.

looping particles in the tracker. Measurements are performed with data samples collected at center-of-mass energies of 0.9 TeV and 2.36 TeV, and at magnetic fields of 3.8 T and 2 T. In addition, the technique is applied to simulated samples. The minimal cluster size method applied to the selected collision events results in the specific for this technique V-shaped distributions of cluster size vs. impact track angle (Figure 3.9). The results from all measurements using the cluster size method are summarized in Table 3.4. Excellent agreement is observed between data and simulation. However, a comparison between the results obtained with the cluster size technique and the grazing angle method (Table 3.3 and Table 3.4) indicates ∼5% systematically larger values for $\tan\theta_L$ when the cluster size method is used. This is explained with the known bias introduced by the minimal cluster size technique, as discussed in Section 3.2.

3.4 Systematic uncertainties

The method adapted to measure the Lorentz angle throughout the LHC operation is the grazing angle technique. Previous studies based on Monte Carlo simulated events have shown [84] that misalignment of the tracker and wrong Lorentz angle assumption in the hit reconstruction algorithm do not introduce a bias in the

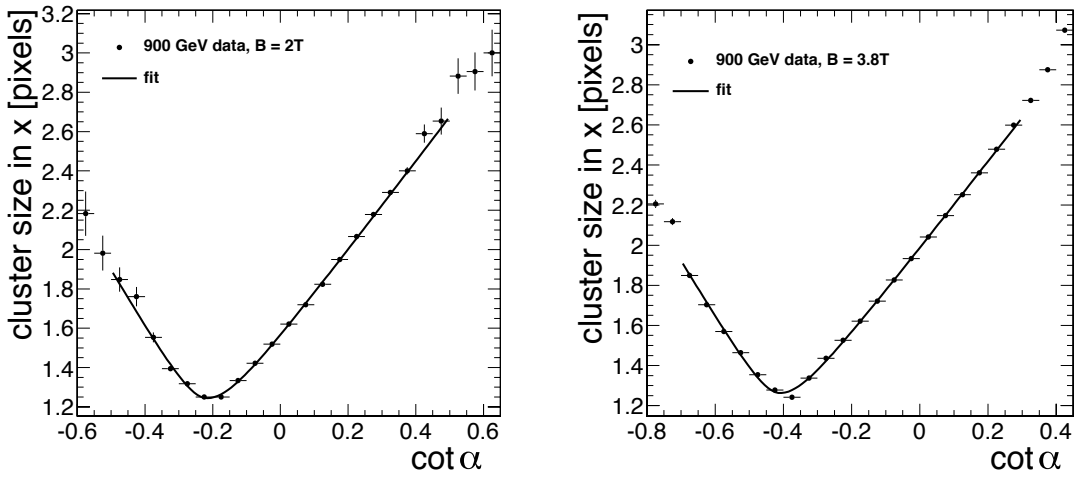

(a) **(b)**

Figure 3.9: Average cluster size in the local x direction vs. track impact angle α. Tracks are selected from minimum bias collision events at $\sqrt{s} = 0.9$ TeV. Circles correspond to data, solid line shows fit (see Eq. 3.7) to the data. (a) $B = 2$ T. (b) $B = 3.8$ T.

Collision data, grazing angle method					
events type	0.9 TeV, 3.8 T	2.36 TeV, 3.8 T	7 TeV, 3.8 T	0.9 TeV, 2 T	7 TeV, 2 T
data	0.3985 ± 0.0005	0.3980 ± 0.0008	0.3987 ± 0.0003	0.2020 ± 0.0006	0.2011 ± 0.0007
simulation	0.4006 ± 0.0005	0.4007 ± 0.0008	–	0.2110 ± 0.0007	–

Table 3.3: Summary of results for $\tan\theta_L$ measured from collision data with the grazing angle method. Where available, the measurements from data are compared with results from the PIXELAV simulation. Quoted uncertainties are statistical only.

Collision data, minimal cluster size method			
	0.9 TeV, 3.8T	2.36 TeV, 3.8T	0.9 GeV, 2T
data	0.4094 ± 0.0016	0.4211 ± 0.0064	0.2161 ± 0.0033
simulation	0.4113 ± 0.0048	0.4238 ± 0.0072	0.2098 ± 0.0025

Table 3.4: Summary of results for $\tan\theta_L$ measured from collision data with the minimal cluster size method. Where available, the measurements from data are compared with results from PIXELAV simulation. Quoted errors are statistical only.

measured Lorentz angle.

A further study on systematic uncertainties is performed with minimum bias events collected at a center-of-mass energy of 900 GeV and a magnetic field of 3.8 T. The impact of the track and cluster selection and the fit procedure are investigated. In order to estimate the uncertainties introduced by the selection criteria imposed on tracks and clusters, the magnitude of the requirements is sequentially varied for each selection quantity (transverse momentum and reduced χ^2 of tracks, cluster charge and cluster size in the y direction, hit residuals). A systematic uncertainty introduced by the fit is assessed by shifting the range within which the fit is performed. The following variations of the Lorentz angle measurement are applied (default values are given in brackets):

- Track transverse momentum larger than 0.5 GeV is required (0.1 GeV).
- The reduced χ^2 of the tracks fit is loosened to $\chi^2/\text{ndof} < 4$ ($\chi^2/\text{ndof} < 2$).
- The required maximum of the cluster charge is varied from 90 ke to 150 ke (120 ke).
- The cluster size in the y direction is required to be larger than 5 (4).
- The maximum of the hit residuals is varied from 40 μm to 60 μm (50 μm).
- The range of the fit over the sensor thickness is shifted with ± 25 μm and the fit is thus performed within the ranges 25 μm – 210 μm and 75 μm – 260 μm (50 μm – 235 μm).

The systematic uncertainties are summarized in Table 3.5. The contribution from any of the selection quantities does not exceed 1%. The largest contribution of 4.4% results from shifting the range of the fit over the sensor thickness, which is explained by the fact that at the edge areas of the pixel sensors non-linear effects start to manifest. The contributions are assumed uncorrelated and the total systematic uncertainty is calculated as the square root of the quadratic sum of all uncertainties. The estimated total systematic uncertainty of the Lorentz angle measurement with the grazing angle method adds up to 4.7%.

source of uncertainty	$\lvert\Delta \tan\theta_L\rvert$	relative error
track p_T	0.0017	0.4%
χ^2/ndof	0.0004	0.1%
cluster charge	0.0046	1.2%
cluster size in y direction	0.0044	1.1%
hit residuals	negligible	–
fit range	0.0174	4.4%
total	0.0186	4.7%

Table 3.5: Summary of systematic uncertainties of the Lorentz angle measurement with the grazing angle technique. The individual contributions are assumed uncorrelated and the total systematic uncertainty is calculated as the square root of the quadratic sum of all uncertainties.

3.5 Conclusions

Due to the presence of combined electric and magnetic fields, the charge carriers in the silicon pixel sensors of CMS experience the Lorentz force and their drift direction is deviated at the so-called Lorentz angle θ_L. The charge deflection leads to charge sharing over neighboring pixels which has an impact on the detector resolution. The Lorentz effect strongly depends on the operational conditions of the detector (such as temperature and bias voltage) and at present cannot be calculated with sufficient precision. This requires in situ measurements and monitoring of the Lorentz angle throughout the CMS operation.

The Lorentz angle in the barrel pixel detector of CMS is measured with cosmic ray data and LHC collision data. Two different measurement techniques are utilized – the *minimal cluster size method* and the *grazing angle technique*, suited for cosmic and collision data, respectively.

The magnitude of the Lorentz angle measured with cosmic muons is compared with earlier measurements with cosmic data collected at different operation conditions of the detector. Results from data and simulation are in very good agreement. Results obtained from data collected in the absence of a magnetic field are compatible with zero Lorentz drift.

Measurements of the Lorentz angle are performed with proton-proton collisions at different center-of-mass energies ($\sqrt{s}$ = 0.9 TeV, 2.36 TeV, 7 TeV) and magnetic fields (B = 2 T, 3.8 T). Results obtained at different beam energies are in excellent

agreement. The results also confirm the strong dependence on the magnetic field. A reduction of ∼50% of the Lorentz angle is observed at $B = 2$ T compared to a magnetic field of 3.8 T. Very good agreement is observed between results from data and simulation.

The Lorentz angle measured from collision data at the nominal magnetic field of 3.8 T, a bias voltage of 150 V and a temperature of 10 °C, is 21.7°. Systematic uncertainties are studied with minimum bias collision events and the total systematic uncertainty is estimated to be about 5%.

Chapter 4

Reconstruction and selection of the decay $\Lambda_b \to J/\psi(\mu^+\mu^-)\Lambda(p\pi^-)$

The goal of the analysis presented in this dissertation is to measure the polarization of the Λ_b baryon. This Chapter describes the reconstruction and selection of the decay $\Lambda_b \to J/\psi(\mu^+\mu^-)\Lambda(p\pi^-)$. The data and simulation samples are discussed in Section 4.1. The online trigger selection and the offline reconstruction and selection steps are described in Section 4.2 and Section 4.3, respectively. Reconstructed signal in data is compared with simulations in Section 4.4. Properties of signal candidates in data reconstructed at different *pp* interaction multiplicities are discussed in Section 4.5.

The reconstructed and selected sample of Λ_b decay candidates is further used to perform an angular analysis of the decay, presented in Chapter 5.

4.1 Data and simulation samples

4.1.1 Data samples

The analysis presented in this dissertation uses proton-proton collision data at a center-of-mass energy $\sqrt{s} = 7$ TeV that were collected by the CMS experiment in 2011. The data corresponds to an integrated luminosity $\mathcal{L} = 5.1$ fb^{-1}. The event sample is collected with the requirement for two reconstructed muons at the HLT trigger level, imposing specific requirements on the properties of the muons which are discussed in Section 4.2.

4.1.2 Simulation samples of signal events

Proton-proton collisions at $\sqrt{s} = 7$ TeV are simulated with the PYTHIA (version 6.4) generator [90]. It incorporates the production of $b\bar{b}$ pairs through $q\bar{q}$ annihilation, gluon-gluon fusion, flavor excitation and gluon splitting. The fraction of events containing a $b\bar{b}$ pair amounts to $\sim$1% of the total number of generated inclusive QCD events, and less than 10% of the generated b-quarks hadronize to Λ_b. Once a Λ_b is produced by PYTHIA, the simulation is further handled by the EvtGen generator [91] which forces the Λ_b decay to the final state particles of interest, namely $\Lambda_b \to J/\psi\,\Lambda$ with $J/\psi \to \mu^+\mu^-$ and $\Lambda \to p\pi$.

4.1.3 Simulation of polarized Λ_b

An additional reason to use the EvtGen generator for the decay of Λ_b is that PYTHIA does not include polarization information. EvtGen allows proper simulation of spin correlations through the implementation of spinor algebra and decay amplitudes. Generation of decays of polarized Λ_b particles has been implemented within the EvtGen framework by the ATLAS Collaboration [92] and the same approach has been adopted in the CMS software framework. The polarization of Λ_b is set through the spin density matrix formalism of EvtGen. For particles with spin 1/2, such as Λ_b, the spin density matrix ρ is defined as

$$\rho = \frac{1}{2}(I + \vec{P} \cdot \vec{\sigma}), \tag{4.1}$$

where I is the identity matrix, $\vec{P}$ is the polarization vector and $\vec{\sigma}$ is the Pauli vector whose components are the Pauli matrices $(\sigma_1, \sigma_2, \sigma_3)$. The polarization vector of Λ_b is defined as

$$\vec{P} = P\left(\frac{\hat{z} \times \vec{p}_{lab}(\Lambda_b)}{|\hat{z} \times \vec{p}_{lab}(\Lambda_b)|}\right), \tag{4.2}$$

where P is the magnitude of the polarization, $\vec{p}_{lab}$ is the momentum of Λ_b in the laboratory frame, and $\hat{z}$ is a unit vector along the z-axis in the laboratory frame of CMS. To generate the angular distributions of the daughter particles in the decays $\Lambda_b \to J/\psi\,\Lambda$ and $\Lambda \to p\pi$, the HELAMP model of EvtGen is used. By taking as input the helicity amplitudes of the involved decays, this model simulates generic two-body decays with given spin configurations. For the simulation of the decay $J/\psi \to \mu^+\mu^-$, the EvtGen VLL model is used which describes the decay of a vector particle to two leptons. Details about the HELAMP and VLL models implemented in the EvtGen generator can be found in Ref. [93].

The generated particles are propagated through a model of the CMS detector material. Interactions of particles with material as well as detector response are simulated with the GEANT4 package [94]. The output is raw digitized detector response which is further fully reconstructed in an identical way as data.

4.2 Trigger selection

The first level of selection of events containing $\Lambda_b \to J/\psi(\mu^+\mu^-)\Lambda(p\pi^-)$ decays is provided by the HLT system of CMS. In order to select the highest number of signal-like events, triggers requiring the presence of two muons in the event are used. The implemented dimuon triggers in 2011 can be generally categorized in two groups:

- *"Barrel triggers"*: Aimed at muons originating from primary vertices (*prompt muons*) and from displaced vertices of long-lived particles. These muon triggers are suited for measurements of particle lifetimes since the whole range of particle decay lengths, starting from zero, is accessible to observe. This comes at the price of accepting only muons in the barrel part of the tracker having pseudorapidity $|\eta| < 1.2$.

- *"Displaced vertex triggers"*: Muons are accepted within a large geometrical coverage of $|\eta| < 2.2$ but are required to originate from vertices displaced from the beam spot. These muon triggers are not optimal for particle lifetime measurements due to a bias introduced in the measured decay length of the particles.

The presented in this thesis angular analysis of the Λ_b decay exploits the *"displaced vertex triggers"*. The choice is motivated by the following reasonings:

- Λ_b is a long lived particle and the two muons originate from a secondary vertex displaced from the beam spot.

- Particle lifetimes are not studied in this analysis and a possible lifetime bias does not affect the angular distributions of the decay products.

- Most importantly, the larger geometrical coverage provided by the displaced vertex triggers yields more signal events.

The displaced dimuon triggers impose requirements on the two muons such as dimuon invariant mass close to the mass of the J/ψ meson, transverse momentum of the muons and displacement of the dimuon vertex w.r.t. the beam spot. Throughout the LHC operation in 2011 the trigger thresholds were gradually increased and additional requirements were introduced in the trigger definitions in

order to control the recorded event rate. The peak LHC parameters in 2011 listed in Table 2.1 result in the following criteria imposed by the dimuon displaced vertex triggers:

- The invariant mass of the two muons $m(\mu\mu)$ is in the range [2.9, 3.3] GeV/c^2.
- The χ^2 probability of a Kalman vertex fit to the two muons is at least 15%.
- The transverse momentum $p_T(\mu)$ of each muon is greater than 4 GeV/c.
- The pseudorapidity $\eta(\mu)$ of each muon is within $|\eta|< 2.2$.
- The dimuon vertex is displaced w.r.t. the beam spot with a significance of $L_{xy}/\sigma > 3$, where L_{xy} is the distance between the beam spot and the vertex in the x-y plane, and σ is the error on the distance.
- The pointing angle θ between the reconstructed momentum vector of the dimuon system and the vector from the beam spot position to the dimuon vertex fulfills the requirement $\cos\theta > 0.9$. This is in fact a requirement on the hypothetical reconstructed J/ψ meson to point toward the beam spot.
- The distance of closest approach between the two muons is less than 0.5 cm.

4.3 Offline selection

4.3.1 J/ψ selection

Candidates of J/ψ mesons are formed from pairs of oppositely charged muons originating from a common vertex. The muons are required to be reconstructed as *tracker muons* (see Section 2.3.3). Reconstructed *global muons* are accepted if they also pass the *tracker muons* selection. In order to be consistent with the trigger selection, the same requirements as the ones implemented in the dimuon trigger definitions (Section 4.2) are explicitly applied to the muons in the offline selection. The selection criteria is further optimized to reduce background events without losing signal J/ψ candidates. This is achieved with a requirement of $\cos\theta > 0.95$ (instead of $\cos\theta > 0.90$ implemented by the trigger) and by introducing a requirement on the transverse momentum of the dimuon system, namely $p_T(\mu^+\mu^-) > 8$ GeV/c. The invariant mass distribution $m(\mu^+\mu^-)$ of two muons following the selection is shown in Figure 4.1. The signal is modeled by a double Gaussian function with a common mean defined in the following way:

$$G(x;\mu,\sigma_1,\sigma_2,f) = f \cdot G_1(x;\mu,\sigma_1) + (1-f)\cdot G_2(x;\mu,\sigma_2), \tag{4.3}$$

where G_1 and G_2 are two Gaussian functions of the variable x (in this case $x \equiv m(\mu^+\mu^-)$), sharing the same mean value μ and having a standard deviation σ_1 and σ_2, respectively. The parameter $f \in [0,1]$ denotes the fraction of G_1. The

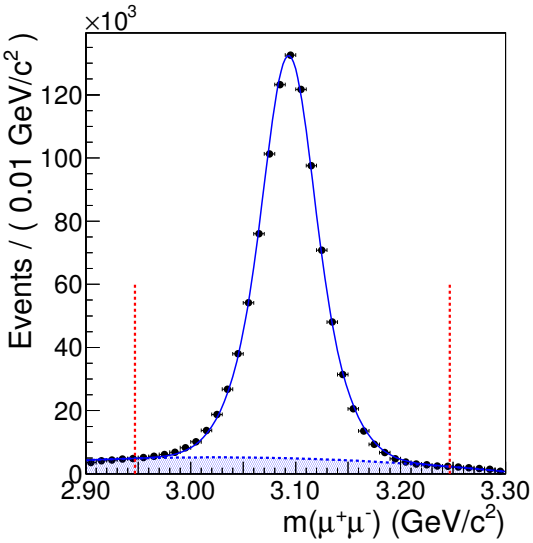

Figure 4.1: Invariant mass distribution of two oppositely charged muons in data following J/ψ selection requirements. Points denote data, the solid line is the fit to the data. A double Gaussian function is used to describe the peak and a second order polynomial is used to model the combinatorial background (dashed blue line). The vertical lines mark the mass range of the selected J/ψ candidates to be used further in the analysis.

background distribution is modeled by a second order polynomial function. The fit to the dimuon invariant mass distribution yields a mean value $\mu = 3093.37 \pm 0.04$ MeV/c^2 where the uncertainty is statistical only. The vertical lines in Figure 4.1 mark the range in which J/ψ candidates are selected, corresponding to masses of $m_{PDG}(J/\psi) \pm 150$ MeV/c^2 around the world average J/ψ mass $m_{PDG}(J/\psi) = 3096.916 \pm 0.011$ MeV/c^2 [16].

4.3.2 Λ selection

The next step in the reconstruction of Λ_b particles is the search for Λ candidates in the events where successful J/ψ candidates have been selected. The reconstruction of V0 particle decays $\Lambda \to p\pi^-$ (and its charge conjugate) and $K_S \to \pi^+\pi^-$ at CMS has been extensively studied [95, 96]. Candidates of Λ and K_S are created from pairs of oppositely charged non-muon tracks requiring a successful Kalman vertex fit applied to the tracks. The CMS detector does not have a particle identification system to distinguish between pions and protons. This requires mass hypothesis to be used and tracks are assigned pion or proton masses, respectively. For the reconstruction of Λ candidates, the lower momentum track is assumed to be the

pion. Since both the mother particle Λ_b in the decay and the daughter particle Λ are long-lived with $c\tau = 427$ μm and 7.89 cm [16], respectively, the decay vertex of the Λ candidate is required to be displaced w.r.t. the beam spot. The selection of Λ and K_s^0 particles detailed in Ref. [95] has been adopted as the standard selection criteria for V0 particles at CMS. It includes requirements on the quality of the two tracks and their vertex. The requirements from Ref. [95] are further optimized in this analysis in order to reduce the combinatorial background. Λ candidates are subject to the following criteria:

- Proton (pion) mass is assigned to the track with the higher (lower) momentum.
- Track requirements:
  Tracks are required to have at least 6 hits in the tracker and reduced χ^2 per degree of freedom less than 5. The transverse impact parameter of the tracks with respect to the beam spot is required to be greater than 2σ, where σ is the calculated uncertainty accounting for beam spot and track uncertainties. In addition, there are requirements for a minimum transverse momentum for the pion (0.3 GeV/c) and proton (1 GeV/c) track and the reconstructed Λ candidate (1.3 GeV/c).
- Vertex requirements:
  The two tracks are fit with a Kalman vertex fitter and the χ^2 probability is required to be greater than 2%. The transverse separation of the vertex from the beam spot is required to be greater than 15σ where σ accounts for the beam spot and vertex position uncertainties.

In order to investigate the contamination from the decay $K_S \to \pi^+\pi^-$, the invariant mass of the track pairs which pass the listed selection is as well reconstructed with the assumption of two pion tracks instead of a pion and a proton. Figure 4.2a shows the invariant mass distribution resulting from a $(\pi^+\pi^-)$ hypothesis, and a clear peak can be seen around the known mass of K_S, $m(K_S) \approx 0.498$ GeV/c^2 [16]. The events contained in the peak populate as well the invariant mass distribution formed under the hypothesis of $(p\pi)$. To reject possible contamination from the decay $K_S \to \pi^+\pi^-$, track pairs entering the peak in the distribution of $m(\pi^+\pi^-)$ are discarded. The vertical lines in Figure 4.2a mark the rejected peak range. A fit to the distribution of $m(\pi^+\pi^-)$, using a double Gaussian function for the peak and a polynomial for the background, shows that more than 99% of the K_S candidates peak is contained within the rejected area. The veto on the K_S mass leads to a reduction of $\sim$20% in the number of $(p\pi)$ pairs. The final invariant mass distribution $m(p\pi)$ is shown in Figure 4.2b. A fit is applied to the data with a double Gaussian function modeling the signal and a second order polynomial function describing

the background. The obtained by the fit mean value for the signal peak is $\mu = 1115.88 \pm 0.02$ MeV/c^2 where the uncertainty is statistical only. Candidates of Λ particles are selected within the mass range $m_{PDG}(\Lambda) \pm 9$ MeV/c^2 (indicated by the vertical lines in Figure 4.2b) around the world average mass of Λ, $m_{PDG}(\Lambda) = 1115.683 \pm 0.006$ MeV/c^2 [16].

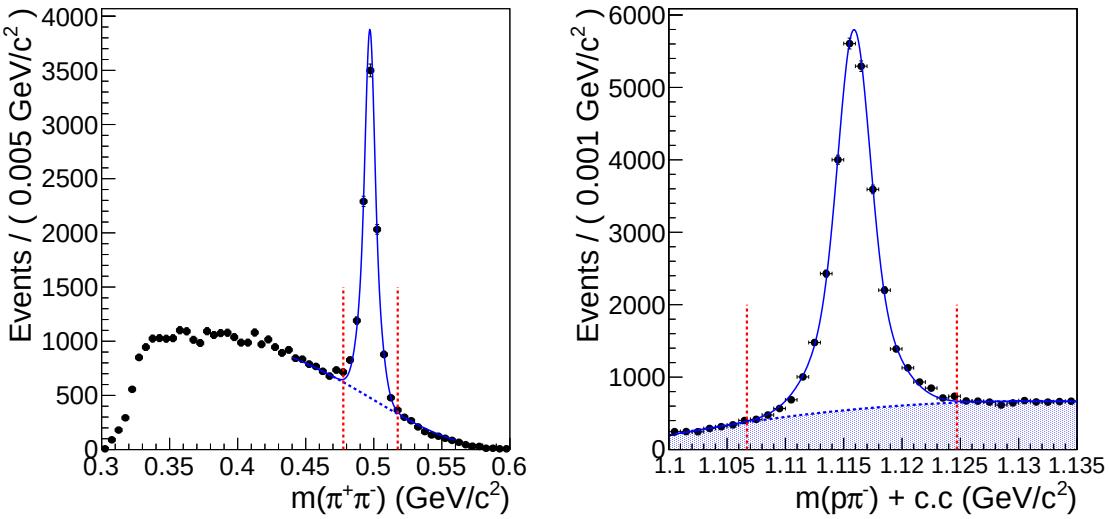

(a) **(b)**

Figure 4.2: Invariant mass distributions of two charged tracks in data reconstructed with (a) $(\pi^+\pi^-)$ hypothesis, (b) $(p\pi)$ hypothesis after rejecting K_S contamination. Solid lines indicate fit to the data. Double Gaussian functions are used to describe the peaks, polynomials are used to model the background (dashed blue line). The vertical lines in (a) mark the rejected peak range. The vertical lines in (b) indicate the mass range within which Λ candidates are selected for the further steps of the analysis.

4.3.3 Kinematic vertex fit and Λ_b selection

Λ_b candidates are constructed by combining in pairs the successfully selected J/ψ and Λ candidates and applying a sequential two-step constrained kinematic fit (see Section 2.3.5). First, a kinematic fit is applied to the pion and proton tracks constraining the invariant mass of the pair to the world average mass of Λ. A second fit is then performed to the two muon tracks and the neutral Λ candidate created by the first fit. The muon tracks and the backwards extrapolated trajectory of the Λ are constrained to have a common vertex and the invariant mass of the muons is constrained to the world average J/ψ mass. The imposed mass constraints are

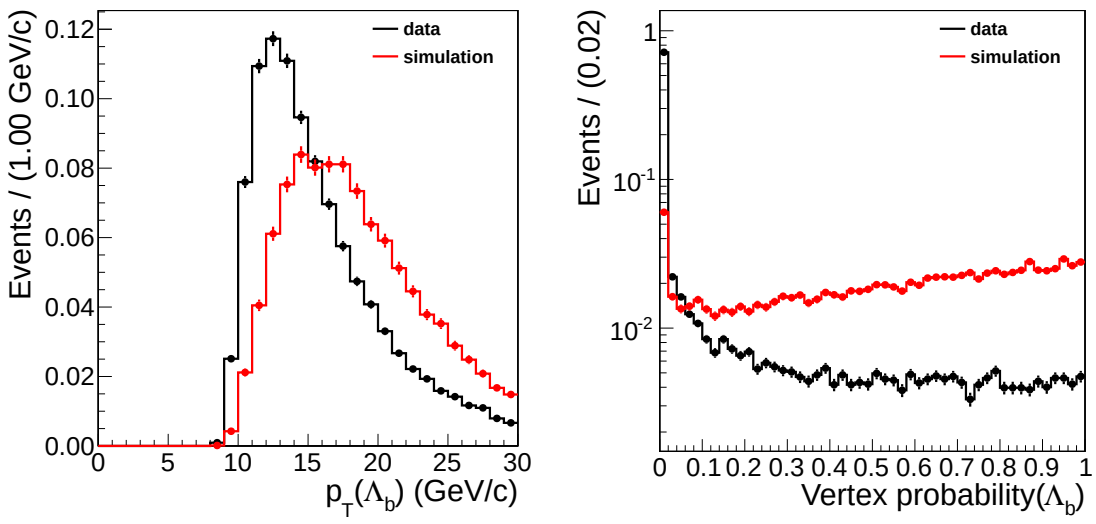

(a) **(b)**

Figure 4.3: (a) Transverse momentum distributions reconstructed from $(J/\psi\,\Lambda)$ candidates upon a successful kinematic fit in data (black) and in simulated signal samples (red). Candidates with a transverse momentum of less than 10 GeV/c are discarded. (b) χ^2 probability returned by the constrained kinematic vertex fit for data (black) and for simulated signal samples (red). Candidates with a probability of less than 3% are rejected. Both histograms are normalized to a unit area.

applicable due to the fact that for both J/ψ and Λ the experimental mass resolution is much higher than the natural width of the resonances. The width of J/ψ is $\Gamma_{J/\psi} = 93$ keV/c^2 while its reconstructed full width at half maximum is ∼70 MeV/c^2. For the long-lived particle Λ with a mean lifetime $\tau_\Lambda \approx 2.6 \times 10^{-10}$ s, the experimental resolution of ∼4 MeV/c^2 (FWHM) is far beyond its natural width $\Gamma_\Lambda = \hbar/\tau_\Lambda$.

Upon a successful kinematic fit, a final selection of Λ_b candidates is applied aiming to reject background events while keeping most of the signal. Figure 4.3a shows the distribution of the transverse momentum p_T for all $(J/\psi\,\Lambda)$ candidates successfully passing the kinematic fit in data and in simulated signal samples. The distribution of the simulated signal peaks at higher momenta w.r.t. data implying that the low momentum range is more contaminated with background events. However, it can be seen from the plot that by imposing a tight requirement on the transverse momentum (e.g. $p_T(\Lambda_b) > 15$ GeV/c), a significant fraction of the signal can be easily cut away. Therefore, a rather loose requirement of $p_T(\Lambda_b) > 10$ GeV/c is applied. Another quantity used to discriminate signal from background is the χ^2 vertex probability returned by the kinematic fit. A comparison of the probability

distributions observed in data and in simulated signal samples is shown in Figure 4.3b. In the data distribution, a large fraction of the particle candidates yield a fit probability close to zero (note the logarithmic scale) while the distribution of the simulated signal is more uniform. This suggests that the candidates with a fit probability close to zero are predominantly background. A requirement on the fit probability $P(\chi^2) > 3\%$ is applied as a final selection criterium for Λ_b candidates. Besides the high track multiplicity in data, reaching $\sim O(10^2)$ tracks in a pp collision, at most one Λ_b candidate per bunch crossing is found to fulfill all selection requirements.

The invariant mass distribution $m(J/\psi\,\Lambda)$ reconstructed from J/ψ and Λ candidates following the entire selection procedure described above can be seen in Figure 4.4. The distribution is separately shown for the whole sample including particle (Λ_b) and antiparticle ($\overline{\Lambda}_b$) candidates (Figure 4.4a), particle candidates only (Figure 4.4b) and antiparticle candidates only (Figure 4.4c). To extract the number of signal (N_{sig}) and background (N_{bkg}) events, an extended unbinned likelihood fit is applied to the data using the RooFit software framework [97]. The signal is modeled by a double Gaussian function with a common mean as defined in Eq. 4.3, where the variable x corresponds to the $(J/\psi\,\Lambda)$ invariant mass m. The background is described by a linear function of the form

$$P(m;p) = 1 + p \cdot m, \tag{4.4}$$

where p denotes the slope. A summary of the fit output obtained in the mass range $m(J/\psi\,\Lambda) \in [5.40, 5.84]$ GeV/c^2 is given in Table 4.1. As can be seen in the distributions in Figure 4.4, these boundaries contain the signal peak region and large sidebands around the peak. Fit results are provided for the entire sample of particles and antiparticles $(J/\psi\,\Lambda) \cup (J/\psi\,\overline{\Lambda})$, and separately for $(J/\psi\,\Lambda)$ and $(J/\psi\,\overline{\Lambda})$. To obtain a better notion of the event composition in the signal peak region, the fit function with parameters fixed according to the values in Table 4.1, is integrated in the peak range $m(J/\psi\,\Lambda) \in [\mu - 0.05, \mu + 0.05]$ GeV/c^2. Within these boundaries, there are 911 ± 38 Λ_b candidates and 845 ± 37 $\overline{\Lambda}_b$ candidates with a signal to background ratio $S/B \approx 3.2$ and 3.7, respectively. A summary of the event composition in the invariant mass peak is given in Table 4.2.

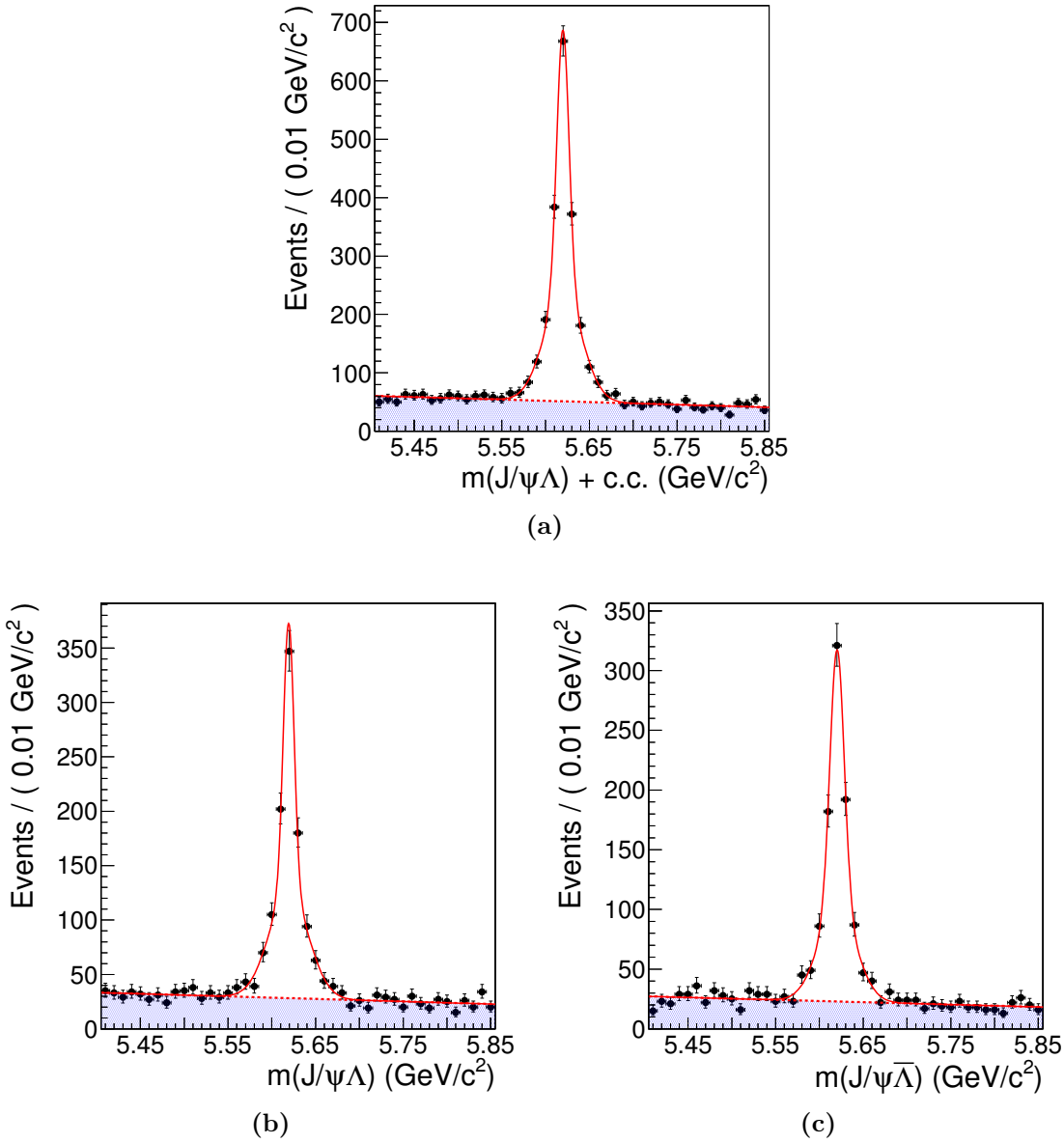

Figure 4.4: Invariant mass distributions reconstructed from $(J/\psi\,\Lambda)$ candidates in data following all selection requirements. (a) Entire sample, $(J/\psi\,\Lambda)$ and $(J/\psi\,\overline{\Lambda})$. (b) $(J/\psi\,\Lambda)$, 925 ± 39 Λ_b candidates found. (c) $(J/\psi\,\overline{\Lambda})$, 853 ± 37 $\overline{\Lambda}_b$ candidates found.

$m(J/\psi\,\Lambda) \in [5.40, 5.84]$ GeV/c^2			
	full sample	particle candidates	antiparticle candidates
μ (GeV/c^2)	5.6198 ± 0.0004	5.6192 ± 0.0005	5.6202 ± 0.0005
σ_1 (GeV/c^2)	0.0070 ± 0.0009	0.0062 ± 0.0009	0.0081 ± 0.0015
σ_2 (GeV/c^2)	0.0216 ± 0.0023	0.0224 ± 0.0025	0.0215 ± 0.0043
N_{sig}	1776 ± 54	925 ± 39	853 ± 37
N_{bkg}	2282 ± 58	1259 ± 43	1023 ± 39
p	-0.1471 ± 0.0047	-0.1466 ± 0.0066	-0.1476 ± 0.0069
f	0.45 ± 0.08	0.41 ± 0.07	0.52 ± 0.02

Table 4.1: Results from an extended likelihood fit to the invariant mass distribution $m(J/\psi\,\Lambda)$ in data. The range of the fit is $[5.40, 5.84]$ GeV/c^2 corresponding to the entire displayed range in Figure 4.4.

$m(J/\psi\,\Lambda) \in [\mu - 0.05, \mu + 0.05]$ GeV/c^2			
	full sample	Λ_b candidates	$\overline{\Lambda}_b$ candidates
N_{sig}	1756 ± 53	911 ± 38	845 ± 37
N_{bkg}	512 ± 31	282 ± 25	229 ± 23

Table 4.2: Number of signal and background events in the $(J/\psi\,\Lambda)$ invariant mass peak in data. Results are obtained from an extended likelihood fit. The fit function, with all parameters except N_{sig} and N_{bkg} fixed to the values in Table 4.1, is integrated in the peak mass range $[\mu - 0.05, \mu + 0.05]$ GeV/c^2. These boundaries contain ∼99% of the signal.

4.4 Comparison of data and simulation

Simulated signal events of the decay $\Lambda_b \to J/\psi(\mu^+\mu^-)\Lambda(p\pi^-)$ are to be used to assess efficiency effects introduced by detector geometry and event selection. In order for the efficiency estimation to be reliable, the simulation should reasonably well describe the data. This section presents a comparison of the main kinematic distributions of the involved particles obtained in data and in simulation.

In data, the distributions formed by events contained in the mass peak of Λ_b are contaminated with a certain amount of background, as can be seen in Table 4.2. The background distributions are determined from events populating the mass peak sidebands. They are scaled to the expected number of background events in the peak region and are then subtracted from the distributions obtained from the peak. Assuming that the sideband-subtracted data represent uncontaminated signal, they are compared with the simulated signal.

The transverse momentum distributions for Λ_b and $\overline{\Lambda}_b$ are shown in Figure 4.5a and Figure 4.5c, respectively. The plots indicate a deficit towards the lower p_T values in the simulated samples w.r.t. data. To correct for this, the simulated signal events are re-weighted to match the transverse momentum distribution of Λ_b in data. A comparison of pseudorapidity distributions in data and simulation for Λ_b and $\overline{\Lambda}_b$ is given in Figure 4.5b and Figure 4.5d, respectively. A discrepancy of up to 3% per bin is observed which is present also after the re-weighting of the simulated events.

A comparison between data and simulation for all decay products of Λ_b (J/ψ, Λ, μ^+, μ^-, p, π) can be found in Appendix A. Good compatibility is observed and the re-weighted on $p_T(\Lambda_b)$ simulated samples generally show better agreement. However, discrepancies in the kinematic distributions of the daughter particles might be an artifact of a potential polarization of the mother Λ_b particle in data. Therefore, re-weighting of the simulated samples so that to match the properties of the daughter particles in data is not performed.

4.5 Comparison of data with different number of pile-up events

Throughout the data collection period in 2011, the performance of LHC was steadily improving with the aim to raise the instantaneous luminosity of the machine. Along with this, the average number of pp collisions in a bunch crossing was increasing as well. The selected ($J/\psi\,\Lambda$) candidates shown in Figure 4.4a originate from bunch crossings with a number of reconstructed interactions varying from 1 up to 30. This can be seen in Figure 4.6 which shows the distribution of the number of recon-

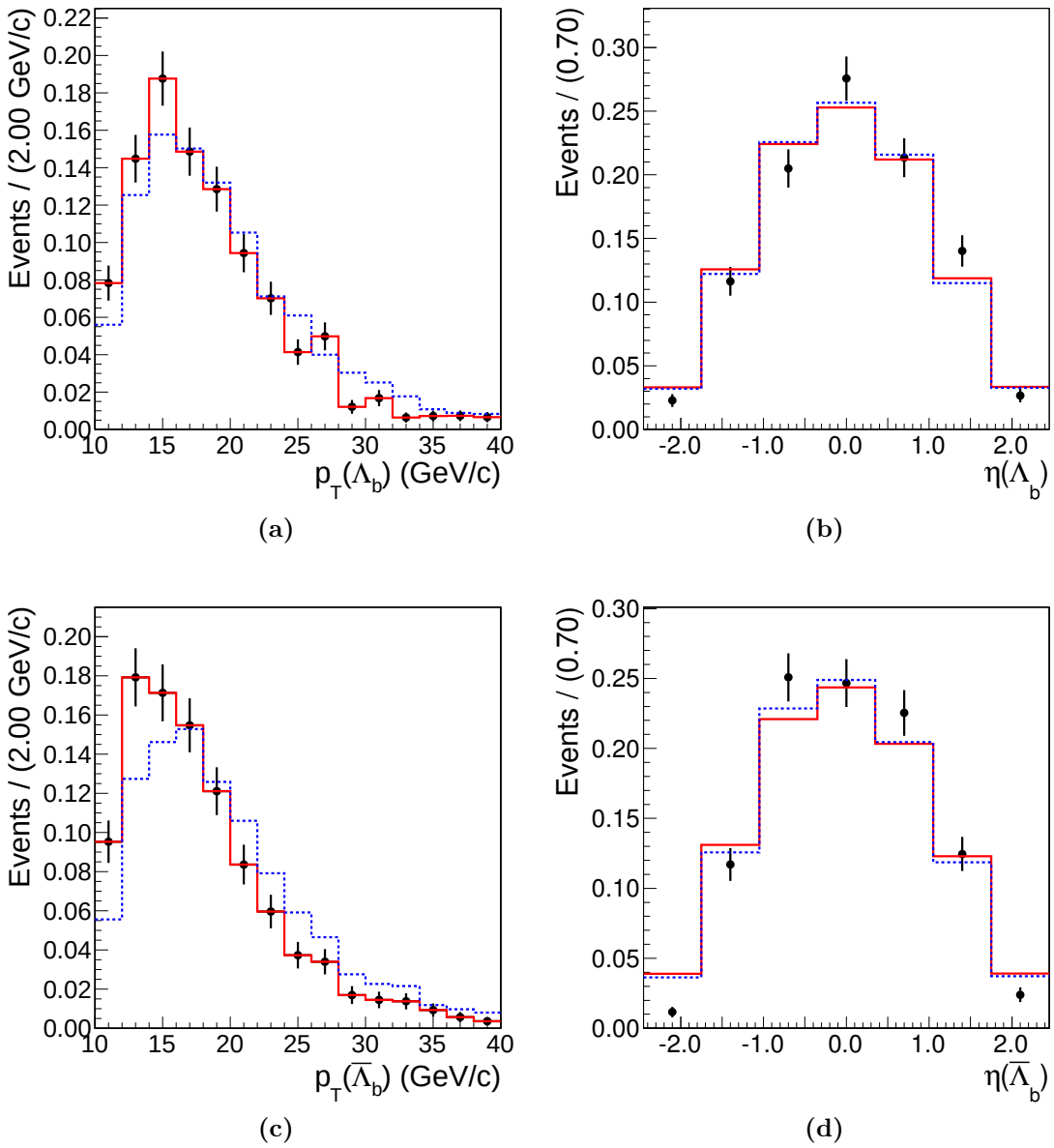

Figure 4.5: Comparison of sideband-subtracted data (black) and simulated signal. Dashed blue (Solid red) lines represent distributions in simulated samples before (after) the simulated events are re-weighted to match the $p_T(\Lambda_b)$ distribution in data. All histograms are normalized to a unit area. (a) and (b) show transverse momentum and pseudorapidity distributions of Λ_b. (c) and (d) show transverse momentum and pseudorapidity distributions of $\overline{\Lambda}_b$.

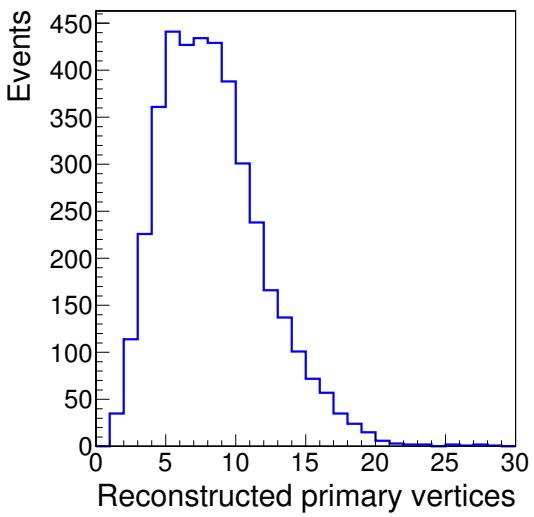

Figure 4.6: Number of reconstructed primary vertices per bunch crossing for events with $(J/\psi\,\Lambda)$ candidates in the mass range $m(J/\psi\,\Lambda) \in [5.40, 5.84]$ GeV/c^2 (see Figure 4.4a).

structed primary vertices for the events that enter the plot in Figure 4.4a. It is important to assure that the measured properties of the selected Λ_b candidates do not depend on the multiplicity of the pp interactions. Foremostly, the observed angular distributions of interest for the polarization measurement of the Λ_b baryon must be consistent in low and high pile-up environment. The limited data statistics allows to split the whole sample of selected candidates into two parts having nearly the same number of events with up to 7 and more than 7 reconstructed primary vertices in a bunch crossing. The distributions of the Λ_b candidates mass and the three angles of interest for the polarization measurement ($\cos\theta_\Lambda$, $\cos\theta_p$ and $\cos\theta_\mu$, see Figure 1.6) are given in Figure 4.7. The displayed data are contained in the mass peak of Λ_b and the background has been subtracted. The distributions obtained in low and high pile-up environment show good consistency within one statistical standard deviation. This gives confidence that Λ_b candidates originating from events with different pile-up multiplicities can be mixed and used in a single sample. This observation is essential also due to the fact that the available simulated signal samples do not include pile-up events.

Comparisons of more kinematic distributions derived from low and high pile-up environment can be seen in Appendix B. These include transverse momentum and pseudorapidity distributions for Λ_b candidates and their decay products. Good consistency is observed for all of them.

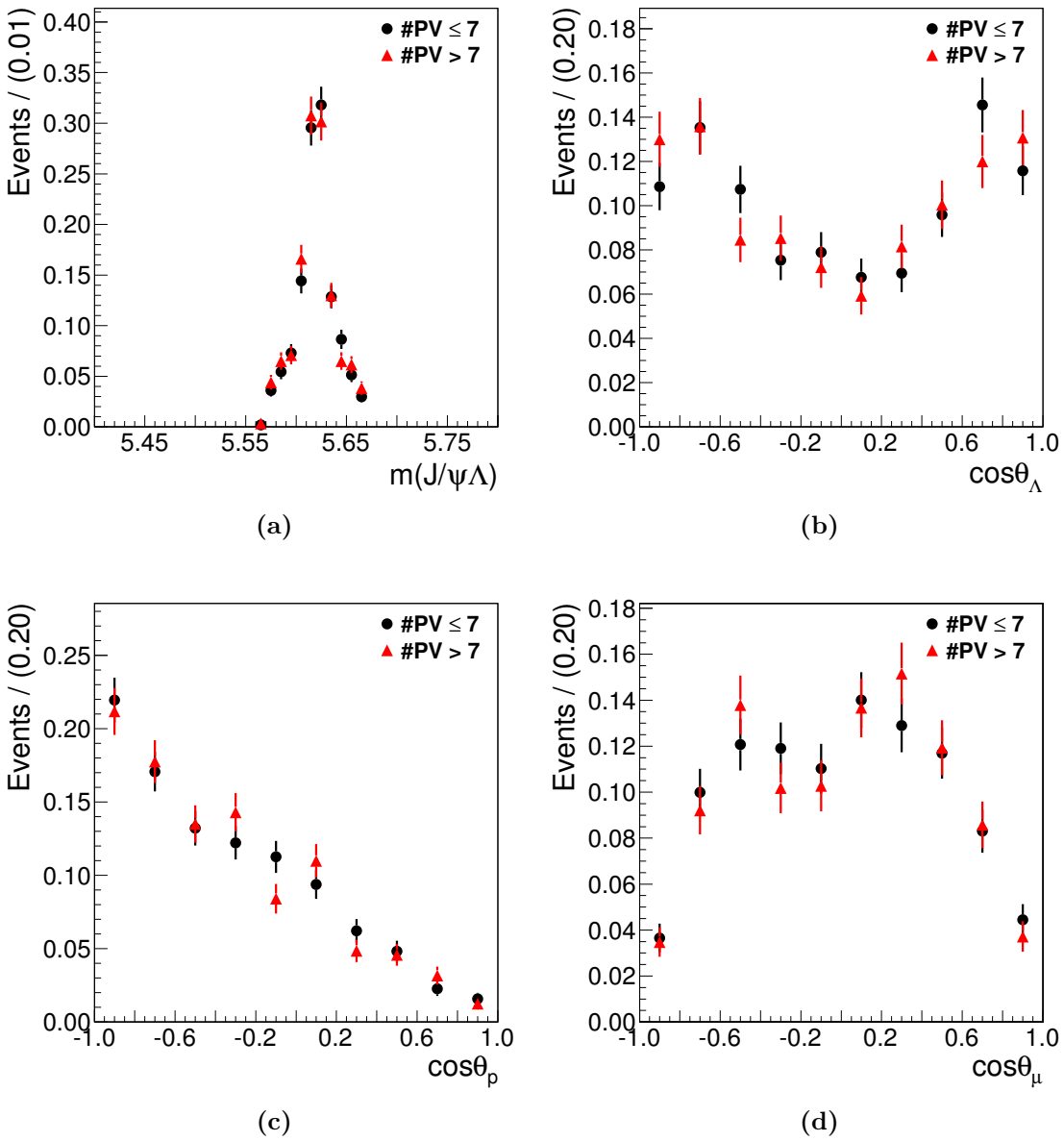

Figure 4.7: Mass and angular distributions for Λ_b (+ c.c.) candidates in events with up to 7 (black circles) and more than 7 (red triangles) reconstructed primary vertices. The events are contained in the mass peak of Λ_b and the background is subtracted. (a) Mass of Λ_b candidates. (b) $\cos\theta_\Lambda$ for Λ in the rest frame of Λ_b. (c) $\cos\theta_p$ for the proton in the rest frame of Λ. (d) $\cos\theta_\mu$ for the muon in the rest frame of J/ψ. All histograms are normalized to a unit area.

4.6 Conclusions

The decay $\Lambda_b \to J/\psi\,\Lambda$ with $J/\psi \to \mu^+\mu^-$ and $\Lambda \to p\pi$ is reconstructed in proton-proton collision data collected in 2011 at a center of mass energy $\sqrt{s} = 7$ TeV and corresponding to an integrated luminosity $\mathcal{L} = 5.1$ fb^{-1}. The number of selected Λ_b ($\overline{\Lambda}_b$) candidates is 911 ± 38 (845 ± 37) with a signal to background ratio of 3.2 (3.7) and a mean mass of 5619.8 ± 0.4 MeV/c^2. Consistency between signal in data and simulation is observed, which can be improved by re-weighting the simulation to match the data. The reconstructed quantities of greatest importance for the polarization measurement of Λ_b, the three angular distributions $\cos\theta_\Lambda$, $\cos\theta_p$ and $\cos\theta_\mu$ (see their definitions in Figure 1.6), are observed to be independent on the multiplicity of the reconstructed proton-proton interactions in the events.

Chapter 5

Measurement of the Λ_b polarization

The sample of Λ_b candidates reconstructed and selected in the decay $\Lambda_b \to J/\psi(\mu^+\mu^-)\Lambda(p\pi^-)$, as described in Chapter 4, is used to measure the polarization of the Λ_b baryon. The analysis exploits the angular correlations between the daughter particles in the decay and the polarization is extracted by a multi-dimensional likelihood fit to the relevant angular distributions.

Correlation factors and resolution of the angles describing the decay are discussed in Section 5.1 and Section 5.2. The likelihood function used to extract the Λ_b polarization is described in Section 5.3 and its signal and background components are presented in Sections 5.4–5.6. Performed validation tests of the fit are discussed in Section 5.7. The application of the fit to data and the results of the analysis are presented in Section 5.8 and Section 5.9, followed by a discussion of the systematic uncertainties in Section 5.10.

5.1 Correlation factors

As was shown in Chapter 1, the full angular distribution describing the decay $\Lambda_b \to J/\psi(\mu^+\mu^-)\Lambda(p\pi^-)$ involves three polar angles (θ_Λ, θ_p, θ_μ) and two azimuthal angles (φ_p, φ_μ) (see Eq. 1.23). To extract the polarization of Λ_b from the angular correlations of the daughter particles, at least the three polar angles have to be observed (Eq. 1.31). Considering the high complexity of the full 5-dimensional angular distribution involving 7 unknown parameters, and the limited number of available signal events (see Table 4.2), the presented analysis makes use of the simplified 3-dimensional form of the distribution. This approach, however, assumes a uniform detector acceptance over φ_p and φ_μ and does not take into account possible correlations involving the azimuthal angles. Such correlations could arise due to

the geometrical acceptance and efficiency of the detector and might require explicit correlation coefficients to be included in Eq. 1.31.

The level of correlation between two variables x and y is estimated by the correlation factor ρ_{xy} defined as

$$\rho_{xy} = \frac{\mathrm{Cov}(x, y)}{\sigma_x \, \sigma_y}, \tag{5.1}$$

where $\mathrm{Cov}(x, y)$ is the covariance of x and y, and σ_x and σ_y is the standard deviation of x and y, respectively. Thus defined, ρ_{xy} lies in the range $[-1, 1]$ [98]. The correlation factors between all five angular distributions as observed in data are listed in Table 5.1. No correlations of more than 4% involving the azimuthal angles are observed neither for Λ_b nor for $\overline{\Lambda}_b$ candidates. Based on these observations, correlation coefficients are not introduced in Eq. 1.31. However, effects from discarding the azimuthal angles φ_p and φ_μ are taken into account in the systematic uncertainties discussed in Section 5.10.

	Λ_b candidates	$\overline{\Lambda}_b$ candidates
variables	correlation factors	correlation factors
$\cos\theta_\Lambda - \cos\theta_p$	0.062	-0.051
$\cos\theta_\Lambda - \cos\theta_\mu$	0.080	0.053
$\cos\theta_p - \cos\theta_\mu$	0.025	-0.006
$\varphi_p - \cos\theta_\Lambda$	-0.039	-0.013
$\varphi_p - \cos\theta_p$	0.008	-0.009
$\varphi_p - \cos\theta_\mu$	0.012	0.017
$\varphi_\mu - \cos\theta_\Lambda$	0.020	-0.024
$\varphi_\mu - \cos\theta_p$	-0.018	-0.002
$\varphi_\mu - \cos\theta_\mu$	0.000	-0.014
$\varphi_\mu - \varphi_p$	-0.013	0.015

Table 5.1: Correlation factors between the angular distributions describing the decay $\Lambda_b \to J/\psi(\mu^+\mu^-)\Lambda(p\pi^-)$, as observed in data. The distributions are obtained from events populating the Λ_b ($\overline{\Lambda}_b$) mass peak.

5.2 Angular resolution

The resolutions of the three angular variables of interest for this analysis ($\cos\theta_\Lambda$, $\cos\theta_p$, $\cos\theta_\mu$) are determined from simulated signal events which pass through an identical chain of reconstruction and selection as data. The distributions of the

difference between the simulated and the reconstructed angles (called residuals) are shown in Figure 5.1. The mean values of the histograms, being practically at 0, indicate that no bias is introduced in the reconstruction of the angles. As an estimate of the resolution, the standard deviation of the histograms is considered, which equals 0.005, 0.03 and 0.01 for $\cos\theta_\Lambda$, $\cos\theta_p$ and $\cos\theta_\mu$, respectively.

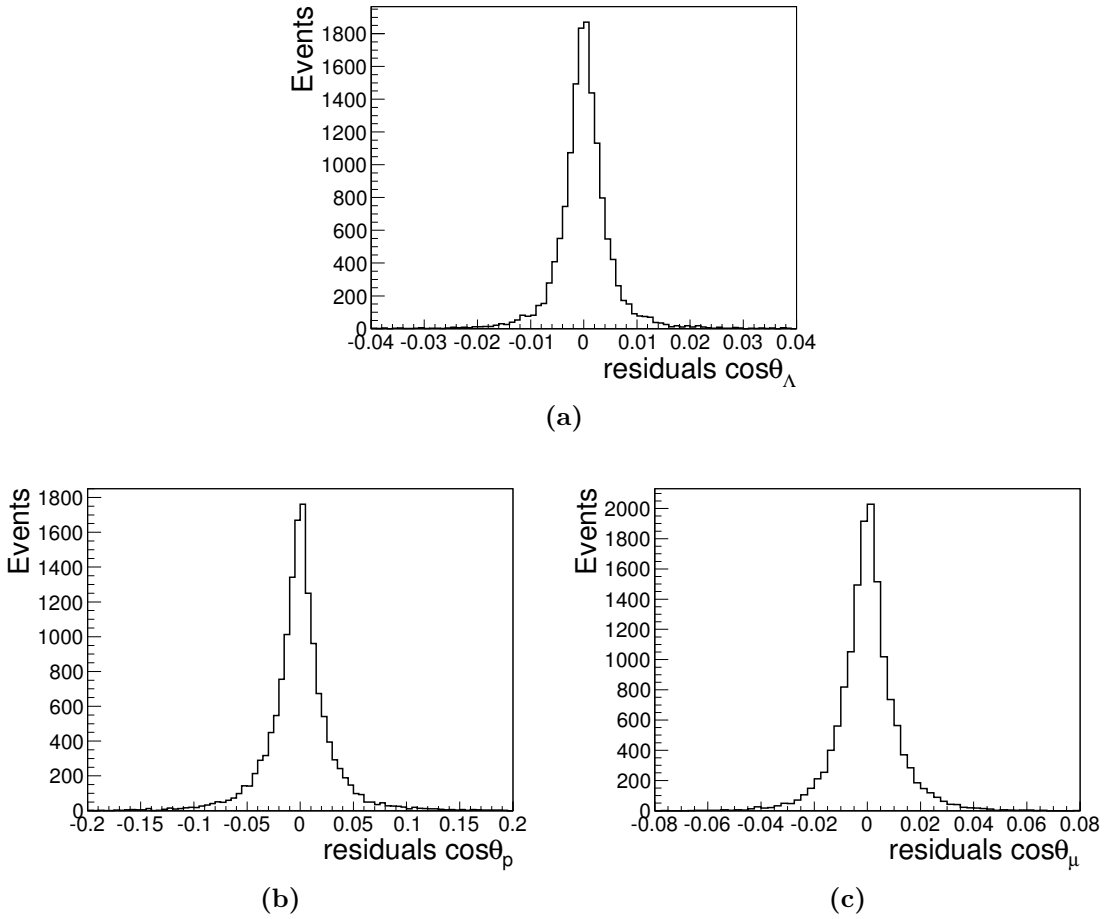

Figure 5.1: Residual distributions for the angular variables $\cos\theta_\Lambda$, $\cos\theta_p$ and $\cos\theta_\mu$. The resolution is given by the standard deviation of the histogram and is measured to be 0.005, 0.03 and 0.01 for $\cos\theta_\Lambda$, $\cos\theta_p$ and $\cos\theta_\mu$, respectively.

5.3 The full extended likelihood function

The measurement of the physics parameters of interest is accomplished by an *unbinned extended maximum likelihood fit* to the data. The framework of RooFit [97] is used for the implementation of the fit. The *extended likelihood function* has the

following general form:

$$L = \exp\Big(-\sum_i N_i\Big) \prod_j \Big[\sum_i N_i \cdot PDF_i\Big] \tag{5.2}$$

where the index i denotes the different components (e.g. signal and background) and j indicates the event. N_i and PDF_i mark the number of events and the probability density function corresponding to the i-th component. For this analysis in particular, considering one signal and one background components, the extended likelihood function transforms to

$$L = \exp(-\mathrm{N_{sig}} - \mathrm{N_{bkg}}) \prod_{\mathrm{j=1}}^{\mathrm{N}} \left[\mathrm{N_{sig}} \cdot \mathrm{PDF_{sig}} + \mathrm{N_{bkg}} \cdot \mathrm{PDF_{bkg}}\right] \tag{5.3}$$

where N_{sig} (N_{bkg}) is the number of observed signal (background) events and N is the total number of events in the sample. The observables involved in the likelihood function are the three angular variables $\Theta = (\cos\theta_\Lambda, \cos\theta_p, \cos\theta_\mu)$. In addition, to better discriminate between signal and background, the invariant mass of the Λ_b candidates is also included. The number of signal (N_{sig}) and background (N_{bkg}) events is obtained in advance from an extended likelihood fit to the invariant mass distribution of the Λ_b candidates (see Table 4.1 and Table 4.2). The so-defined likelihood function L is to be maximized with respect to the set of unknown physics parameters $\alpha = (P, \alpha_1, \alpha_2, \gamma_0)$, defined in Chapter 1.

The probability density functions PDF_{sig} and PDF_{bkg} of the signal and background components are discussed in detail in Section 5.4 and Section 5.5, respectively.

Remark that the likelihood functions related to Λ_b and $\overline{\Lambda}_b$ are separately defined. In the following sections, the upper index "+" is related to Λ_b, while the upper index "−" refers to $\overline{\Lambda}_b$.

5.4 Probability density function of the signal

Hypothetically, ideal experimental conditions involve a perfect detector and event selection which do not introduce any distortion to the signal distributions. In such an idealized case, the probability density function F_{sig} for the angular distributions of the signal in reconstructed and selected data is the same as the signal at particle level described by Eq. 1.31, i.e.

$$F_{sig}(\Theta, \alpha) \equiv \frac{d^3\Gamma}{d\Theta} = \sum_{i=1}^{8} c_i(\alpha) \cdot \eta_i(\alpha) \cdot f_i(\Theta). \tag{5.4}$$

However, in reality the imperfect geometrical acceptance and resolution of the detector and the event selection criteria alter the angular and mass distributions. Distortions of the angular distributions are taken into account by an efficiency term $\epsilon(\Theta)$ determined from simulated signal statistics, which is discussed in detail in Section 5.6. The invariant mass distribution $m(J/\psi\,\Lambda)$ of the signal is modeled by a sum of two Gaussians with a common mean, $G(m;\mu,\sigma_1,\sigma_2,f)$, as defined in Eq. 4.3. Thus, the signal component in the likelihood function in Eq. 5.3 has the following form:

$$PDF_{sig}^{+(-)} = F_{sig}^{+(-)}(\Theta,\alpha)\cdot\epsilon(\Theta)^{+(-)}\cdot G^{+(-)}(m;\mu,\sigma_1,\sigma_2,f). \tag{5.5}$$

The four parameters of the double Gaussian are set to the values listed in Table 4.1, which are obtained in advance by a fit to the $(J/\psi\,\Lambda)$ invariant mass distribution.

5.5 Probability density function of the background

The probability density function of the background component in the likelihood function (Eq. 5.3) is obtained by analyzing events populating the sidebands of the Λ_b candidates mass peak in data. The selected range of the sidebands is $m(J/\psi\,\Lambda) \in [5.40, 5.54] \cup [5.70, 5.84]$ GeV/c^2. According to the likelihood fit to the invariant mass distribution (Section 4.3.3), this range is sufficiently off the peak and does not contain signal Λ_b candidates. The shapes of the background angular distributions are parametrized. The simplest functions found to describe the data are sequences of Chebyshev polynomials of the 1st kind (for $\cos\theta_\Lambda$ and $\cos\theta_p$) and error functions (for $\cos\theta_\mu$) [79]. The parametrizing functions are combined as follows:

$$F_{bkg}^{+(-)}(\Theta) = \left(\sum_{i=0}^{5} A_i^{+(-)}\cdot T_i(\cos\theta_\Lambda)\right)\cdot\left(\sum_{j=0}^{3} B_j^{+(-)}\cdot T_j(\cos\theta_p)\right)\cdot E^{+(-)}(\cos\theta_\mu) \tag{5.6}$$

In the above expression, $T_{i(j)}$ denote Chebyshev polynomials of the 1st kind of degree $i(j)$, $A_i^{+(-)}$ and $B_j^{+(-)}$ are free coefficients and $E^{+(-)}$ is defined as

$$\begin{aligned} E^{+(-)}(x) &= \left[k_0^{+(-)}\left(1+\mathrm{erf}\left((x-k_1^{+(-)})/k_2^{+(-)}\right)\right)+k_3^{+(-)}\right] \\ &\times \left[k_0^{+(-)}\left(1+\mathrm{erf}\left((-x-k_4^{+(-)})/k_5^{+(-)}\right)\right)+k_6^{+(-)}\right] \end{aligned} \tag{5.7}$$

with free parameters $k_0^{+(-)}$ to $k_6^{+(-)}$.

The invariant mass distribution of the background is assumed to be linear and is modeled by a first order polynomial function $P^{+(-)}$, as defined in Eq. 4.4, with coefficients listed in Table 4.1.

Finally, the full probability density function of the background is given by the product of the angular and mass PDFs, resulting in

$$PDF_{bkg}^{+(-)} = F_{bkg}^{+(-)}(\Theta) \cdot P^{+(-)}(m). \tag{5.8}$$

$PDF_{bkg}^{+(-)}$ is used for an unbinned likelihood fit to the angular and mass distributions from the data sidebands in order to determine the free coefficients which parametrize the shapes of the background angular distributions. To account for possible correlations, the fit is performed simultaneously to the four distributions. The angular distributions and the fit are shown separately for particles and antiparticles in Figure 5.2 and Figure 5.3, respectively. The chosen parametrization functions describe well the shapes of the angular distributions. The corresponding to the plots χ^2 per degree of freedom are listed in Table 5.2.

	χ^2/ndf, particles	χ^2/ndf, antiparticles
$\cos\theta_\Lambda$	1.18	1.11
$\cos\theta_p$	0.90	1.88
$\cos\theta_\mu$	1.49	0.52

Table 5.2: χ^2 per degree of freedom of fits to the angular distributions from data sidebands, shown in Figure 5.2 and Figure 5.3.

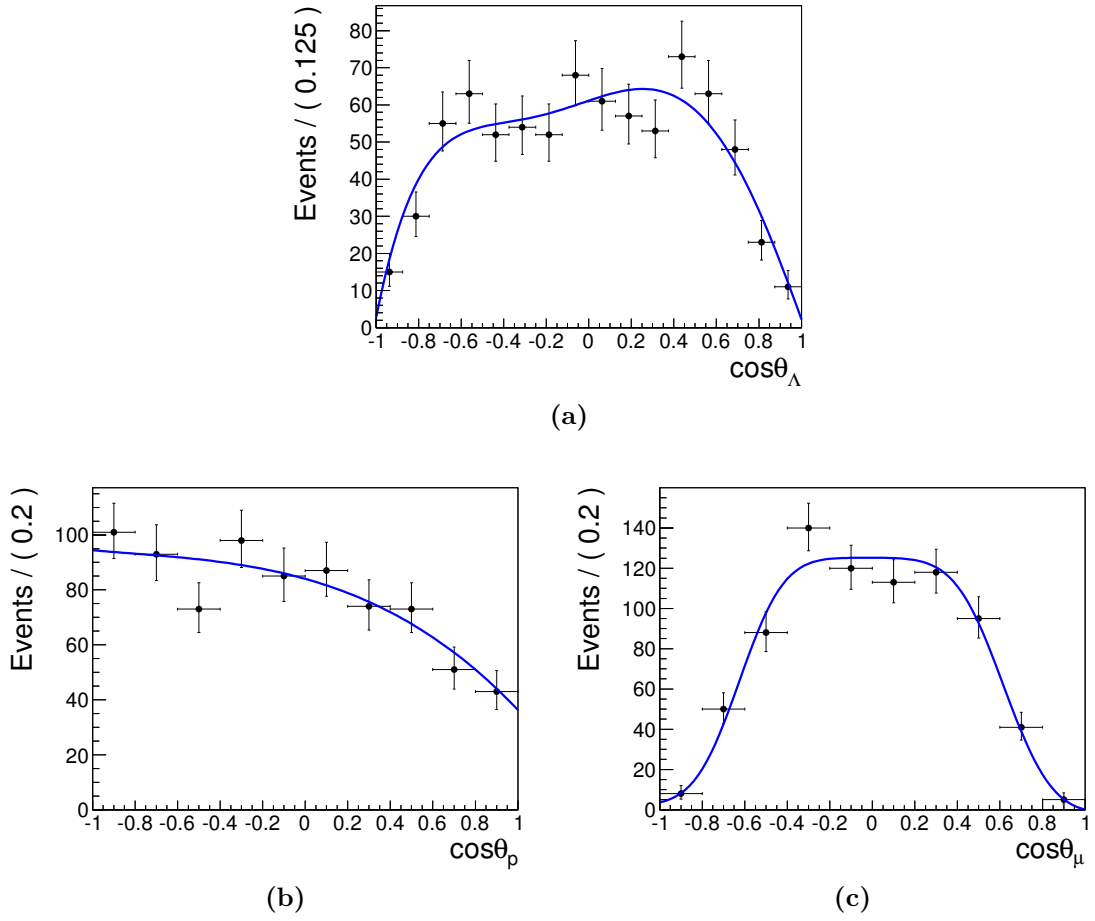

Figure 5.2: Angular distributions from sidebands of the Λ_b candidates mass peak in data. (a) $\cos\theta_\Lambda$ (b) $\cos\theta_p$ (c) $\cos\theta_\mu$. The solid line shows fit to the data.

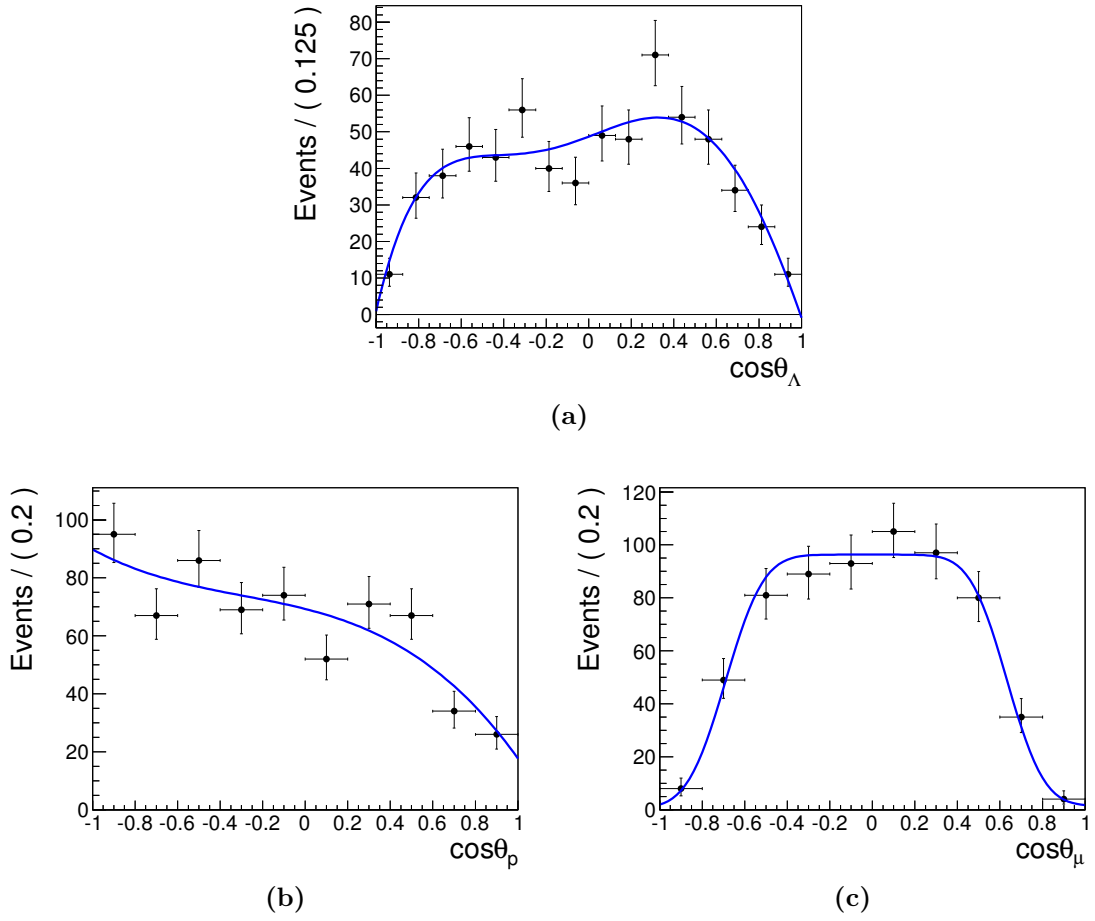

Figure 5.3: Angular distributions from sidebands of the $\overline{\Lambda}_b$ candidates mass peak in data. (a) $\cos\theta_\Lambda$ (b) $\cos\theta_p$ (c) $\cos\theta_\mu$. The solid line shows fit to the data.

5.6 Angular efficiency shapes

The genuine shapes of the angular distributions are distorted due to effects deriving from the geometry of the detector and the event reconstruction and selection procedure. For the needs of this analysis the absolute efficiency, in terms of fraction of successfully reconstructed and selected events out of the initial generated sample, is not of interest. The property of relevance are the shapes of the distortions introduced by detector, reconstruction and selection effects. In the likelihood function Eq. 5.3 this is accounted for by introducing an efficiency shape term $\epsilon(\Theta)$ which disturbs the original signal $F_{sig}(\Theta, \alpha)$ (see Eq. 5.5). The angular efficiency shapes are determined from simulation in which the angular distributions in the corresponding rest frames are generated flat, as shown in Figure 5.4. The effect of the entire event detection, reconstruction and selection chain can be seen in the angular distributions shown in Figure 5.5 and Figure 5.6 for samples of Λ_b and $\overline{\Lambda}_b$, respectively. Clearly, the originally flat distributions at particle level are observed drastically deformed at detector level. The shapes of the distributions in Figure 5.5 and Figure 5.6 are parametrized. The simplest functions found to match the distributions are series of Chebyshev polynomials of the 1st kind [79]. The distributions are similar, although not identical for the samples of Λ_b and $\overline{\Lambda}_b$, which requires the efficiency shapes for particles and antiparticles to be separately parametrized. The efficiency shape term $\epsilon(\Theta)$ is then defined as the following product:

$$\begin{aligned}\epsilon^{+(-)}(\cos\theta_\Lambda, \cos\theta_p, \cos\theta_\mu) &= \left(\sum_{i=0}^{6} A_i^{+(-),eff} \cdot T_i(\cos\theta_\Lambda)\right) \\ &\cdot \left(\sum_{j=0}^{3} B_j^{+(-),eff} \cdot T_j(\cos\theta_p)\right) \\ &\cdot \left(\sum_{k=0}^{6} C_k^{+(-),eff} \cdot T_k(\cos\theta_\mu)\right), \end{aligned} \tag{5.9}$$

where $A_i^{+(-),eff}$, $B_j^{+(-),eff}$ and $C_k^{+(-),eff}$ are free coefficients in front of the Chebyshev polynomials $T(x)$ of i-th, $j-$th and k-th order, respectively. $\epsilon(\Theta)$ is used for an unbinned likelihood fit which aims to evaluate the coefficients $A_i^{+(-),eff}$, $B_j^{+(-),eff}$ and $C_k^{+(-),eff}$. It is performed simultaneously on the three angular distributions $\cos\theta_\Lambda$, $\cos\theta_p$ and $\cos\theta_\mu$ in order to take into account possible correlations between the angles. The fit to the simulated angular distributions is shown with solid line in Figure 5.5 and Figure 5.6. As can be seen from the plots, the chosen for the parametrization polynomial functions describe very well the shapes of the distributions. Information on the goodness-of-fit in terms of χ^2 per degree of freedom is provided in Table 5.3.

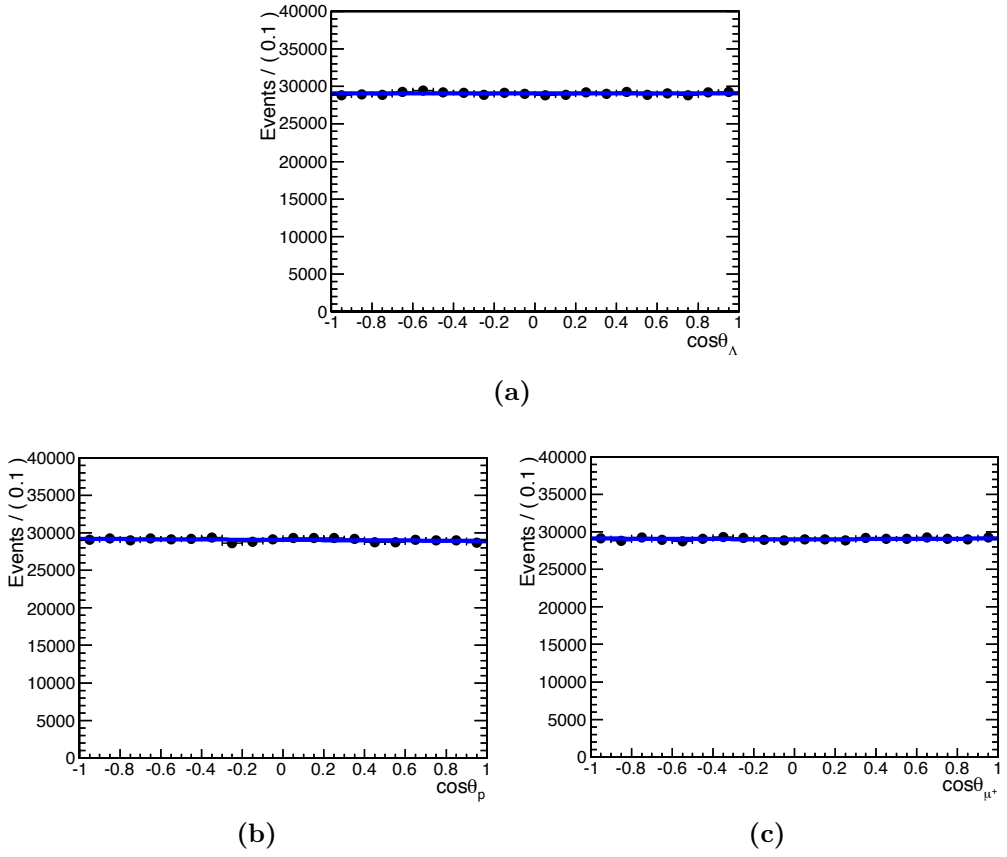

(a) **(b)** **(c)**

Figure 5.4: Flat generated angular distributions at particle level.

	χ^2/ndf, particles	χ^2/ndf, antiparticles
$\cos\theta_\Lambda$	0.49	0.83
$\cos\theta_p$	1.61	0.84
$\cos\theta_\mu$	0.59	1.08

Table 5.3: χ^2 per degree of freedom of fits to the efficiency shape distributions shown in Figure 5.5 and Figure 5.6.

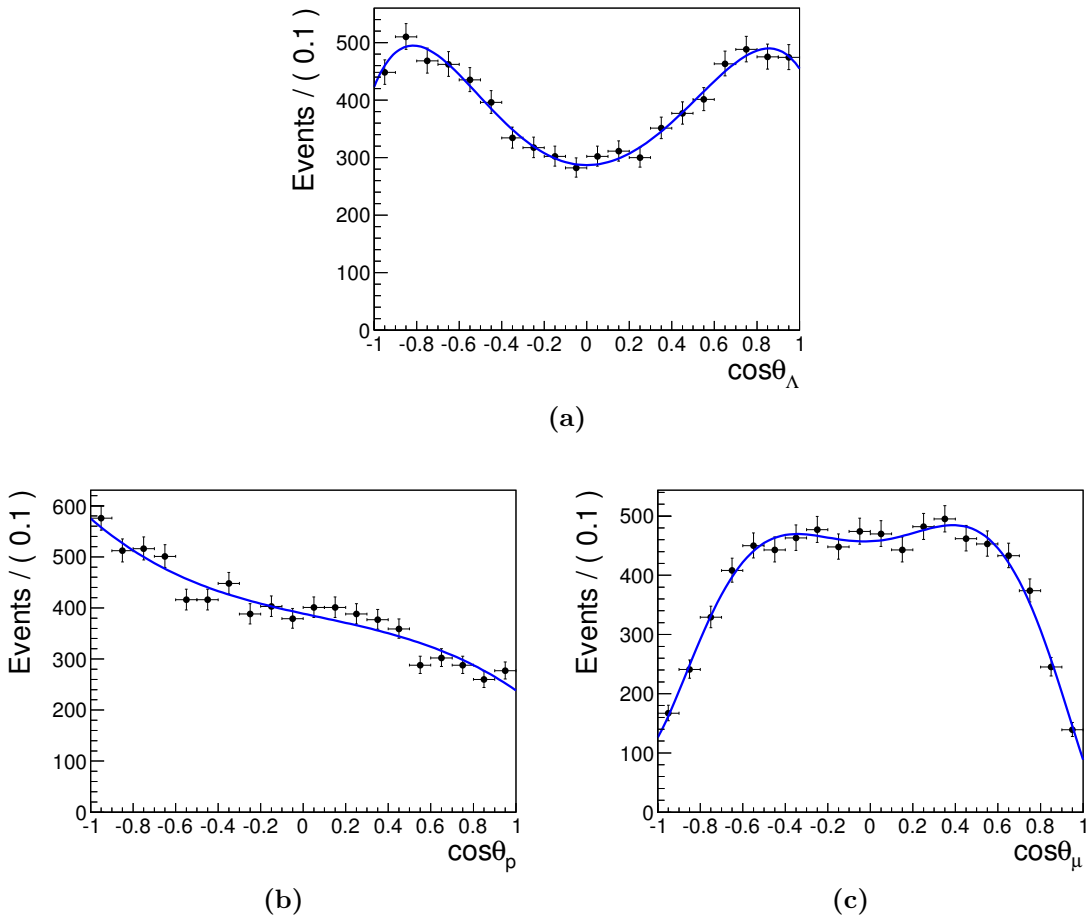

Figure 5.5: Angular distributions (in black) from simulated Λ_b samples after full detector reconstruction and selection, starting from flat generated distributions (see Figure 5.4). The angular efficiency shapes $\epsilon^+(\Theta)$ are parametrized with a series of Chebychev polynomials fitted simultaneously to the three angular distributions (shown in blue).

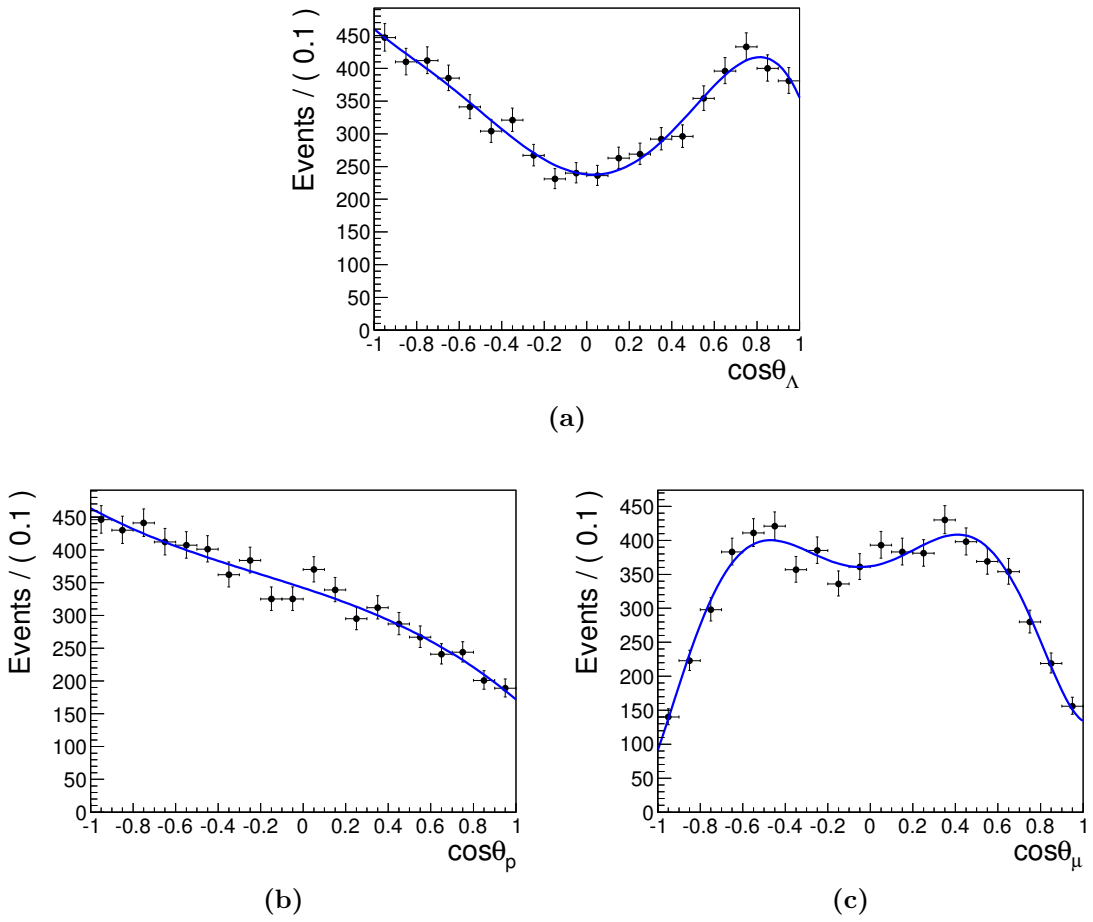

Figure 5.6: Angular distributions (in black) from simulated $\overline{\Lambda}_b$ samples after full detector reconstruction and selection, starting from flat generated distributions (see Figure 5.4). The angular efficiency shapes $\epsilon^{-}(\Theta)$ are parametrized with a series of Chebychev polynomials fitted simultaneously to the three angular distributions (shown in blue).

5.7 Validation of the likelihood fit

The following section describes several tests of the fit stability. Special attention is given to the effect of the sample size on the fit performance.

5.7.1 Validation of the fit to the signal model

To test the accurate implementation and performance of the fit, it is first validated with the undisturbed signal polarization model with the use of generated samples of polarized Λ_b and $\overline{\Lambda}_b$ particles. The samples are not put through further detector simulation and reconstruction steps and therefore they are not affected by any efficiency effects. The function $F_{sig}^{+(-)}(\Theta, \alpha)$ is fitted to the generated angular distributions. The fit is applied simultaneously to the samples of Λ_b and $\overline{\Lambda}_b$, each containing approximately 150,000 events. The input values in the simulation and the results of the fit are summarized in Table 5.4. The output of the fit for all five physics parameters is perfectly consistent with the input values in the simulation.

Parameter	Input value	Fit result	Stat. error
P^+	0.500	0.500	0.011
P^-	-0.500	-0.508	0.011
α_1	0.461	0.462	0.008
α_2	0.687	0.691	0.005
γ_0	0.257	0.247	0.008

Table 5.4: Results from a likelihood fit of the undisturbed signal PDF $F_{sig}^{+(-)}(\Theta, \alpha)$ applied to generated polarized Monte Carlo events. The samples contain approximately 150,000 Λ_b and 150,000 $\overline{\Lambda}_b$ events. The output of the fit is in excellent agreement with the input in the simulation.

The stability of the fit performance is probed with samples of test statistics (*toy Monte Carlo*) in which the distributions are generated according to the signal PDF $F_{sig}^{+(-)}(\Theta, \alpha)$. The samples serve as inputs for the likelihood fit of the same PDF, thus probing if the fit is able to obtain back the input values for each sample. This manner allows for a large number of pseudo-experiments to be conducted, probing the fit performance for various sets of values for the input parameters $\alpha = (P^+, P^-, \alpha_1, \alpha_2, \gamma_0)$. The results from the pseudo-experiments are used to examine the pull distributions for every fitted parameter, where the pull of the quantity x in the i-th pseudo-experiment is defined as

$$PULL(x_i) = \frac{x_i^{fit} - x_i^{true}}{\sigma_i^{fit}} \tag{5.10}$$

with x_i^{fit} being the fitted value, x_i^{true} is the true (generated) value and σ_i^{fit} is the calculated by the fit error on x_i^{fit}. Stable performance of the fit, meaning not introducing any bias in the results and their errors, suggests normally distributed pulls with a mean value at 0 and a standard deviation of 1.

The pull distributions resulting from 1,000 test samples, each containing 100,000 Λ_b and 100,000 $\overline{\Lambda}_b$ events, are shown in Figure 5.7. The mean and widths of the fitted Gaussian functions are listed in Table 5.5. The results indicate that with this large number of events (200,000) the performance of the fit is excellent and no bias is introduced for any of the 5 fitted parameters.

The study is repeated with 1,000 low-statistic samples in which the numbers of generated Λ_b and $\overline{\Lambda}_b$ events correspond to the observed numbers in data. The resulting pull distributions are shown in Figure 5.8 and the output of the fitted Gaussian functions is given in Table 5.5. The results give an indication for a bias in the measurement of one of the five fit parameters, namely the parameter α_1. This signals that the performance of the fit can be affected by a small sample size. A systematic uncertainty associated with the bias of the fit is addressed in Section 5.10.

Parameter	High statistics		Low statistics	
	Pull μ	Pull σ	Pull μ	Pull σ
P^+	0.038 ± 0.032	1.016 ± 0.023	-0.069 ± 0.034	1.064 ± 0.024
P^-	0.035 ± 0.030	0.945 ± 0.021	-0.034 ± 0.032	1.019 ± 0.023
α_1	-0.035 ± 0.031	0.984 ± 0.022	-0.192 ± 0.042	1.331 ± 0.030
α_2	-0.045 ± 0.032	1.012 ± 0.023	-0.010 ± 0.032	0.998 ± 0.022
γ_0	0.006 ± 0.033	1.040 ± 0.023	0.028 ± 0.031	0.985 ± 0.022

Table 5.5: Validation of the signal model fit with pseudo-experiments. Mean and standard deviation values are given for Gaussian fits applied to the pull distributions from 1,000 pseudo-experiments with high statistics (∼200,000 entries) and low statistics (∼2,000 entries).

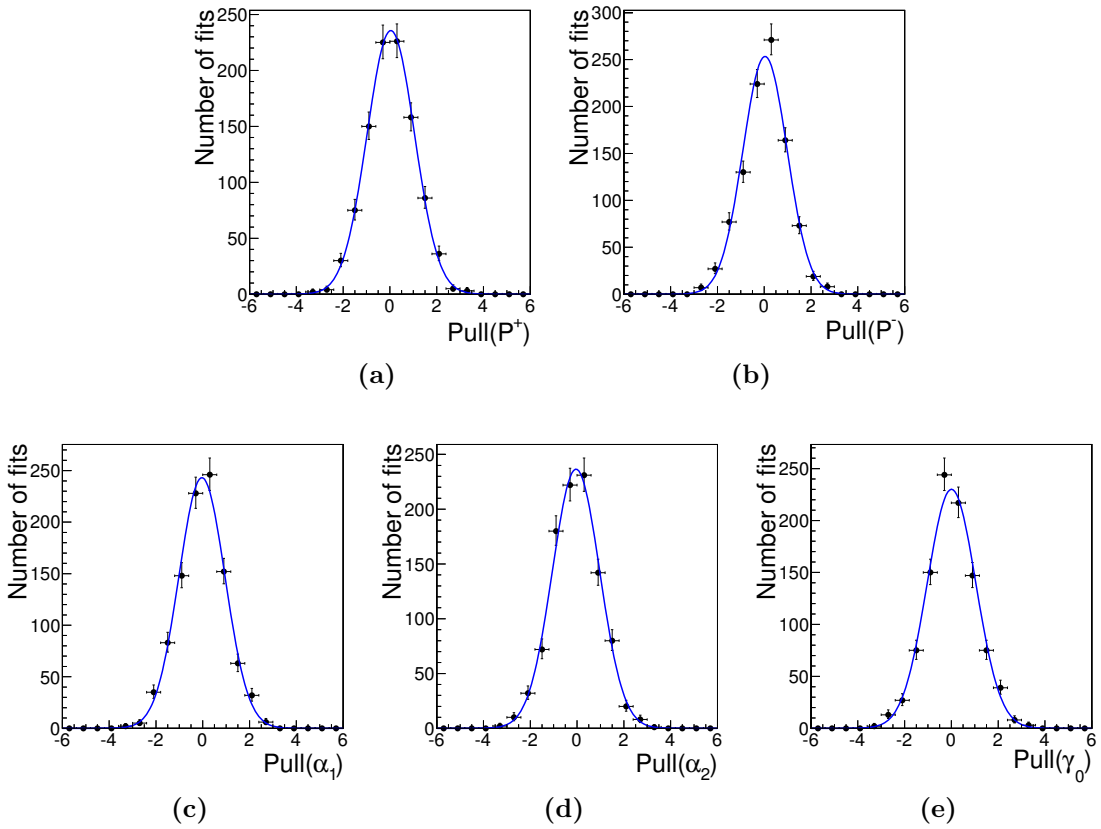

Figure 5.7: Pull distributions from 1,000 pseudo-experiments simulating the undisturbed signal polarization model. Each test sample consists of ∼200,000 events.

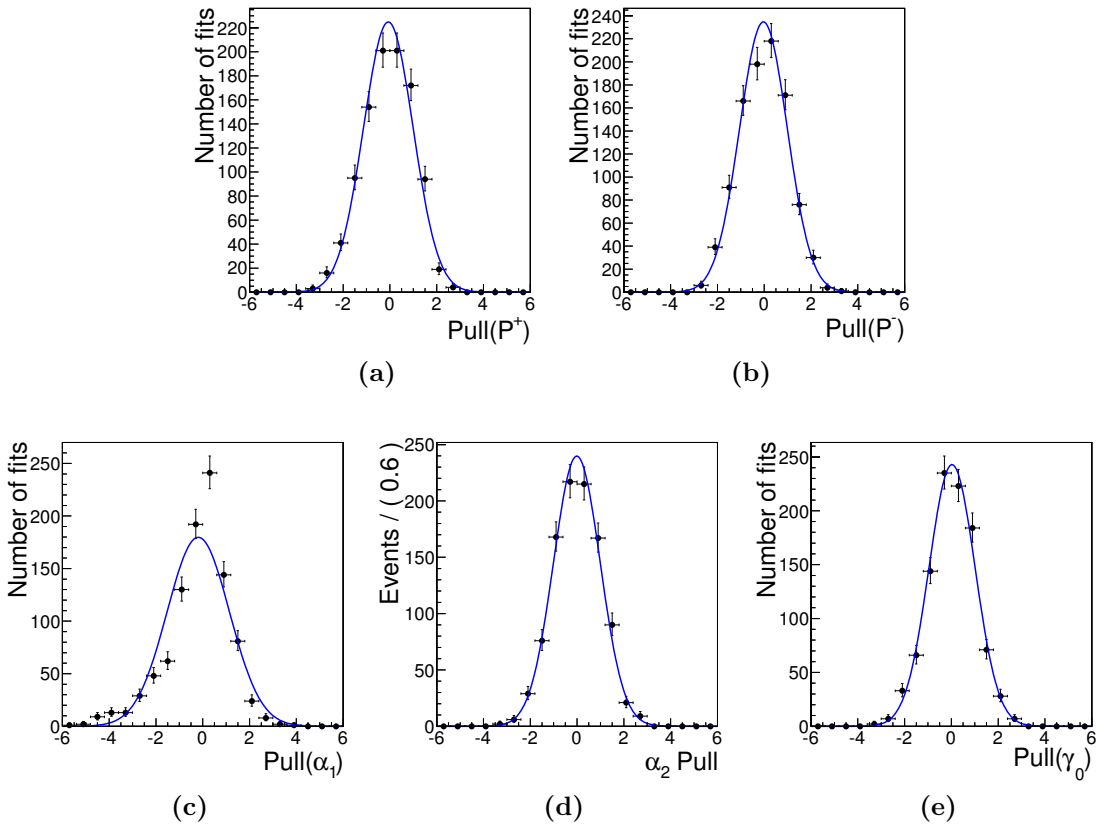

Figure 5.8: Pull distributions from 1,000 pseudo-experiments simulating the undisturbed signal polarization model. Each test sample consists of ∼2,000 events.

5.7.2 Validation of the full likelihood fit

The angular efficiency shapes and the background terms in the likelihood function can, in principle, be a source of biases in the fit results. This is investigated in a similar way as the fit to the undisturbed signal model. 1,000 samples of test statistics are generated from the PDF in the full likelihood function (see Eq. 5.3), describing the three angular distributions ($\cos\theta_\Lambda, \cos\theta_p, \cos\theta_\mu$) and the invariant mass distribution $m(J/\psi\,\Lambda)$. All parameters related to the background and efficiency terms are fixed as described in Section 5.5 and Section 5.6, respectively. The number of signal and background entries for Λ_b and $\overline{\Lambda}_b$ is set in accordance with the observed numbers in data (see Table 4.2). The full 4-dimensional likelihood fit is then applied to each test sample. As can be seen in Figure 5.9, the resulting pull distributions for the fitted parameters are well described by Gaussian functions except for the parameter α_1, which replicates the observations for this parameter in Section 5.7.1. The mean values and the standard deviations of the fitted Gaussians are listed in Table 5.6. The results indicate that the fitting procedure biases the measured parameter α_2 towards lower values. In addition, the uncertainties of the parameters P^+, P^- and α_1 tend to be underestimated by the fit. Systematic uncertainties associated with these observations are addressed in Section 5.10.

Parameter	Low statistics	
	Pull μ	Pull σ
P^+	-0.008 ± 0.038	1.214 ± 0.027
P^-	-0.009 ± 0.039	1.163 ± 0.028
α_1	-0.039 ± 0.113	1.415 ± 0.113
α_2	-0.172 ± 0.032	1.001 ± 0.024
γ_0	0.003 ± 0.032	1.020 ± 0.023

Table 5.6: Validation of the full likelihood fit model with pseudo-experiments. Mean and standard deviation values of Gaussian fits applied to the pull distributions from 1,000 pseudo-experiments with a number of entries consistent with the observations in data.

The performance of the full likelihood fit is further tested at an environment which resembles as much as possible the real data. Samples of Λ_b and $\overline{\Lambda}_b$ are generated and put through the full simulation and reconstruction chain of CMS. The events are subject to identical reconstruction and selection criteria as data. The simulated signal entries are mixed with background events from the sidebands of the invariant mass distribution $m(J/\psi\,\Lambda)$ in data (see Figure 4.4). The number of signal and background events for the samples of Λ_b and $\overline{\Lambda}_b$ follows the observations

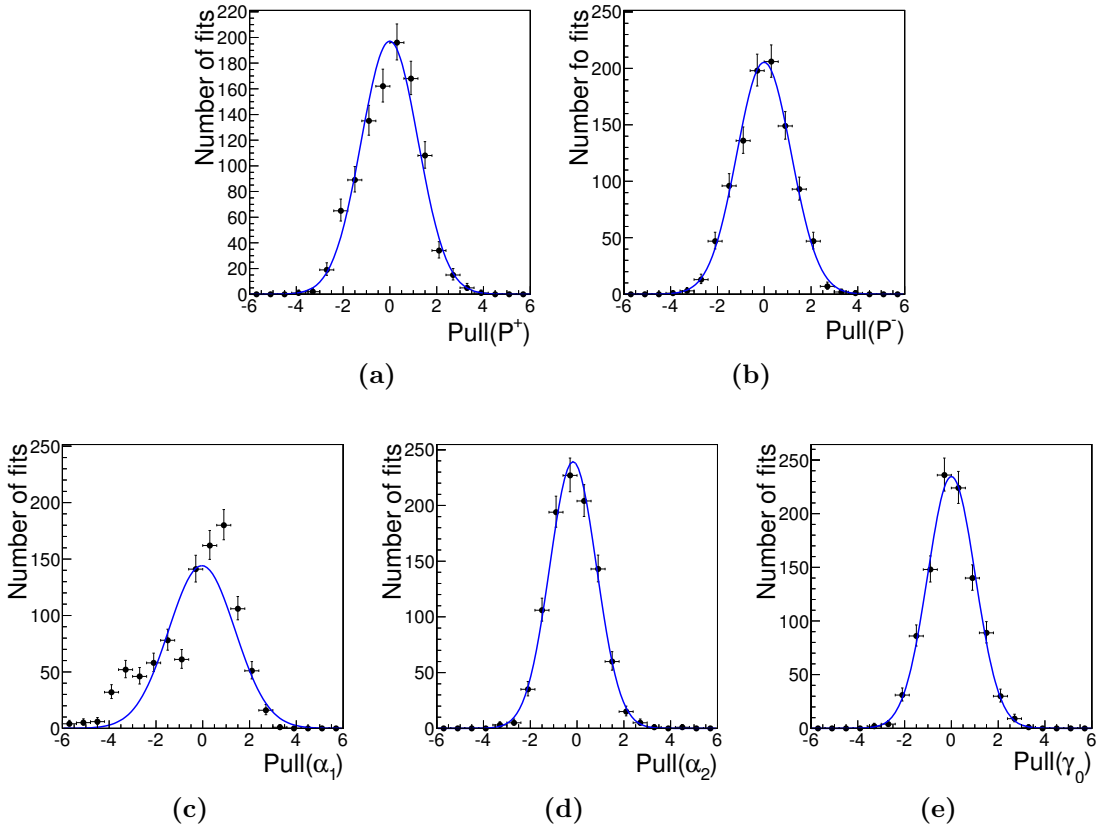

Figure 5.9: Pull distributions from 1,000 pseudo-experiments simulating the full fit model. The test samples are generated from the PDF in the full likelihood function (see Eq. 5.3), which includes signal, efficiency and background terms. The numbers of signal and background entries correspond to the observed numbers in data.

in the data which are listed in Table 4.2. The mixture of simulated signal events and background data events serves as an input for the full likelihood fit performed on the angular distributions $(\cos\theta_\Lambda, \cos\theta_p, \cos\theta_\mu)$. The invariant mass is not included in the fit since the background events in the sample populate only the sidebands mass range. The capability of the fit to obtain the input values in the simulated signal is tested with samples in which the polarization of Λ_b and $\overline{\Lambda}_b$ is set to zero. The angular distributions and the fit are shown in Figure 5.10. As can be seen in the plots, the full likelihood fit generally describes very well the angular distributions. The separate contributions of the signal (folded with the angular efficiency) and the background components of the fit are as well displayed in order to provide a better understanding of the sample composition. A comparison of the expected parameter values and the outcome of the fit (Table 5.7) reveals good agreement; the largest discrepancy observed is approximately two statistical standard deviations.

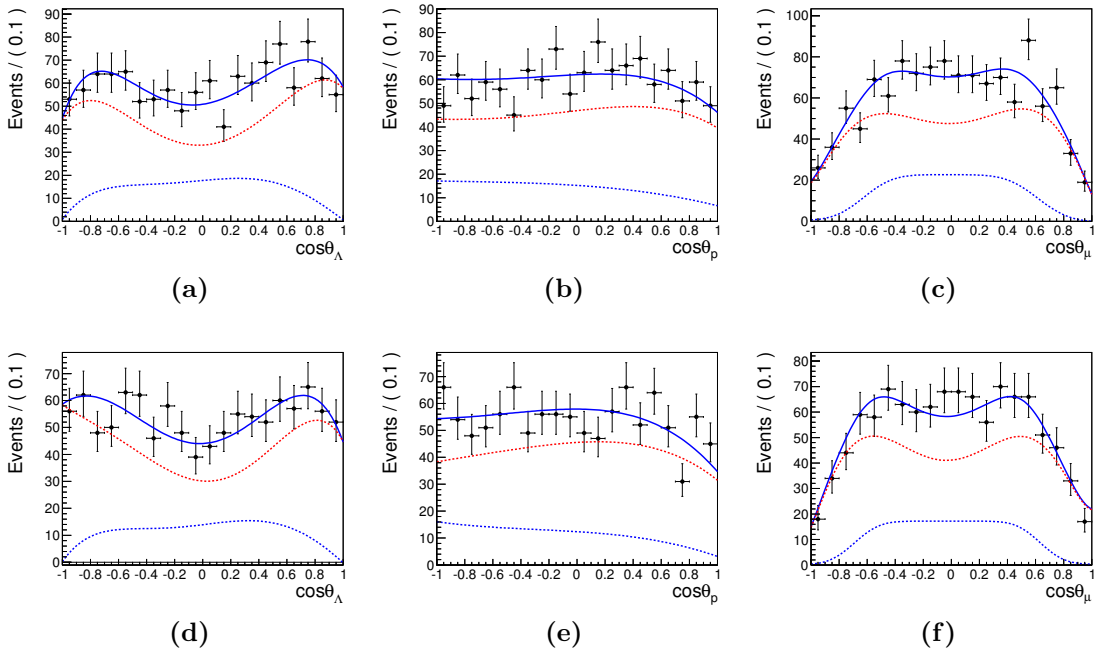

Figure 5.10: Validation of the full likelihood fit to simulated samples of Λ_b (a), (b), (c), and $\overline{\Lambda}_b$ (d), (e), (f), merged with background events from data. The numbers of signal and background events correspond to the observed numbers in data. The projection of the total fit is shown in solid blue line, the signal folded with efficiency in dashed red, and the background component in dashed blue.

5.8 Full likelihood fit to data

The full likelihood function defined in Eq. 5.3 is used to perform an unbinned extended maximum likelihood fit to the data. Each term entering the likelihood function is separately determined for Λ_b and $\overline{\Lambda}_b$ decays, leading to functions of the form

$$L^{+(-)} = \exp\left(-N_{sig}^{+(-)} - N_{bkg}^{+(-)}\right) \prod_{j=1}^{N^{+(-)}} \left[N_{sig}^{+(-)} \cdot F_{sig}^{+(-)}(\Theta, \alpha) \cdot \epsilon^{+(-)} \cdot G^{+(-)} + N_{bkg}^{+(-)} \cdot PDF_{bkg}^{+(-)}\right], \tag{5.11}$$

where all terms are as defined in Section 5.3 to Section 5.6. Except for $F_{sig}^{+(-)}$, all terms in the likelihood function are fixed. The set of free parameters $\alpha = (P^{+(-)}, \alpha_1, \alpha_2, \gamma_0)$ is contained only in the term $F_{sig}^{+(-)}$ defined in Eq. 5.4. The fit is performed in three different manners, as described below.

1. The fit is performed simultaneously to the samples of Λ_b and $\overline{\Lambda}_b$ candidates, using events from the $(J/\psi\,\Lambda)$ invariant mass peak in the range $m(J/\psi\,\Lambda) \in [5.57, 5.67]$ GeV/c^2. The choice of the mass range is motivated by a preliminary

Parameter	Input value	Fit result	Deviation
P^+	0.000	-0.138 ± 0.102	-1.35σ
P^-	0.000	0.004 ± 0.093	0.04σ
α_1	0.461	0.752 ± 0.279	1.04σ
α_2	0.687	0.615 ± 0.069	-1.04σ
γ_0	0.257	0.537 ± 0.136	2.06σ

Table 5.7: Validation of the full likelihood fit performed to signal events from full detector simulation mixed with background events from data. The numbers of signal and background events in the sample correspond to the observed numbers in data. Quoted errors are statistical errors only.

fit to the invariant mass distribution (see Section 4.3.3), pointing that the selected range contains more than 99% of the signal events. A decision to use the likelihood function L^+ or L^- is made on event by event basis, taking into account whether the reconstructed candidate is a particle or antiparticle. The simultaneous fitting strategy requires that two independent parameters P^+ and P^- are used for the polarization in the signal probability density function F^+_{sig} and F^-_{sig}, respectively. Therefore, the set of free parameters in the likelihood fit is $\alpha = (P^+, P^-, \alpha_1, \alpha_2, \gamma_0)$. Given the limited number of signal events observed in the data, this approach exploits the maximum available statistics and benefits from smaller statistical errors for the shared parameters of the fit (α_1, α_2 and γ_0). For the presented angular analysis, this approach is considered as most favorable.

2. The fit is performed simultaneously to the samples of particles and antiparticles, using events from the invariant mass peak and the sidebands in the range $m(J/\psi\,\Lambda) \in [5.40, 5.84]$ GeV/c^2. This manner serves as a cross-check of the first approach. The difference consists in introducing more background events (from the sidebands) while the number of signal events remains the same. Given that all free parameters in the fit are related only to the signal PDF while all parameters describing the background are fixed, then adding more background events does not add information about the free parameters. Therefore, it is expected that the results and the statistical errors estimated in this way should be the same as the ones obtained with the first approach, where only events from the mass peak are exploited.

3. The samples of particles and antiparticles are fit separately using events from the invariant mass peak in the range $m(J/\psi\,\Lambda) \in [5.57, 5.67]$ GeV/c^2. This

procedure serves as an additional cross-check of the first described approach. Splitting the whole data sample into particles and antiparticles and fitting the two sub-samples independently should increase the statistical errors but the results should stay consistent within the uncertainties.

5.9 Results

The results of the likelihood fit to data, performed in the three different manners described in Section 5.8, are summarized in Table 5.8. The first approach, which is considered optimal, results in a polarization of 0.03 ± 0.09 and 0.02 ± 0.08 for Λ_b and $\overline{\Lambda}_b$, respectively. The relevant data distributions along with the fit projections are shown in Figure 5.11 (Λ_b) and Figure 5.12 ($\overline{\Lambda}_b$).

The outcome of the second approach, which includes events populating the sidebands of the Λ_b candidates mass peak, is perfectly consistent with the first set of results. As expected, the magnitude of the statistical errors is not influenced by including additional background events from the sidebands. The third approach, fitting the samples of Λ_b and $\overline{\Lambda}_b$ candidates separately, yields results which are in agreement within the statistical uncertainties with the outcome of the simultaneous fit. In this case the results are obtained from approximately half of the statistics compared to the simultaneous fit to Λ_b and $\overline{\Lambda}_b$ candidates. This leads to larger statistical uncertainties, scaled by a factor $\sim\sqrt{2}$, for the shared fit parameters α_1, α_2 and γ_0.

The results from the different fit approaches, listed in Table 5.8, are consistent within $\sim 1\sigma$ where the given errors are the statistical uncertainties as obtained by the fit. Note that the values obtained for the parameter α_2, namely $\alpha_2 < -1$, are outside the physical range of $-1 \leq \alpha_2 \leq 1$. A tendency to obtain values lower than the true ones for this parameter is observed in tests of the fit stability, performed with pseudo-experiments (see Table 5.6).

To give a notion of the genuine signal angular distributions, they are simulated with the signal model given by Eq. 1.31, with the physics parameters obtained from the fit to data. The outcome is shown in Figure 5.13.

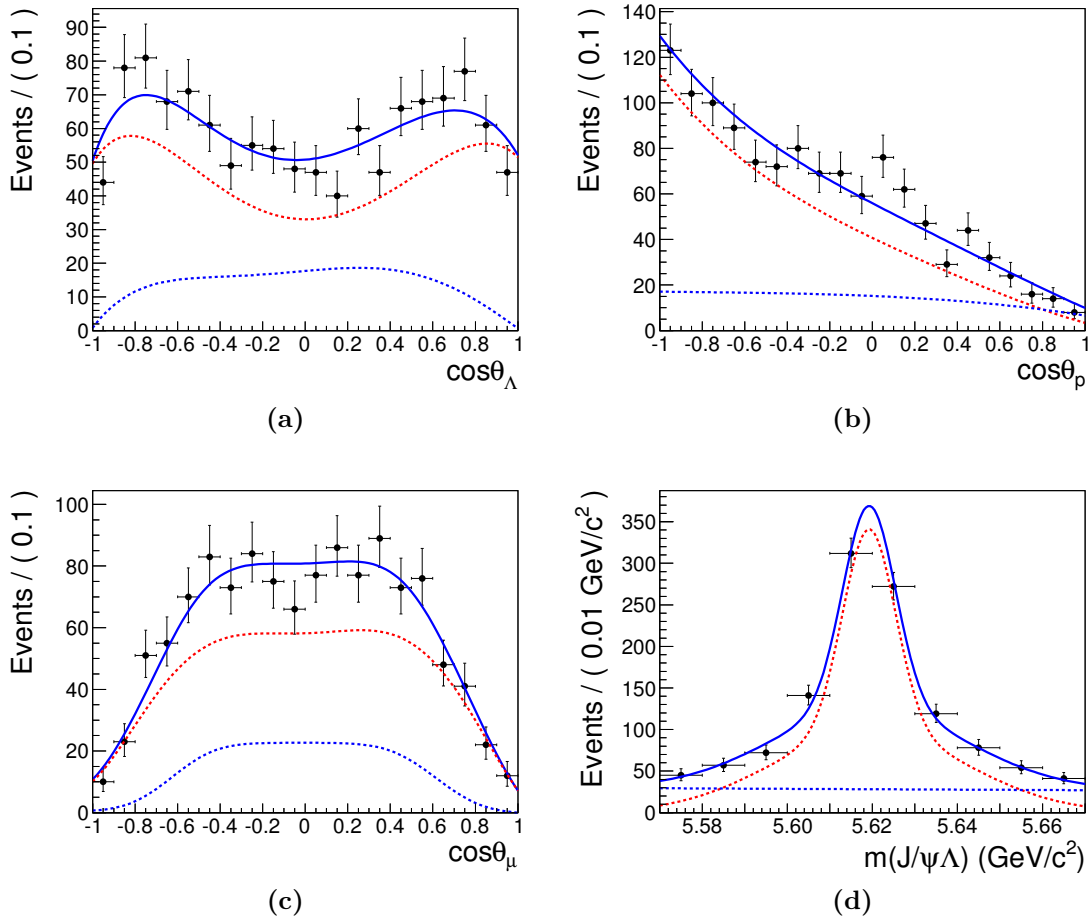

Figure 5.11: The full likelihood fit to data. Projections of the fit result in (a) $\cos\theta_\Lambda$, (b) $\cos\theta_p$, (c) $\cos\theta_\mu$, (d) $m(J/\psi\,\Lambda)$, for Λ_b candidates. The projection of the total fit is shown in solid blue line, the signal folded with efficiency in dashed red, and the background component in dashed blue.

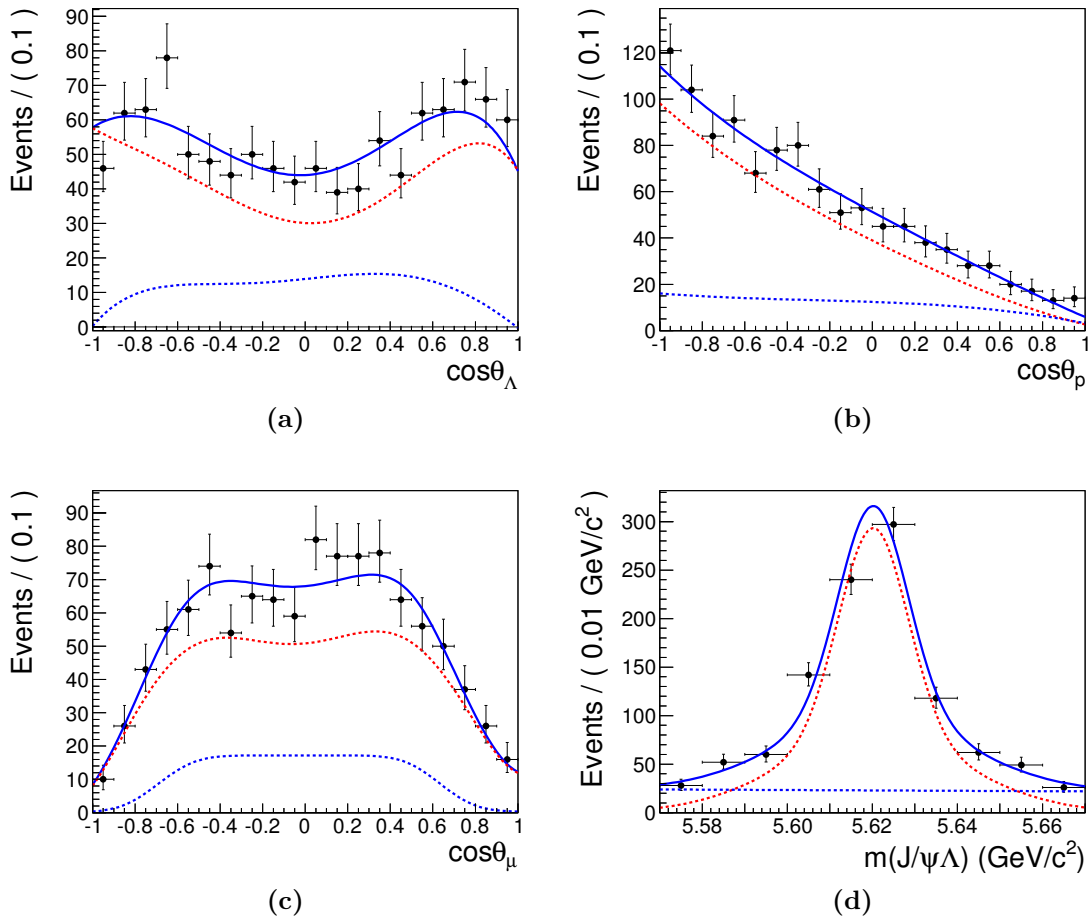

Figure 5.12: The full likelihood fit to data. Projections of the fit result in (a) $\cos\theta_\Lambda$, (b) $\cos\theta_p$, (c) $\cos\theta_\mu$, (d) $m(J/\psi\,\Lambda)$, for $\overline{\Lambda}_b$ candidates. The projection of the total fit is shown in solid blue line, the signal folded with efficiency in dashed red, and the background component in dashed blue.

Parameter	Fit results			
	$\Lambda_b + \overline{\Lambda}_b$ (peak)	$\Lambda_b + \overline{\Lambda}_b$ (peak+sidebands)	Λ_b (peak)	$\overline{\Lambda}_b$ (peak)
P^+	0.03 ± 0.09	0.03 ± 0.09	0.07 ± 0.13	—
P^-	0.02 ± 0.08	0.02 ± 0.08	—	-0.04 ± 0.06
α_1	0.47 ± 0.24	0.48 ± 0.24	0.17 ± 0.35	-0.81 ± 0.31
α_2	-1.31 ± 0.07	-1.31 ± 0.07	-1.42 ± 0.11	1.17 ± 0.10
γ_0	-0.51 ± 0.14	-0.50 ± 0.14	-0.72 ± 0.20	-0.57 ± 0.20

Table 5.8: Summary of results from the full likelihood fit to data, obtained in three different manners (see text). The errors quoted are the statistical errors as obtained by the likelihood fit. Note that the parameters α_1 and α_2 for $\overline{\Lambda}_b$ have opposite signs compared to Λ_b, as a result of the relations between particles and antiparticles (see Eq. 1.28 and Eq. 1.30) which are taken into account in the likelihood function.

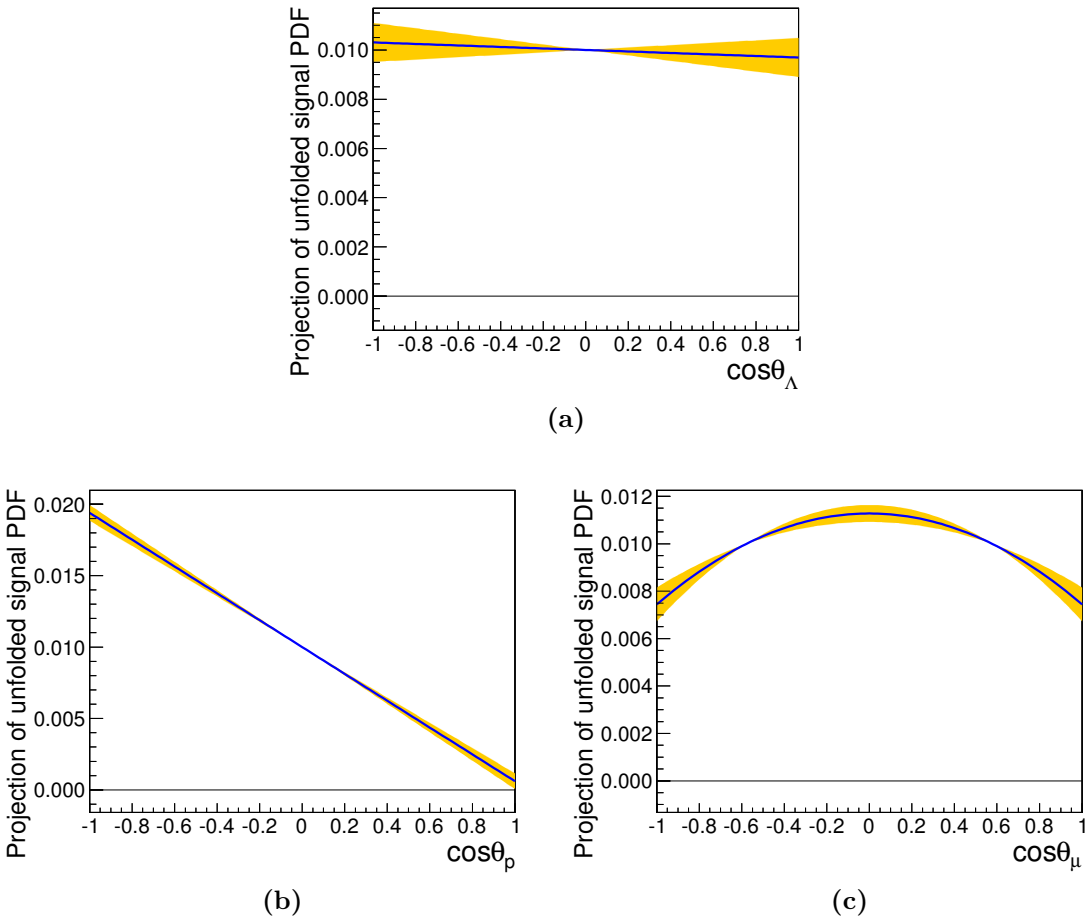

Figure 5.13: Simulation of the signal angular distributions, corrected for efficiency and detector effects, with the physics parameters obtained by the fit to data. The color band represents one statistical standard deviation as obtained by the fit. Projections in (a) $\cos\theta_\Lambda$, (b) $\cos\theta_p$, (c) $\cos\theta_\mu$.

5.10 Systematic uncertainties

Various sources of systematic uncertainties which affect the measurement of the physics parameters $\alpha = (P^+, P^-, \alpha_1, \alpha_2, \gamma_0)$ are considered. A list of the contributions follows.

- **Signal mass model**
  The systematic uncertainty introduced by the model describing the Λ_b ($\overline{\Lambda}_b$) candidates mass distribution is estimated by considering an alternative model. A sum of three Gaussian functions is used instead of the nominal model with two Gaussians. The deviation from the nominal result for each fitted parameter in the full likelihood fit to the data is considered as the associated systematic effect.

- **Background mass model**
  The background in the ($J/\psi\,\Lambda$) invariant mass distribution is alternatively described by a second order polynomial instead of the nominal linear function. The difference from the nominal result for each fitted parameter in the full likelihood fit is accounted as a systematic uncertainty.

- **Uncertainty on the asymmetry parameter α_Λ**
  The asymmetry parameter α_Λ is varied within its measurement uncertainties [16]. The largest deviation from the nominal results of the full fit to data is taken as a systematic uncertainty.

- **Angular efficiency shapes**
  To account for systematic uncertainties introduced by the modeling of the angular efficiency shapes, the order of the Chebyshev polynomials used for their parametrization is varied with one degree. The largest deviation from the nominal results of the full fit to data is considered as the associated systematic uncertainty.

- **Signal to background ratio**
  In order to estimate the influence of the background fraction, the number of signal and background events is varied within one statistical standard deviation. The largest difference from the nominal results of the full fit to data is taken as a systematic uncertainty.

- **Angular shapes of the background**
  The uncertainty introduced by the parametrization of the background angular distributions is estimated by using the histograms of the background distributions, instead of parametrized curves. The associated systematic error for each parameter is the deviation from the nominal results.

- **Calibration of the simulated signal samples**
  Uncertainties due to the calibration of the simulated signal samples are evaluated by obtaining the angular efficiency shapes before and after re-weighting the simulated events. The samples are re-weighted to match the total and the transverse momentum distribution of Λ_b and $\overline{\Lambda}_b$ in data. The largest deviation from the nominal full fit result is accounted as a systematic uncertainty.

- **Intrinsic bias of the fit**
  1,000 pseudo-experiments are performed with the full PDF which is used to fit the data (see Section 5.7.2). The pull distributions of the fitted parameters serve to estimate the intrinsic biases of the fit. For each parameter, the pull mean value multiplied by the nominal error of the fit is accounted as a systematic effect. Additional uncertainty is added, based on the pull standard deviation, to correct for underestimated statistical errors of the fit.

- **Angular resolution**
  Systematic uncertainties due to finite measurement resolution of the angular observables $\Theta = (\cos\theta_\Lambda, \cos\theta_p, \cos\theta_\mu)$ are estimated by performing pseudo-experiments in which the samples are generated with smeared angles. The magnitude of the introduced smearing is twice as large as the resolution observed from full detector simulation. 1,000 samples, each containing 100,000 Λ_b and 100,000 $\overline{\Lambda}_b$ events, are fitted with the signal PDF which does not take into account the angular resolution. The resulting pull distributions for the five fit parameters serve to estimate the associated systematic uncertainty.

- **Azimuthal angles φ_p and φ_μ**
  Systematic uncertainties due to the exclusion of the azimuthal angles from the likelihood function can be introduced by a possibly non-uniform efficiency in φ_p and φ_μ. The effect is investigated with simulated signal events. The full likelihood fit is performed to a number of sub-samples limited in certain ranges of φ_p and φ_μ. The largest deviation from the result obtained from the full sample (covering the full range of the azimuthal angles) is taken as a systematic uncertainty.

The contributions from the different uncertainty sources are summarized in Table 5.9. They are assumed to be independent and the total systematic uncertainty is calculated as the square root of the quadratic sum of all uncertainties.

The bias of the fit and the effect from non-uniform efficiency for the angles φ_p and φ_μ have dominating contributions to the systematic uncertainties on the polarizations of Λ_b and $\overline{\Lambda}_b$. Significant contributions to the $\overline{\Lambda}_b$ polarization uncertainty have also the model describing the background mass distribution and the signal

to background ratio. The uncertainty on the decay asymmetry parameter α_1 is dominated by the bias of the fit and the signal to background ratio.

A summary of the fit results from the data and their statistical and systematic uncertainties is given in Table 5.10.

Uncertainty source	P^+	P^-	α_1	α_2	γ_0
Signal mass model	0.002	0.000	0.000	0.002	0.002
Background mass model	0.005	0.018	0.025	0.009	0.015
S/B ratio	0.006	0.033	0.109	0.025	0.039
Background angular model	0.007	0.001	0.037	0.030	0.068
Simulation calibration	0.001	0.009	0.058	0.049	0.123
Angular efficiency shapes	0.001	0.002	0.013	0.004	0.020
α_Λ uncertainty	0.004	0.021	0.018	0.027	0.017
Angular resolution	0.003	0.002	0.007	0.002	0.008
Fit bias	0.019	0.013	0.101	0.012	0.003
Azimuthal angles	0.023	0.024	0.042	0.053	0.052
Total	**0.03**	**0.05**	**0.17**	**0.09**	**0.16**

Table 5.9: Summary of systematic uncertainties. The contributions are assumed to be independent and the total systematic uncertainty is therefore calculated as the square root of the quadratic sum of all uncertainties.

Parameter	Result	Stat. error	Syst. error
P^+	0.03	0.09	0.03
P^-	0.02	0.08	0.05
α_1	0.47	0.24	0.17
α_2	-1.31	0.07	0.09
γ_0	-0.51	0.14	0.16

Table 5.10: Summary table for the fit results from data and their statistical and systematic uncertainties.

By definition, the range of values for the five parameters in the analysis is $[-1, 1]$. The result for the parameter α_2, namely $\alpha_2 < -1$, is therefore unphysical. To investigate the effect of this, the fit to data is redone with the parameter α_2 fixed to the lowest physical value, $\alpha_2 = -1$. This shows no influence on the polarization, resulting in $P^+ = 0.02 \pm 0.07\,(\text{stat.})$ and $P^- = 0.03 \pm 0.05\,(\text{stat.})$, and a small effect on the parameter γ_0, resulting in $\gamma_0 = -0.41 \pm 0.15\,(\text{stat.})$. However, the effect on the parameter α_1 is substantial, although still within the statistical uncertainties, leading to $\alpha_1 = 0.81 \pm 0.25\,(\text{stat.})$. This indicates a strong correlation between the parameters α_1 and α_2.

5.11 Conclusion and discussion

The decay $\Lambda_b \to J/\psi(\mu^+\mu^-)\Lambda(p\pi^-)$ is used to perform a measurement of the polarization of the Λ_b baryon. The analysis uses pp collision data at a center-of-mass energy of 7 TeV that were collected by the CMS experiment in 2011. The data sample corresponds to an integrated luminosity of 5.1 fb^{-1}.

The analysis exploits the angular correlations between the daughter particles in the decay. The set of physics parameters, such as the polarizations of Λ_b and $\overline{\Lambda}_b$ baryons and the parity violation asymmetry parameter for the decay, are extracted by a specially developed and validated multi-dimensional likelihood fit. Distortions of the angular distributions due to efficiency effects from detector acceptance and event selection are studied with simulated signal samples, put through an identical reconstruction and selection procedure as data. Properties of the background are determined from events populating the sidebands of the Λ_b mass peak in data. The angular efficiency and background are separately determined for Λ_b and $\overline{\Lambda}_b$ and the fit is performed simultaneously to the relevant angular and mass distributions of the Λ_b and $\overline{\Lambda}_b$ candidates. Various tests are carried out to probe the fit's ability to extract the physics parameters of interest, especially with low-statistics samples corresponding to the available data. Studies of the fit performance are done with pseudo-experiments (toy Monte Carlo), simulations, and a mixture of full detector simulation and data events.

The number of reconstructed and selected Λ_b ($\overline{\Lambda}_b$) candidates in data is 911 ± 38 (845 ± 37) with a signal to background ratio of 3.2 (3.7) and a mean mass of 5619.8 $\pm$ 0.4 MeV/c^2. Based on this sample, a production polarization of

$$P^+ = 0.03 \pm 0.09\ (\text{stat.}) \pm 0.03\ (\text{syst.}) \quad \text{for } \Lambda_b$$

and

$$P^- = 0.02 \pm 0.08\ (\text{stat.}) \pm 0.05\ (\text{syst.}) \quad \text{for } \overline{\Lambda}_b$$

is measured. The parity violation asymmetry parameter characterizing the decay $\Lambda_b \to J/\psi\,\Lambda$ is measured to be 0.47 ± 0.24 (stat.) $\pm\, 0.17$ (syst.).

It has to be noted that at the time when these results were obtained, there was no previous polarization measurement of Λ_b baryons produced at hadron colliders. The results can now be compared with a recently published measurement by the LHCb Collaboration [99]. Based on ∼7200 $\Lambda_b \to J/\psi(\mu^+\mu^-)\Lambda(p\pi^-)$ decays, LHCb measures a Λ_b polarization of 0.06 ± 0.07 (stat.) ± 0.02 (syst.) and a decay asymmetry parameter[1] of -0.05 ± 0.17 (stat.) ± 0.07 (syst.). Note that in the work of the LHCb Collaboration, the polarizations of Λ_b and $\overline{\Lambda}_b$ baryons are assumed to be equal. The Λ_b ($\overline{\Lambda}_b$) baryon polarizations measured by the CMS and LHCb experiments are fully consistent. The results for the decay asymmetry parameter agree within the measurement uncertainties, which are very large.

The presented in this work result for the Λ_b polarization is consistent with predictions from perturbative QCD calculations for a polarization of ∼10% [26]. The result for the decay asymmetry parameter indicates a different from zero asymmetry and it is compatible, within the large measurement uncertainties, with predictions in the range 0.14 to 0.21 reported in Ref. [38, 37]. The result, however, disagrees at the level of 6 standard deviations with a prediction from HQET for an asymmetry parameter of -0.777 reported in Ref. [36][2].

The presented analysis can significantly benefit from larger data samples. The carried out tests show that the performance of the utilized likelihood fit deteriorates when applied to small statistical samples (comparable to the used data sample), and this is a dominating source of systematic uncertainty. More data will allow to improve the measurement of the decay asymmetry parameter, resolving the correlation problems with this parameter in the fit. It will also allow to probe a possible difference between the polarizations of Λ_b and $\overline{\Lambda}_b$. More data will as well facilitate the measurement of the helicity amplitudes of the decay, which requires the employment of additional free parameters and angular observables in the fit. Larger signal samples will also allow to measure the polarization in different kinematic regions in order to investigate for dependences on the kinematics, since such dependences have been observed for the Λ hyperon polarization.

In 2012, the impressive performance of LHC and the CMS detector provided 22 fb^{-1} of pp collision data at a center-of-mass energy of 8 TeV. These data will undoubtedly refine the measurement of the Λ_b polarization and the decay asymmetry parameter at the CMS experiment.

[1] The convention used for the definition of the asymmetry parameter in the work of the LHCb Collaboration requires a sign flip in order to match the definition of the parameter used in this thesis.

[2] The convention used for the definition of the asymmetry parameter in the quoted references requires a sign flip in order to match the definition of the parameter used in this thesis.

Appendix A

Comparison of data and simulation

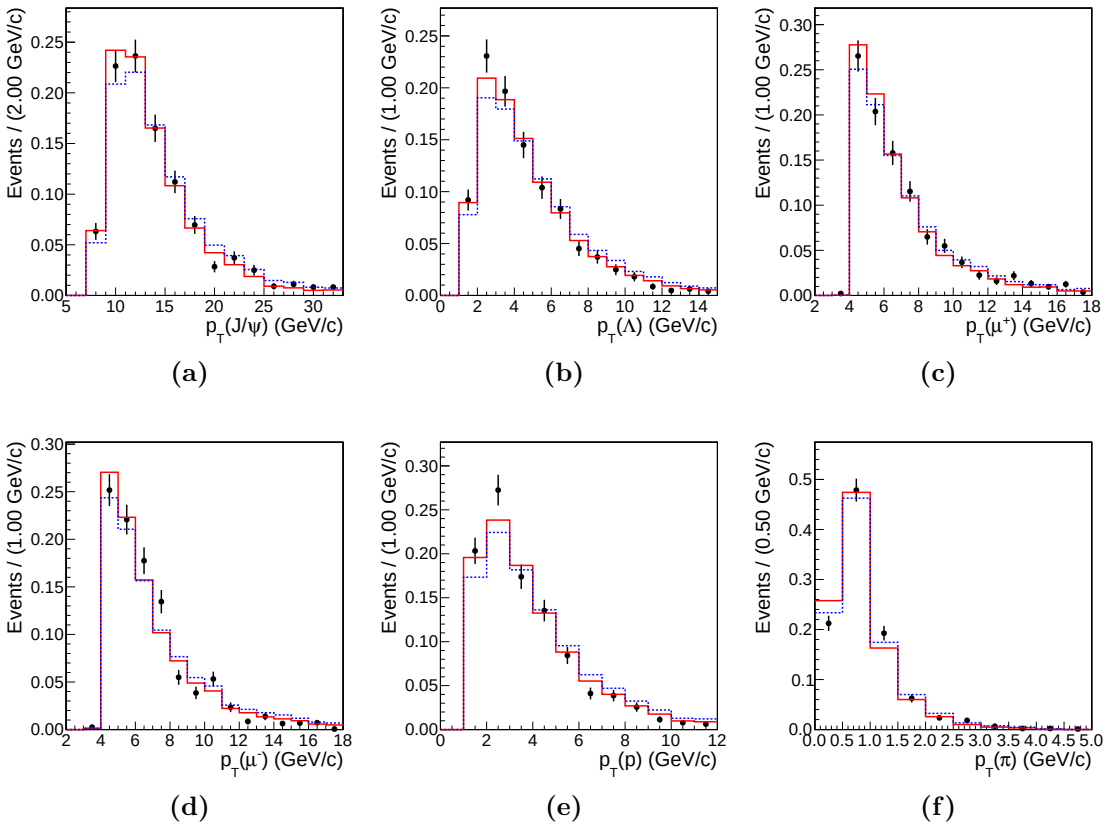

Figure A.1: Λ_b candidates: Comparison of sideband-subtracted data (black) and simulated signal. Dashed blue (Solid red) lines represent distributions in simulated samples before (after) the simulated events are re-weighted to match the $p_T(\Lambda_b)$ distribution in data. All histograms are normalized to a unit area. Transverse momentum distributions for (a) J/ψ, (b) Λ, (c) μ^+, (d) μ^-, (e) p, (f) π^-.

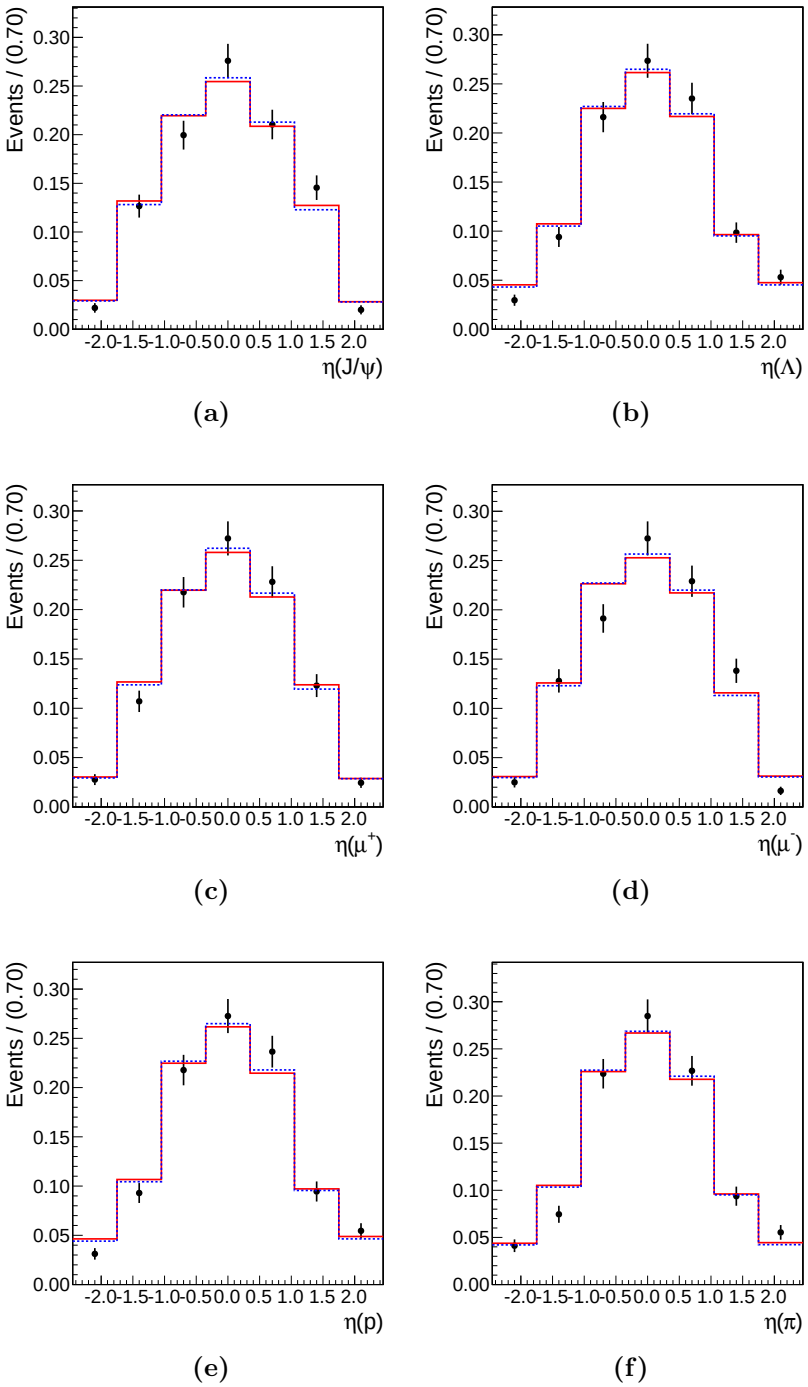

Figure A.2: Λ_b candidates: Comparison of sideband-subtracted data (black) and simulated signal. Dashed blue (Solid red) lines represent distributions in simulated samples before (after) the simulated events are re-weighted to match the $p_T(\Lambda_b)$ distribution in data. All histograms are normalized to a unit area. Pseudorapidity distributions for (a) J/ψ, (b) Λ, (c) μ^+, (d) μ^-, (e) p, (f) π^-.

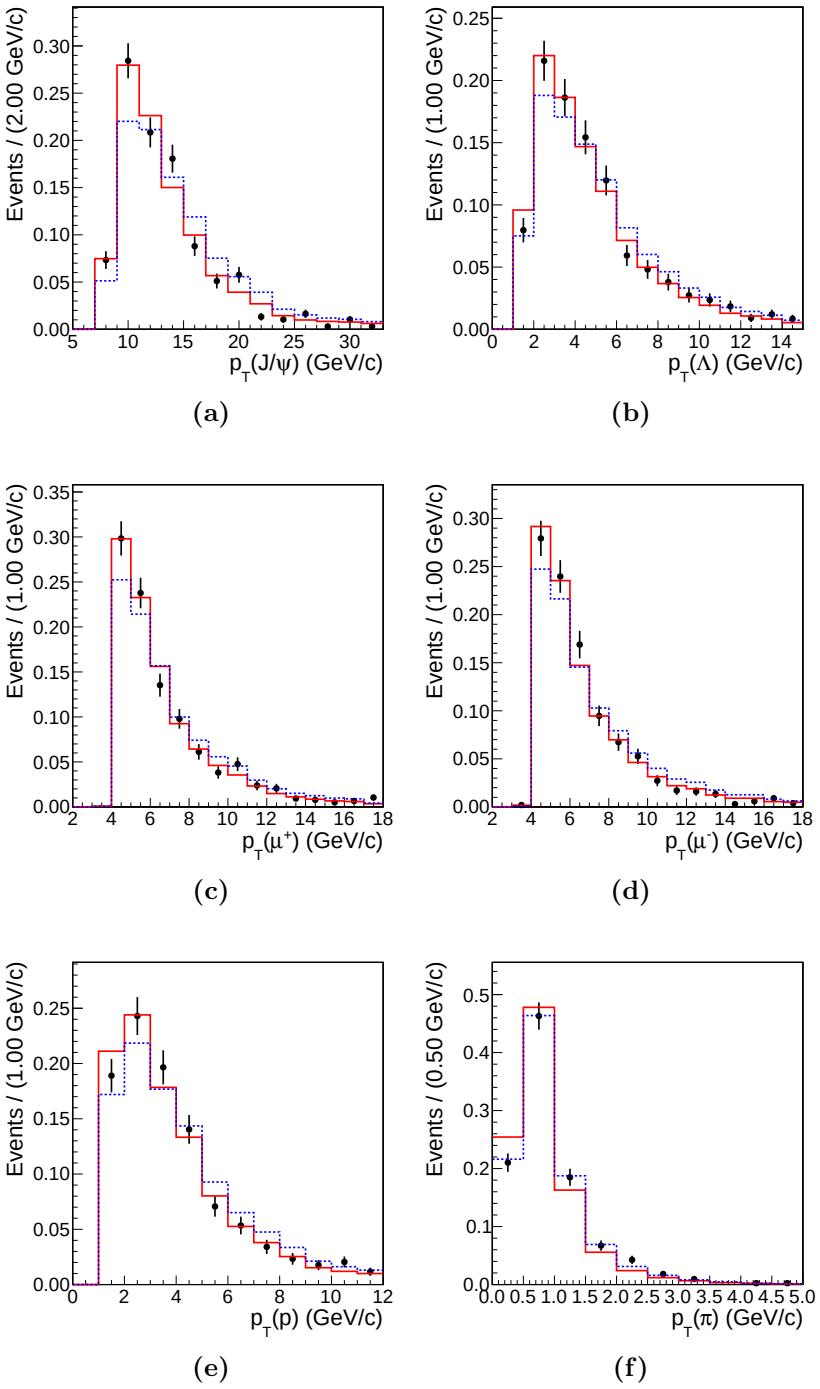

Figure A.3: $\overline{\Lambda}_b$ candidates: Comparison of sideband-subtracted data (black) and simulated signal. Dashed blue (Solid red) lines represent distributions in simulated samples before (after) the simulated events are re-weighted to match the $p_T(\Lambda_b)$ distribution in data. All histograms are normalized to a unit area. Transverse momentum distributions for (a) J/ψ, (b) $\overline{\Lambda}$, (c) μ^+, (d) μ^-, (e) $\overline{p}$, (f) π^+.

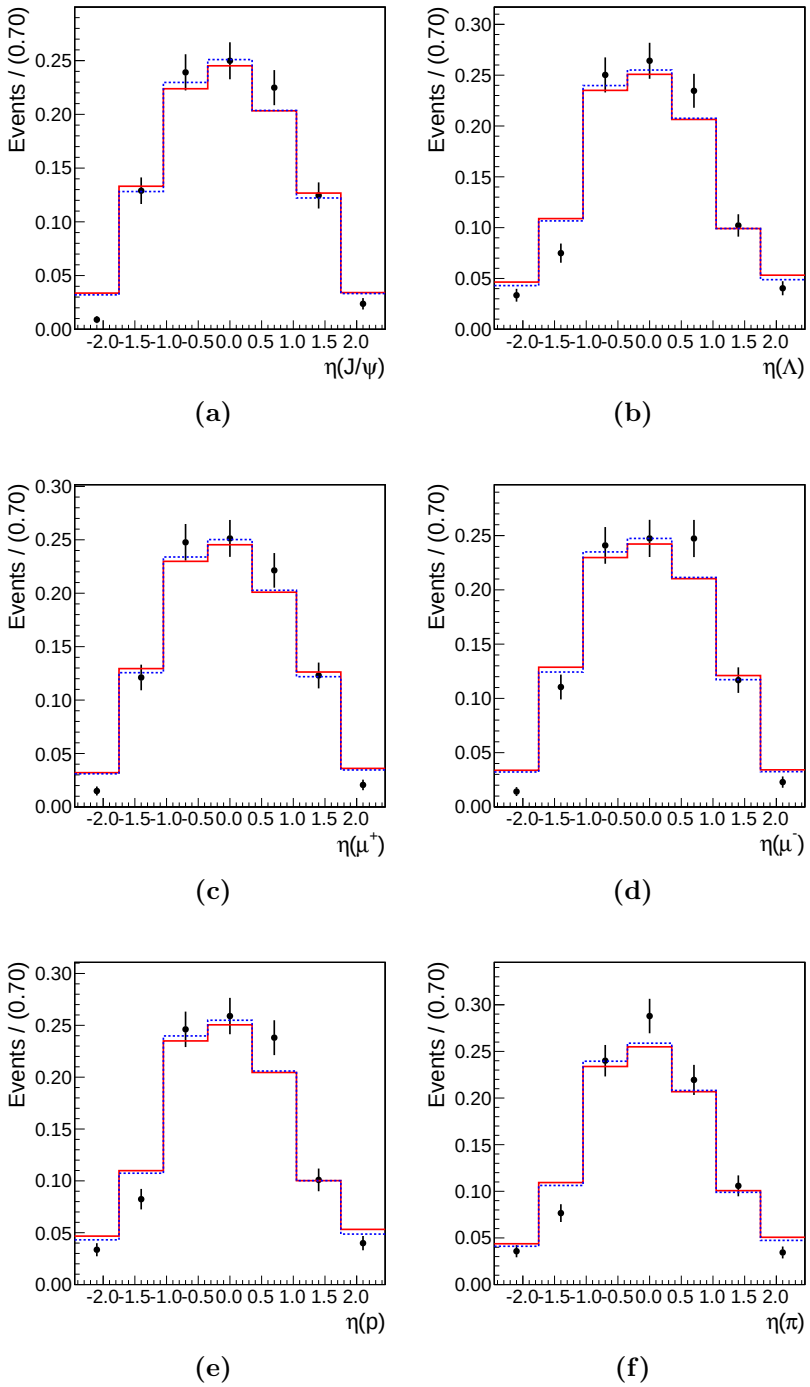

Figure A.4: $\overline{\Lambda}_b$ candidates: Comparison of sideband-subtracted data (black) and simulated signal. Dashed blue (Solid red) lines represent distributions in simulated samples before (after) the simulated events are re-weighted to match the $p_T(\Lambda_b)$ distribution in data. All histograms are normalized to a unit area. Pseudorapidity distributions for (a) J/ψ, (b) $\overline{\Lambda}$, (c) μ^+, (d) μ^-, (e) $\overline{p}$, (f) π^+.

Appendix B

Comparison of data with low and high number of pile-up events

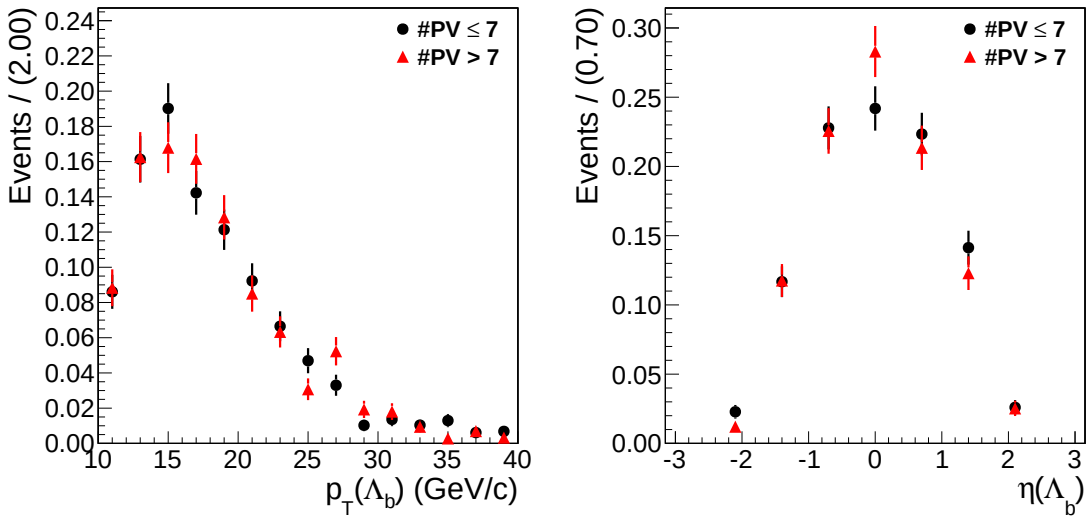

(a) **(b)**

Figure B.1: Distributions for Λ_b (+ c.c.) candidates reconstructed in events with up to 7 (black circles) and more than 7 (red triangles) primary vertices. The events are contained in the mass peak of Λ_b and the background is subtracted. (a) Transverse momentum. (b) Pseudorapidity. The histograms are normalized to a unit area.

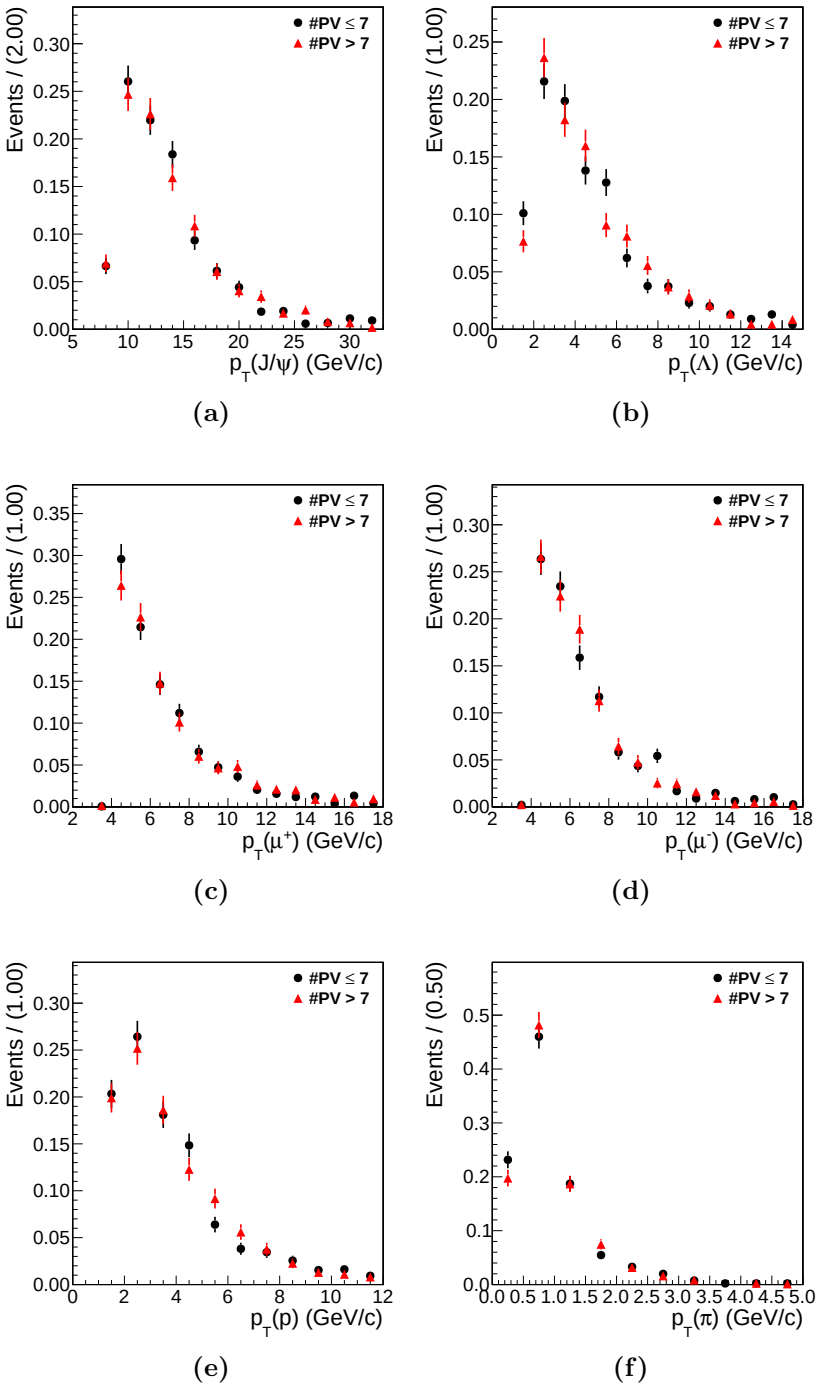

Figure B.2: Transverse momentum distributions of the daughter particles in the Λ_b (+ c.c.) decays, reconstructed in events with up to 7 (black circles) and more than 7 (red triangles) primary vertices. The events are contained in the mass peak of Λ_b and the background is subtracted. Distributions for (a) J/ψ, (b) Λ, (c) μ^+, (d) μ^-, (e) p, (f) π. The histograms are normalized to a unit area.

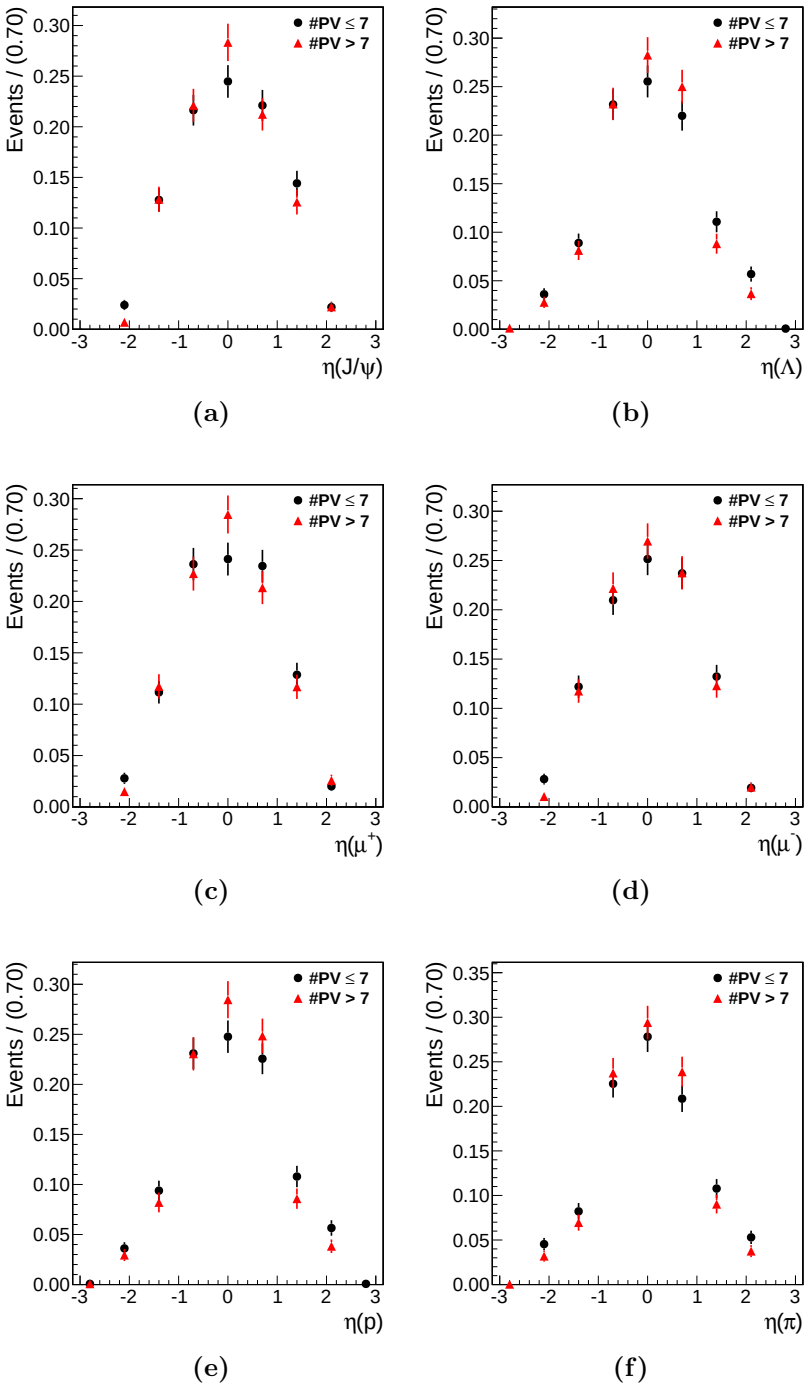

Figure B.3: Pseudorapidity distributions of the daughter particles in the Λ_b (+ c.c.) decays, reconstructed in events with up to 7 (black circles) and more than 7 (red triangles) primary vertices. The events are contained in the mass peak of Λ_b and the background is subtracted. Distributions for (a) J/ψ, (b) Λ, (c) μ^+, (d) μ^-, (e) p, (f) π. The histograms are normalized to a unit area.

List of Figures

List of Tables

Bibliography

[1] M. Kobayashi and T. Maskawa, "CP Violation in the Renormalizable Theory of Weak Interaction", *Prog. Theor. Phys.* **49** (1973) 652–657. doi:10.1143/PTP.49.652. 1, 5

[2] J. J. Aubert et al., "Experimental Observation of a Heavy Particle J", *Phys. Rev. Lett.* **33** (1974) 1404–1406. doi:10.1103/PhysRevLett.33.1404. 1

[3] J. E. Augustin et al., "Discovery of a Narrow Resonance in e^+e^- Annihilation", *Phys. Rev. Lett.* **33** (1974) 1406–1408. doi:10.1103/PhysRevLett.33.1406. 1

[4] S. W. Herb et al., "Observation of a Dimuon Resonance at 9.5 GeV in 400-GeV Proton-Nucleus Collisions", *Phys. Rev. Lett.* **39** (1977) 252–255. doi:10.1103/PhysRevLett.39.252. 1, 2

[5] D0 Collaboration, "Search for High Mass Top Quark Production in $p\overline{p}$ Collisions at $\sqrt{s} =$ 1.8 TeV", *Phys. Rev. Lett.* **74** (1995) 2422–2426. doi:10.1103/PhysRevLett.74.2422. 1

[6] CDF Collaboration, "Observation of Top Quark Production in $\overline{p}p$ Collisions with the Collider Detector at Fermilab", *Phys. Rev. Lett.* **74** (1995) 2626–2631. doi:10.1103/PhysRevLett.74.2626. 1

[7] C. Albajar et al., "First observation of the beauty baryon Λ_b in the decay channel $\Lambda_b \to J/\psi\Lambda$ at the CERN proton-antiproton collider", *Phys. Lett.* **B273** (1991) 540–548. doi:10.1016/0370-2693(91)90311-D. 2, 3

[8] K. Chadwick et al., "Decay of b-Flavored Hadrons to Single-Muon and Dimuon Final States", *Phys. Rev. Lett.* **46** (1981) 88–91. doi:10.1103/PhysRevLett.46.88. 2

[9] L. J. Spencer et al., "Measurement of B-Meson Semileptonic Decay", *Phys. Rev. Lett.* **47** (1981) 771–774. doi:10.1103/PhysRevLett.47.771. 2

[10] A. Brody et al., "Decay of B Mesons into Charged and Neutral Kaons", *Phys. Rev. Lett.* **48** (1982) 1070–1074. doi:10.1103/PhysRevLett.48.1070. 2

[11] M. S. Alam et al., "Charged-Particle Multiplicities in B-Meson Decay", *Phys. Rev. Lett.* **49** (1982) 357–360. doi:10.1103/PhysRevLett.49.357. 2

[12] K. Chadwick et al., "Semileptonic decays of B mesons", *Phys. Rev.* **D27** (1983) 475–485. doi:10.1103/PhysRevD.27.475. 2

[13] S. Behrends et al., "Observation of Exclusive Decay Modes of b-Flavored Mesons", *Phys. Rev. Lett.* **50** (1983) 881–884. doi:10.1103/PhysRevLett.50.881. 2

[14] M. Basile et al., "Evidence for a new particle with naked ≪beauty≫ and for its associated production in high-energy (pp) interactions", *Lettere al Nuovo Cimento* **31** (1981) 97–111. doi:10.1007/BF02822406. 2

[15] D. Drijard et al., "Further investigation of beauty baryon production at the ISR", *Phys. Lett.* **B108** (1982) 361–366. doi:10.1016/0370-2693(82)91213-8. 2

[16] Particle Data Group, "Review of Particle Physics (RPP)", *Phys. Rev.* **D86** (2012). doi:10.1103/PhysRevD.86.010001. 3, 5, 6, 17, 59, 60, 61, 96

[17] CDF Collaboration, "Measurement of the Λ_b^0 Lifetime in $\Lambda_b^0 \to J/\psi\Lambda^0$ in $p\bar{p}$ Collisions at $\sqrt{s} = 1.96$ TeV", *Phys. Rev. Lett.* **98** (2007) 122001, arXiv:hep-ex/0609021. doi:10.1103/PhysRevLett.98.122001. 3

[18] Heavy Flavor Averaging Group, "Averages of B-Hadron, C-Hadron, and tau-lepton properties as of early 2012", arXiv:1207.1158. 3

[19] E. Norrbin and T. Sjöstrand, "Production and hadronization of heavy quarks", *Eur. Phys. J.* **C17** (2000) 137–161, arXiv:hep-ph/0005110. doi:10.1007/s100520000460. 3, 5

[20] B. Webber, "Hadronization", *Lectures at Summer School on Hadronic Aspects of Collider Physics* (1994) arXiv:hep-ph/9411384. 5

[21] M. Neubert, "Heavy quark effective theory", arXiv:hep-ph/9610266. 5

[22] J. Körner, M. Krämer, and D. Pirjol, "Heavy baryons", *Prog. Part. Nucl. Phys.* **33** (1994) 787–868, arXiv:hep-ph/9406359. doi:10.1016/0146-6410(94)90053-1. 5

[23] CMS Collaboration, "Measurement of the Λ_b cross section and the $\bar{\Lambda}_b$ to Λ_b ratio with $J/\Psi\Lambda$ decays in pp collisions at $\sqrt{s} = 7$ TeV", *Phys. Lett.* **B714** (2012) 136–157, arXiv:1205.0594. doi:10.1016/j.physletb.2012.05.063. 6

[24] E. Noether, "Invariante Variationsprobleme", *Nachr. D. König. Gesellsch. D. Wiss. Zu Göttingen* (1918) 235–257. 7

[25] E. Leader, "Spin in Particle Physics". Cambridge University Press, 2005. 8

[26] W. G. Dharmaratna and G. R. Goldstein, "Single quark polarization in quantum chromodynamics subprocesses", *Phys. Rev.* **D53** (1996) 1073–1086. doi:10.1103/PhysRevD.53.1073. 8, 100

[27] W. G. D. Dharmaratna and G. R. Goldstein, "Gluon fusion as a source for massive-quark polarization", *Phys. Rev.* **D41** (1990) 1731–1735. doi:10.1103/PhysRevD.41.1731. 9

[28] E. Ramberg et al., "Polarization of Λ and $\overline{\Lambda}$ produced by 800-GeV protons", *Phys. Lett.* **B338** (1994) 403–408. doi:10.1016/0370-2693(94)91397-8. 9

[29] V. Fanti et al., "A measurement of the transverse polarization of Λ-hyperons produced in inelastic pN-reactions at 450 GeV proton energy", *Eur. Phys. J.* **C6** (1999) 265–269. doi:10.1007/s100529801045. 9

[30] HERA-B Collaboration, "Polarization of Lambda and anti-Lambda in 920-GeV fixed-target proton-nucleus collisions", *Phys. Lett.* **B638** (2006) 415–421, arXiv:hep-ex/0603047. doi:10.1016/j.physletb.2006.05.040. 9

[31] ALEPH Collaboration, "Measurement of Λ_b polarization in Z decays", *Phys. Lett.* **B365** (1996) 437–447. doi:10.1016/0370-2693(95)01433-0. 9

[32] DELPHI Collaboration, "Λ_b polarization in Z^0 decays at LEP", *Phys. Lett.* **B474** (2000) 205–222. doi:10.1016/S0370-2693(99)01431-8. 9

[33] OPAL Collaboration, "Measurement of the average polarization of b baryons in hadronic Z^0 decays", *Phys. Lett.* **B444** (1998) 539–554, arXiv:hep-ex/9808006. doi:10.1016/S0370-2693(98)01387-2. 9

[34] B. Mele and G. Altarelli, "Lepton spectra as a measure of b quark polarization at LEP", *Phys. Lett.* **B299** (1993) 345–350. doi:10.1016/0370-2693(93)90272-J. 9

[35] T. Mannel and G. A. Schuler, "Semileptonic decays of bottom baryons at LEP", *Phys. Lett.* **B279** (1992) 194–200. doi:10.1016/0370-2693(92)91864-6. 9

[36] Z. Ajaltouni, E. Conte, and O. Leitner, "Λ_b decays into Λ-vector", *Phys. Lett.* **B614** (2005) 165–173, arXiv:hep-ph/0412116. doi:10.1016/j.physletb.2005.04.014. 10, 100

[37] R. Mohanta et al., "Hadronic weak decays of Λ_b baryon in the covariant oscillator quark model", *Prog. Theor. Phys.* **101** (1999) 959–969, arXiv:hep-ph/9904324. doi:10.1143/PTP.101.959. 10, 100

[38] C.-H. Chou et al., "$\Lambda_b \to \Lambda J/\psi$ decay in perturbative QCD", *Phys. Rev.* **D65** (2002) 074030, arXiv:hep-ph/0112145. doi:10.1103/PhysRevD.65.074030. 10, 100

[39] A. F. Falk and M. E. Peskin, "Production, decay, and polarization of excited heavy hadrons", *Phys. Rev.* **D49** (1994) 3320–3332, arXiv:hep-ph/9308241. doi:10.1103/PhysRevD.49.3320. 10

[40] CDF Collaboration, "First observation of heavy baryons Σ_b and Σ_b^*", *Phys. Rev. Lett.* **99** (2007) 202001, arXiv:0706.3868. doi:10.1103/PhysRevLett.99.202001. 10

[41] G. Hiller et al., "Photon polarization from helicity suppression in radiative decays of polarized Λ_b to spin-3/2 baryons", *Phys. Lett.* **B649** (2007) 152–158, arXiv:hep-ph/0702191. doi:10.1016/j.physletb.2007.03.056. 10

[42] J. D. Richman, "An experimenter's guide to the helicity formalism", Technical Report CALT-68-1148, Calif. Inst. Technol., (1984). 10

[43] C. Amsler and J. Bizot, "Simulation of angular distributions and correlations in the decay of particles with spin", *Comput. Phys. Commun.* **30** (1983) 21–30. doi:10.1016/0010-4655(83)90118-2. 10

[44] C. Amsler, "Decay angular distributions", *Seminar in Leukerbad, Switzerland* (June, 2011). 10

[45] M. Krämer and H. Simma, "Angular correlations in $\Lambda_b \to \Lambda + V$: Polarization measurements, HQET and CP violation", *Nucl. Phys. B – Proc. Suppl.* **50** (1996) 125–129. doi:10.1016/0920-5632(96)00378-7. 14, 15, 16

[46] R. Lednicky, "About the determination of Λ_c^+ polarization", Technical Report JINR-E2-85-257, Joint Inst. Nucl. Res., Dubna, (1985). 14

[47] I. Dunietz, "CP violation with beautiful baryons", *Zeitschrift für Physik C Particles and Fields* **56** (1992) 129–143. doi:10.1007/BF01589716. 16

[48] J. F. Donoghue, X.-G. He, and S. Pakvasa, "Hyperon decays and *CP* nonconservation", *Phys. Rev.* **D34** (1986) 833–842. doi:10.1103/PhysRevD.34.833. 17

[49] "LEP design report". CERN, Geneva, 1984. 19

[50] L. Evans and P. Bryant, "LHC Machine", *J. Instrum.* **3** (2008) S08001. doi:10.1088/1748-0221/3/08/S08001. 19

[51] The CMS Collaboration, "The CMS experiment at the CERN LHC", *J. Instrum.* **3** (2008) S08004. doi:10.1088/1748-0221/3/08/S08004. 19, 23, 26, 27

[52] The ATLAS Collaboration, "The ATLAS Experiment at the CERN Large Hadron Collider", *J. Instrum.* **3** (2008) S08003. doi:10.1088/1748-0221/3/08/S08003. 19

[53] The LHCb Collaboration, "The LHCb Detector at the LHC", *J. Instrum.* **3** (2008) S08005. doi:10.1088/1748-0221/3/08/S08005. 19

[54] The ALICE Collaboration, "The ALICE experiment at the CERN LHC", *J. Instrum.* **3** (2008) S08002. doi:10.1088/1748-0221/3/08/S08002. 20

[55] The LHC website. http://lhc.web.cern.ch/lhc. 20

[56] The CMS website. http://cms.web.cern.ch. 21

[57] O. S. Brüning et al., "LHC Design Report". CERN, 2004. 22

[58] The CMS Collaboration, "CMS Physics Technical Design Report, Volume II: Physics Performance", *J. Phys.* **G34** (2007) 995. doi:10.1088/0954-3899/34/6/S01. 21

[59] "The CMS magnet project: Technical Design Report". Technical Design Report CMS. CERN, 1997. 23

[60] C. Amsler et al., "Mechanical design and material budget of the CMS barrel pixel detector", *J. Instrum.* **4** (2009). doi:10.1088/1748-0221/4/05/P05003. 24

[61] The CMS Collaboration, "CMS Physics: Technical Design Report Volume 1: Detector Performance and Software". Technical Design Report CMS. CERN, 2006. 26, 29

[62] CMS Collaboration, "CMS ECAL Technical Design Report", (1997). CERN-LHCC 97-033. 27

[63] CMS Collaboration, "CMS HCAL Technical Design Report", (1997). CERN-LHCC 97-031. 28

[64] CMS Collaboration, "The Level-1 Trigger Technical Design Report", (2000). CERN-LHCC-2000-38. 30

[65] CMS Collaboration, "Data Aqcuisition and High-Level Trigger Technical Design Report", (2002). CERN-LHCC-2002-26. 30

[66] I. Antcheva et al., "ROOT – A C++ framework for petabyte data storage, statistical analysis and visualization", *Comput. Phys. Commun.* **180** (2009) 2499–2512. doi:10.1016/j.cpc.2009.08.005. 31

[67] W. Adam et al., "Description and performance of the CMS track and primary vertex reconstruction", *CMS Note* (2011). CMS AN-11-172. 31

[68] R. Frühwirth, "Application of Kalman filtering to track and vertex fitting", *Nucl. Instrum. Meth.* **A262** (1987) 444–450. doi:10.1016/0168-9002(87)90887-4. 31, 36

[69] M. Pioppi, "Iterative tracking", *CMS Note* (2007). CMS IN 2007/065. 32

[70] CMS Collaboration, "Performance of CMS muon reconstruction in pp collision events at $\sqrt{s} = 7$ TeV", (2012). CERN-PH-EP-2012-173. doi:10.1088/1748-0221/7/10/P10002. 33, 34

[71] K. Rose, "Deterministic Annealing, Clustering and Optimization", *PhD thesis, California Institute of Technology* (1991). 34

[72] W. Erdmann, "Offline Primary Vertex Reconstruction with Deterministic Annealing Clustering", *CMS Internal Note* (2011). CMS-IN-2011/014. 34

[73] W. Waltenberger, "Development of Vertex Finding and Vertex Fitting Algorithms for CMS", *PhD thesis, Technical University of Vienna* (2004). 35

[74] R. Frühwirth et al., "New developments in vertex reconstruction for CMS", *Nucl. Instrum. Meth.* **A502** (2003) 699–701. doi:10.1016/S0168-9002(03)00548-5. 35

[75] R. Frühwirth, W. Waltenberger, and P. Vanlaer, "Adaptive Vertex Fitting", *CMS Note* (2007). CMS-NOTE-2007/008. 35

[76] R. Frühwirth et al., "Vertex reconstruction and track building at the LEP collider using robust algorithms", *Comput. Phys. Commun.* **96** (1996) 189–208. doi:10.1016/0010-4655(96)00040-9. 36

[77] T. Speer et al., "Vertex Fitting in the CMS Tracker", *CMS Note* (2006). CMS-NOTE-2006-032. 36

[78] K. Prokofiev and T. Speer, "A Kinematic fit and a decay chain reconstruction library", *CMS Internal Note* (2004). CMS-IN-2004-020. 36

[79] G. Arfken, "Mathematical Methods for Physicists", (1985). Academic Press. 36, 75, 79

[80] L. Wilke, V. Chiochia, and T. Speer, "Lorentz angle calibration for the barrel pixel detector", *CMS Note* (2008). CMS-NOTE-2008-012. 38, 46

[81] Y. Allkofer et al., "Design and performance of the silicon sensors for the CMS barrel pixel detector", *Nucl. Instrum. Meth.* **A584** (2008) 25–41. doi:10.1016/j.nima.2007.08.151. 37, 39

[82] A. Castoldi et al., "Performance of silicon drift detectors in a magnetic field", *Nucl. Instrum. Meth.* **A399** (1997) 227–243. doi:10.1016/S0168-9002(97)00909-1. 38

[83] R. Kaufmann, "Development of Radiation Hard Pixel Sensors for the CMS Experiment", *PhD thesis, University of Zurich* (2001). 40

[84] L. Wilke, "Study of the B_s-Meson with the First LHC Data", *PhD thesis, University of Zurich* (2009). 40, 41, 43, 44, 45, 50

[85] CMS Collaboration, "Commissioning and performance of the CMS silicon strip tracker with cosmic ray muons", *J. Instrum.* **5** (2010). doi:10.1088/1748-0221/5/03/T03008. 40

[86] The CMS Collaboration, "Commissioning and performance of the CMS pixel tracker with cosmic ray muons", *J. Instrum.* **5** (2010). doi:10.1088/1748-0221/5/03/T03007. 41, 44, 45

[87] M. Swartz, "CMS pixel simulations", *Nucl. Instrum. Meth.* **A511** (2003) 88–91. doi:10.1016/S0168-9002(03)01757-1. 43

[88] M. Swartz, "A Detailed Simulation of the CMS Pixel Sensor", *CMS Note* (2002). CMS-NOTE-2002-027. 43

[89] B. Henrich and R. Kaufmann, "Lorentz-angle in irradiated silicon", *Nucl. Instrum. Meth.* **A477** (2002) 304–307. doi:10.1016/S0168-9002(01)01865-4. 46

[90] T. Sjöstrand, S. Mrenna, and P. Skands, "PYTHIA 6.4 physics and manual", *J. High Energy Phys.* **026** (2006). doi:10.1088/1126-6708/2006/05/026. 56

[91] D. J. Lange, "The EvtGen particle decay simulation package", *Nucl. Instrum. Meth.* **A462** (2001) 152–155. doi:10.1016/S0168-9002(01)00089-4. 56

[92] ATLAS Collaboration, "Expected Performance of the ATLAS Experiment - Detector, Trigger and Physics", CERN-OPEN-2008-020, arXiv:0901.0512. 56

[93] A. Ryd et al., "EvtGen: A Monte Carlo Generator for B-Physics", (2005) EVTGEN-V00-11-07. 56

[94] S. Agostinelli et al., "GEANT4: A Simulation toolkit", *Nucl. Instrum. Meth.* **A506** (2003) 250–303. doi:10.1016/S0168-9002(03)01368-8. 57

[95] CMS Collaboration, "Measurement of differential cross sections versus p_T and $|y|$ of K^0_s, Λ^0 and Ξ^- from 7 TeV pp collisions at CMS", *CMS Internal Note* (2010) CMS PAPER AN-10-084. 59, 60

[96] CMS Collaboration, "Tracking and Vertexing Results from First Collisions", *CMS Physics Analysis Summary* (2010) CMS PAS TRK-10-001. 59

[97] W. Verkerke and D. Kirkby, "The RooFit toolkit for data modeling", *Comput. High Energy Nucl. Phys.* (2003). arXiv:physics/0306116 [physics.data-an]. 63, 73

[98] G. Cowan, "Statistical Data Analysis", (1998). Oxford University Press. 72

[99] LHCb Collaboration, "Measurements of the $\Lambda^0_b \to J/\psi\Lambda$ decay amplitudes and the Λ^0_b polarisation in pp collisions at $\sqrt{s} = 7$ TeV", *Phys. Lett.* **B724** (2013) 27–35. doi:10.1016/j.physletb.2013.05.041. 100

Acknowledgements

In the first place, I would like to express my sincere gratitude to Prof. Dr. Claude Amsler for giving me the great opportunity to do a PhD study in his group. He gave me the freedom and independence to pursue my analysis, while offering advice, discussions, support and encouragement, which were of invaluable help to me. I certainly benefited from his extensive knowledge in physics and acute sense for detail. I am particularly grateful for the opportunity to work at CERN at the start-up of LHC and CMS – this was a priceless experience.

I would like to thank Prof. Dr. Vincenzo Chiochia for sharing his expertise on the CMS pixel detector during the commissioning of the detector with the first LHC data – this was an exciting time. I thank him as well for the various helpful discussions and suggestions on my b-physics work.

I want to thank Keith Ulmer and Hermine Wöhri from the CMS b-physics group for their useful comments and feedback which helped me to improve and scrutinize the analysis. I owe special thanks to Urs Langenegger whose constructive comments helped me to gain a better insight on the Lorentz angle measurement and the CMS pixel detector as a whole. Thanks go also to Morris Swartz for answering to all my questions concerning the Lorentz angle.

Thanks to Frank Meier for the friendly chats on chasing the Λ_b. I want to thank also Ernest Aguilo who offered help on my earlier b-physics subjects although not covered in this thesis.

I would like to thank the whole Uni-Zurich group based at CERN for the friendly attitude and nice atmosphere. Special thanks to my colleagues Barbara Millan and my four-year-long office mate Carlotta Favaro for the numerous helpful and interesting discussions on work and life.

I also wish to acknowledge my former professors and colleagues from the University of Sofia. I would like to thank Emiliya Mladenova who kindled my interest in physics many years ago.

My final words of gratitude belong to my family. I most heartily thank my parents, my grandparents and my great-grandmother for their love, support and trust in me. I address my special thanks to Bozhidar for his patience, support and encouragement. Thank you!